ISSN 0915-633X

NATIONAL INSTITUTE FOR FUSION SCIENCE

Contributions to 30th European Physical Society Conference
on Controlled Fusion and Plasma Physics
(St.Petersburg, Russia, 7-11 July 2003)
from NIFS

(Received - Aug. 11, 2003)

NIFS-780 Aug. 2003

TOKI, JAPAN

Contributions to 30th European Physical Society Conference on Controlled Fusion and Plasma Physics (St.Petersburg, Russia, 7-11 July 2003) from NIFS

Abstract

25 contributed papers to the 30th European Physical Society Conference on Controlled Fusion and Plasma Physics (St.Petersburg, Russia, 7-11 July 2003) from the activity of NIFS are collected in this report.

Keywords : 30th European Physical Society Conference on Controlled Fusion and Plasma Physics, NIFS, Large helical device, Compact helical system, contributed paper

Recent Diagnostic Developments on LHD

S. Sudo, Y. Nagayama, B. J. Peterson, K. Kawahata, T. Akiyama, N. Ashikawa, M. Emoto, M. Goto, Y. Hamada, K. Ida, T. Ido, H. Iguchi, S. Inagaki, M. Isobe, T. Kobuchi, A. Komori, Y. Liang, S. Masuzaki, T. Minami, T. Morisaki, S. Morita, O. Motojima, S. Muto, Y. Nakamura, H. Nakanishi, M. Narushima, K. Narihara, M. Nishiura, A. Nishizawa, S. Ohdachi, M. Osakabe, T. Ozaki, R. O. Pavlichenko, S. Sakakibara, K. Sato, M. Shoji, N. Tamura, K. Tanaka, K. Toi, T. Tokuzawa, K. Y. Watanabe, T. Watanabe, H. Yamada, I. Yamada, M. Yoshinuma, P. Goncharov[1], D. Kalinina[1], T. Kanaba[1], T. Sugimoto[1], A. Ejiri[2], Y. Ono[2], H. Hojo[3], K. Ishii[3], N. Iwama[4], Y. Kogi[5], A. Mase[5], M. Sakamoto[5], K. Kondo[6], H. Nagasaki[6], S. Yamamoto[6], N. Nishino[7], S. Okajima[8], T. Saida[9], M. Sasao[9], T. Takeda[10], S. Tsuji-Iio[11], D. S. Darrow[12], H. Takahashi[12], Y. Liu[13], J. F. Lyon[14], A. Yu. Kostrioukov[15], V. B. Kuteev[15], V. Sergeev[15], I. Viniar[15], A. V. Krasilnikov[16], A. Sanin[17], L. N. Vyacheslavov[17], D. Stutman[18], M. Finkenthal[18], and LHD Group

National Institute for Fusion Science,

322-6 Oroshi, Toki 509-5292, Japan

[1]Graduate University for Advanced Studies, Hayama 240-0193, Japan

[2]University of Tokyo, Tokyo 113-8654, Japan

[3]Tsukuba University, Tsukuba 305-8577, Japan

[4]Daido Institute of Technology, Nagoya 457-8530, Japan

[5]Kyushu University, Kasuga 816-8580, Japan

[6]Kyoto University, Uji 611-0011, Japan

[7]Hiroshima University, Hiroshima 739-8511, Japan

[8]Chubu University, Kasugai 487-8501, Japan

[9]Tohoku University, Sendai 980-8579, Japan

[10]University of Electro-Communicasions, Chofu 182-8585, Japan

[11]Tokyo Institute of Technology, Tokyo 152-8550, Japan

[12]Princeton Plasma Physics Laboratory,

Princeton, New Jersey 08543-0451, USA

[13]South Western Institute of Physics, Chengdu 610041, China

[14]Oak Ridge National Laboratory, Oak Ridge , Tennessee 37831-6354, USA

[15]St. Petersburg Technical University, St. Petersburg 195251, Russia
[16]Troitsk Institute for Innovating and Fusion Research, Troitsk 142092, Russia
[17]Budker Institute of Nuclear Physics, Novosibirsk 630090, Russia and
[18]Johns Hopkins University, Baltimore, Maryland, USA

(Dated: July 4, 2003)

Abstract

Standard diagnostics for fundamental plasma parameters and for plasma physics are routinely utilized for daily operation and physics study in the large helical device (LHD) with high reliability. Diagnostics for steady state plasma are intensively developed, especially for T_e, n_e (YAG laser Thomson, CO_2 laser polarimeter), data acquisition in steady state, heat resistant probes. To clarify the plasma property of the helical structure, 2-D or 3-D diagnostics are intensively developed: Tangential cameras (Fast SX TV, Photon counting CCD, H_α TV); Tomography (Tangential SX CCD, Bolometer); Imaging (Bolometer, ECE, Reflectometer). Divertor and edge physics are one of important key issues for steady state operation. Diagnostics for neutral flux (H_α array, Zeeman spectroscopy) and n_e (Fast scanning probe, Li beam probe, Pulsed radar reflectometer). In addition to these, advanced diagnostics are being intensively developed with national and international collaborations in LHD.

INTRODUCTION

Requirements to realize a fusion reactor are as follows: (a) high plasma confinement; (b) stable and steady state operation; (c) adequate material against neutron wall load, and so on. The progress in the study of plasma confinement is so remarkable that the next generation device will reach the ignition condition. Development of material replacement technology may solve the problem of wall load, as quick replacement minimizes the dead time of reactor operation. Stable and steady state operation is one of the most crucial issues in the study of fusion reactor. In tokamaks, stable and steady state operation is still difficult subjects to be solved. Tokamaks suffer the current disruption, which happens when the plasma current or the β value is high, where β is the ratio of the plasma pressure to the magnetic pressure. Plasma current, which makes tokamak configuration, is inductively introduced in case of traditional scheme, but it is very challenging to maintain plasma current in the steady state.

On the other hand, a helical system is expected to be a disruption-free steady-state reactor since no plasma current is required. Among different types of helical systems, the large helical device (LHD) [1] is the world's largest device fully equipped with superconducting magnets, modern diagnostics and high power heating systems. The LHD has an $l = 2/m = 10$ heliotron configuration with a natural divertor, where l and m are the poloidal and the toroidal mode numbers of the helical plasma, respectively. The present machine parameters are as follows: the magnetic field strength on the plasma axis can be varied up to 2.9 T; the major radius is 3.4 $-$ 4.1 m; the averaged minor radius is 0.6 m; and the plasma volume is 30 m^3.

Three heating methods are available; electron cyclotron heating (ECH): 2.1 MW, neutral beam injection (NBI): 10.3MW, and ion cyclotron heating (ICH): 2.7 MW. The energy confinement time in LHD is longer by a factor of more than 50 % than that obtained from the international stellarator scaling law [2]. The achieved plasma parameters are comparable to those of large tokamaks as follows: the highest central electron temperature is 10 keV; the highest central ion temperature is 7 keV; the highest β is 3.2 %; the highest stored energy is 1.2 MJ and the highest electron density is 1.6×10^{20} m^{-3}.

Target and achieved plasma parameters in LHD are shown in TableI, and target and achieved heating power in LHD are shown in TableII. The first goal of LHD experiment is to confine a fusion relevant plasma, such as the electron temperature of 10 keV and the

TABLE I: Target and achieved plasma parameters in LHD until July, 2003.

	Target	Achieved
T_e [keV]	10	10
T_i [keV]	7	7
n_e [10^{19} m^{-3}]	10	16
W_p [MJ]	3	1.2
β [%]	5	3.2
Duration [sec]	3,600	150

TABLE II: Target and achieved heating power in LHD until July, 2003.

	Target	Achieved
NBI [MW]	17	10.3
ECH [MW]	3	2.1
ICH [MW]	5	2.7

electron density of 10^{20} m^{-3}. Those targets have been already achieved. Residual targets are the plasma energy W_p, β value and the long pulse operation. Improved confinement is necessary to obtain high W_p. If the confinement is governed by the L-mode, the required power is 5 times larger than the present power in order to reach the target W_p.

In order to reach the goal, diagnostics will be more important not only for measuring plasma parameters but also for precise plasma control. In high β plasma, the magnetohydrodynamic (MHD) instability might be destabilized. As the duration time is longer, the plasma wall interaction gives larger effects to plasma, and edge plasma physics including diverter is more important. So, diagnostics to study physics of improved confinement, MHD physics and physics of plasma wall interaction are necessary to reach the goal of LHD. Also, diagnostics working in steady state should be developed. In LHD, standard diagnostics for plasma performance are important and most of them have been installed. Beside, diagnostics for steady state plasma are important to carry out the expected aim of LHD experiment. Considering LHD plasma is not axi-symmetric, two dimensional (2-D) or three dimensional (3-D) diagnostics are more useful in LHD than in axi-symmetric plasma, such as tokamak

TABLE III: Diagnostics for plasma operation in LHD.

Parameter	Diagnostics	Actuator
n_e	FIR Laser Interferometer	Gas puff
Min. n_e	Reflectometer	NBI Interlock
I_p	Rogowskii Coil	PF coil

and RFP plasmas.

The strategy of diagnostics in LHD is to assure the following features: (i) Reliable and robust diagnostics for operation (video, n_e, I_p, W_p, NBI interlock); (ii) Reliable and flexible diagnostics for fundamental plasma parameters (T_e, T_i, n_e) with reasonable accuracy; (iii) Diagnostics and data acquisition systems capable of steady state plasma operation; (iv) 2-D or 3-D capability of standard diagnostics for physical parameters (T_e, T_i, n_e, E_r, ECE, SX, Spectroscopy, Bolometer) for studies of the 3-D non-axisymmetric LHD helical plasma; (v) Advanced diagnostics for physics analysis with improvements in accuracy and innovative methods of which R&D should be carried out with domestic and international collaborations.

Following to the above-mentioned strategy of diagnostics in LHD, we constructed the diagnostic systems in pace with the LHD experiments. The arrangements of major diagnostics together with heating systems are schematically shown in Fig. ??. The categories of diagnostics and the corresponding diagnostic systems are summarized in the following sections.

In this paper, recent developments of plasma diagnostics in LHD will be reviewed. Standard diagnostics for plasma performance have been reviewed in the previous papers [3, 4]. This paper will rather focus diagnostics to study physics of improved confinement, MHD physics and edge plasma physics. This paper will also present development of 2-D and 3-D imaging diagnostics and innovative diagnostics in LHD.

DIAGNOSTICS FOR LHD OPERATION

Diagnostics for plasma operation in LHD are shown in TableIII. The operation of LHD is much easier than tokamaks, since plasma current is not required, and position control is not sensitive thanks to disruption free configuration. Once the superconducting magnets

are energized, plasma is generated and controlled by gas puffing and heating in LHD.

The plasma density is monitored by the 2-color mm-wave interferometer and the far infrared (FIR) laser interferometer [7].

The FIR laser beam is generated by CO_2 laser pumped CH_3OH lasers with wavelength 118.8 μm. The observed density resolution is 4×10^{17} m^{-3}. When the electron density is controlled, the gas puffing is automatically adjusted using the feedback control system so that the line averaged electron density that is monitored by the FIR laser interferometer may agree the target density. The plasma is usually generated by the electron cyclotron heating (ECH), but sometimes generated by the neutral beam injection (NBI). The NBI is tangentially injected, but the beam passes through when the electron density is very low. In order to minimize the damage on the wall, the NBI power is shut off with the density interlock system. The interlock system uses an O-mode homodyne reflectometer with the frequencies of 28.5, 34.2 and 40.8 GHz [8].

The plasma current is usually not important in LHD, but it is unexpectedly generated by the bootstrap current and the beam driven current. n the case of co-beam injection into a low density plasma, the plasma current sometimes exceeds 100 kA. In order to prevent unfavorable effect to the superconducting magnet coils, the plasma current is monitored by the magnetic diagnostics [9–11] and is limited. Sometimes, the plasma current is actively controlled by changing poloidal field (PF) coil current [12].

The reliability and robustness of the diagnostics for operation and feed-back control have been proved during the 6 experimental campaigns.

FUNDAMENTAL DIAGNOSTICS FOR OPERATION IMPROVEMENTS

Reliability and flexibility of the diagnostics for fundamental plasma parameters: T_e, T_i, n_e and the other essential parameters with reasonable accuracy are extremely important.

Electron Temperature

The YAG laser Thomson scattering system and the ECE system are proven as a reliable diagnostic for the temporal development of the electron temperature profile. The YAG laser Thomson scattering [13–15] works routinely to provide electron temperature profile every

TABLE IV: Standard diagnostics for plasma performance and confinement physics in LHD.

Diagnostics	Δt	Δx	Parameters	[References]
FIR Interferometer	10 μsec	10 cm	$< n_e(r,t) >$	[7]
CO_2+YAG Interferometer	10 μsec	1 cm	$< n_e(r,t) >$	[41–44]
YAG Thomson	0.001 - 0.1 sec	2 cm	$T_e(r,t)$, $n_e(r,t)$	[13–15]
ECE(Michelson)	50 msec	5 cm	$T_e(r,t)$	[16, 17]
ECE(Radiometer)	2 μsec	3 cm	$T_e(r,t)$	[18]
SX-PHA	0.1 sec	10 cm	$T_e(r,t)$	[19, 20]
HX-CCD	10 sec	10 cm	$T_e(r,z,t)$	[39]
Crystal Spectroscopy	0.1 sec		$T_i(0,t)$, Impurity	[21, 22]
CXS	0.1 sec	10 cm	$T_i(r,t)$, $E_r(r,t)$	[23]
Fast-CXS	10 msec	10 cm	$T_i(r,t)$, $E_r(r,t)$	
TOF-NPA	0.1 sec		$T_i(0,t)$, fast particle	[24, 25]
NDD-NPA	0.1 sec		$T_{tail}(t)$, fast particle	[26–28]
Si-NPA	0.1 sec		$T_{tail}(t)$, fast particle	[29, 30]
Bolometer array	1 msec	5 cm	$P_{rad}(r,z,t)$	[31, 33]

0.1 sec. The back scattered light of Nd:yttrium-aluminum-garnet (YAG) pulse laser beam, which has a wavelength of 1.058 μm, a pulse energy of up to 2 J, a pulse width of 20 ns, passes a 33 cm$\times$60 cm quartz viewing window, and is collected by a 150 cm$\times$180 cm mosaic mirror. An array of 200 fibers with a core diameter of 2 mm and a separation of 2.93 mm carries the collected scattered light to polychromators. In each polychromator, the scattered light is separated to different wavelength bands by 5 dichroic filters, and each band is detected by an avalanche photo diode. The YAG laser Thomson scattering system has a very good flexibility for the repetition rate (from ms to hundred ms) as shown in Fig. 1.

The magnetic field profile has a peak in the central region of the plasma in LHD, as shown in Fig. 2. Therefore, the full electron temperature profile with electron cyclotron emission (ECE) is measured using two antennas, one on the outboard side and one on the inboard side [16–18]. The ECE on the outboard side is detected by a Michelson spectrometer, which is absolutely calibrated to the blackbody radiation source. The ECE on the inboard side is detected by the heterodyne radiometer, which is cross calibrated to Michelson.a This

experiment was possible owing to the long pulse operation of LHD.

Soft X-ray Pulse Height Analyzer (SX-PHA) [20] is utilized to measure electron temperature profiles in addition to diagnose of line emission from impurities such as Fe, Cr and Ti. The electron temperature profiles measured by the ECE and the SX-PHA agree well with the data measured by the Thomson scattering system.

X-ray crystal spectroscopy for T_i measurement

The central ion temperature has been measured using a Johan-type x-ray crystal spectrometer with a cylindrical crystal bent to 3m in radius [21, 22]. Four crystals (quartz (2020), (2023), (3140) and (2243)) set at a rectangular crystal holder can be automatically selected by an external controller moving a detector position in order to measure He-like lines of Ar XVII, Ti XXI, Cr XXIII and Fe XXV, respectively. The curvature of the crystals was carefully checked in order to reduce the installation error less than 1 μm. The spectral line profile is measured by a CCD detector (active area: 13×13 mm^2, 1024×1024 channels). The resonance lines of Ar XVII (3.95 A) is routinely utilized for Doppler broadening measurements every 20 ms with small Ar gas puffing before the discharge. The lowest measured ion temperature was 0.2-0.3 keV for ArXVII and TiXXI. A highest $T_i(0)$ measured by this system (from Ar XVII) is 7 keV so far.

Charge exchange spectroscopy

Charge exchange spectroscopy (CXS) has been conveniently used to measure the profile of ion temperature and plasma rotation velocity and radial electric field (E_r) in LHD. By applying neon gas puff, the charge exchange line of fully ionized neon, NeX ($n = 11 \rightarrow 10$, $\lambda = 524.9$ nm) is used in LHD CXS [23]. A time resolution of the charge exchange spectroscopy should be improved in order to study the transitions of confinement phase. A new charge exchange spectroscopy system has been developed to increase time resolution of the E_r measurement. By using a back illuminated CCD with quantum efficiency of 80 % and camera lenses with F=2.8, the time resolution is 50 ms, which is 9 times improved from conventional CXS. The 50 fibers with a diameter of 200 μm are arranged at the entrance slit (100 μm) of spectrometer. Each fiber leads the light emitted from different radial position

in plasma to the spectrometer. The pixel size, the width and height of the CCD detector are 12 μm, 652 pixels and 496 pixels, respectively. The instrumental width is 0.08 nm and the wavelength range of the spectrum image is 5.7 nm.

Diagnostics for fast neutral particle

Fast neutral particle measurement is great concern in the ripple transport in helical field, the high energy ion tail during heating in LHD. The time of flight - neutral particle analyzer (TOF-NPA) is useful to measure energy spectra of fast particles from 0.5 to 300 keV [24, 25]. The pitch angle distribution can be obtained by scanning the analyzer. High energy neutral particles are also detected by Si diodes [29, 30] and by Natural diamond detectors (NDD) [26–28] in LHD. By using the pulse height analysis technique, energy spectra of fast particles is obtained from these semiconductor dtectors.

IMAGING DIAGNOSTICS

2-D or 3-D imaging diagnostics are intensively developed with national and international collaborators in LHD: Tangential cameras (Fast SX, Bolometer, photon counting CCD, H_α CCD); tomography (tangential SX CCD, AXUV); mm wave imaging (ECE, Reflectometer).

Bolometric imaging

The infrared imaging video bolometer (IRVB) has been developed and mounted on a LHD tangential port. This diagnostic utilizes a thin (0.001 mm) gold foil mounted in a frame to detect the radiation and neutrals from the plasma, which are incident on the foil through a 1 cm diameter pinhole. The resulting temperature distribution on the foil is measured using an AGEMA THV 900 LW infrared camera having 136×272 pixels with a frame rate of 15 Hz and a nominal sensitivity of 80 mK. Using a numerical technique the spatial and temporal derivatives of the temperature distribution on the foil are calculated and the incident power density on the foil is determined using a calibration of the foil obtained by means of a He-Ne laser. The resulting 10×14 pixel view of the plasma radiation at a 15 Hz frame rate has a noise equivalent power density of 0.5 mW/cm^2. An image of the plasma radiation during a

discharge using the inboard vacuum vessel wall as a limiter shows radiation localized near the limiting surface.

The absolute extreme ultraviolet silicon photodiode (AXUVD) arrays are installed in LHD [33]. The sensitivity of the AXUVD in most of the XUV region is flat and equal to 0.27 A/W. All the channels have been absolutely calibrated to two arrays (16 and 19 channels) installed in the normal LHD cross section and to two other arrays (20 and 20 channels) in a semi-tangential plasma cross section. Tomographic reconstruction using a singular value decomposition (SVD) technique has been developed for the total radiation power distribution from the AXUVD data [34]. The 2-D inversion uses a 2-D peeling away algorithm, improved by a feedback procedure. The emitting region is divided into a number of layers using the magnetic flux contours calculated using the VMEC code [35] assuming a certain β close to the experimental value derived from the diamagnetic loop measurements. Then the emission at each magnetic flux layer is assumed to be a function of poloidal angle θ. The expansion coefficients are determined by a least-square fit to the brightness of the chords. These measurements and analysis techniques have enabled us to visualize asymmetries in plasma emission due to pellet and gas fueling.

ECE imaging

A 3-D ECE imaging system is under development in LHD [36]. The imaging system consists of focusing optics installed inside the vacuum chamber of LHD and planer-type detectors fabricated by monolithic microwave integrated circuit technology. The detector consists of the integration of a bowtie antenna, a down-converting mixer using a Schottky barrier diode, and heterojunction bipolar transistors (HBTs) on a GaAs substrate. The HBTs work as an intermediate frequency (IF) amplifier with a 10 GHz bandwidth and a 10 dB voltage gain. The ECE signal and local oscillator beam are irradiated from both sides of the detector. The ECE signals are down-converted at the mixers and the IF signal is fed to a filter bank with center frequencies of 1-8 GHz. The obtained ECE signals agree with the ECE measurement by Michelson.

Tangential soft X-ray camera

A high-speed tangentially viewing soft x-ray camera system has been developed and installed in LHD [37, 38]. It consist of a vacuum-tight beryllium window (25 or 40 μm thick), a 1 mm diameter pinhole camera with a 10 cm diameter CsI coated scintillator screen, where the soft X-ray is converted to visible light. The visible image is tranffered to a image intensifier system by a 9 m long optical fiber bundle (100×100 fibers with 0.75 μm diameter core) in order to avoid a magnetic stray field. The image intensifier system consists of an electron-beam-imaging amplifier with P47 phosphor, and is further reduced by a tapered fiberoptic plate and subsequently intensified by a two-stage MCP amplifier. Finally, the image is recorded by a high-speed video camera with the framing rate of 3.5 kHz for a reduced frame of 128X 128 pixels. In LHD, the coherent fluctuation component is comparable to or even lower than the noise level, so the method of singular value decomposition (SVD) has been developed to identify coherent fluctuations in space and time within a background of noise. An example of the SVD components is shown in Fig. 3. A slow (500-1000 Hz) MHD oscillation is observed in a inward-shifted plasma ($R_ax = 3.53m$). A rotating $m = 2$ structure can be constructed from three components (U2-U4) in Fig. 3. The (2,1) mode structure is also confirmed by the magnetic probe array. We have been able to successfully extract relevant fluctuating components using SVD, even though the fluctuation level is comparable with that of the noise.

Hard X-ray imaging for electron temperature profile

Two-dimensional profiles of energy spectra of x-ray emission are measured with the photon counting hard X-ray CCD camera by optimizing the intensity of x-ray with attenuation by Be and Al filters [39]. Since half of the pixels are devoted to storage area, the imaging area has 1242×576 pixels. The time resolution determined by the mechanical shutter is ~100ms. The two-dimensional profiles of the electron temperature are derived from energy spectra measured using the hard x-ray CCD camera. Comparison between the SX data and the Thomson data is done for the plasmas with and without ITB as shown in Fig. 4. It is revealed that both the data agree well. Such situation is seen also for the plasma heated with ECH and NBI. This fact suggests that the energy distribution of electrons is close to

the Maxwellian in the energy range of the YAG and the x-ray CCD measurements.

Soft X-ray imaging for Shafranov shift

The x-ray imaging system with a soft x-ray back-illumination CCD detector sensitive to the energy range of 1keV to 10keV has been applied to measure the magnetic axis shift [40]. The system has good spatial resolution (1024×512 pixels in image area). By choosing the appropriate combinations of pinhole size and thickness of Be filters, the x-ray image can be measured for the plasmas in a wide range of electron temperature and density. The major radius of the magnetic axis (R_{ax}) is derived by choosing the magnetic flux surface from a database, which gives the best fit to the measured two-dimensional x-ray profile. The Shafranov shift measured with this method increases linearly as the averaged beta $< \beta_{dia} >$ is increased. The scatter of the Shafranov shifts measured are beyond the error bar of the measurements and is mainly due to the change of the pressure profiles for the identical $< \beta_{dia} >$. The Shafranov shift depends on not only the averaged beta but also on the peaking degree of plasma pressure profiles. Recently from the data of this tangential SX-CCD camera a tomographic image is reconstructed, and the static (2,1) magnetic island is found.

CO_2 laser imaging interferometer

A CO_2 laser ($\lambda = 10.6$ μm) imaging interferometer has been developed and installed to measure the precise n_e profile in LHD [41–43]. For the compensation of vibration, YAG laser ($\lambda = 1.06$ mum) interferometer is coaxially installed on the CO_2 laser interferometer. The whole system is installed on the unti-vibration structure for the FIR laser interferometer . Frequencies of laser beams are shifted by acousto-optic modulators (AOM), so that the phase is modulated with the frequency of 1 MHz. Then the CO_2 and YAG laser beams are combined and expanded to slab-like beams (250×50 mm^2), which are injected into the LHD plasma vertically. The CO_2 and the YAG lasers are detected by the 32 channel HgCdTe detector and avalanche photo-diode (APD) arrays, respectively The phase is detected by comparing the IF signal and the original 1 MHz clock. In LHD, the n_e profile has a steep gradient at the edge, and the diffraction of the laser beam with longer wavelength may cause

large error on the n_e measurement. Still the CO_2 laser interferometer is useful to measure the precise density profile at the plasma edge. In order to measure the n_e fluctuations, the phase contrust imaging technique is utilized in this interferometer [43]

DIAGNOSTICS FOR EDGE PHYSICS

Reflectometer

A four channel pulsed radar reflectometer system has been installed on LHD [45, 46]. Pulsed radar reflectometry is useful, because it measures the delay time of the reflected wave, not the phase, and X-mode and O-mode polarized waves can be distinguished. Four Gunn oscillators are used as a source. The frequencies of the oscillators are 33, 39, 60, and 65 GHz. The output power of each is about 100 mW. A p-i-n switch is used as a pulse modulator that uses the tuned signal of the generated impulse output. Separate transmitter and receiver horns are used in order to avoid the mixture of spurious reflecting components. The reflected waves is mixed with the local microwave with the frequencies of 51 GHz for R band and 78 GHz for V band. The intermediate frequency signals are filtered by band path filters with a bandwidth of 2 GHz and then detected. Each pulse width is 2 ns and the repetition rate is 200 kHz in standard operation. The time-of-flight (TOF) measurement is carried out with the reference pulses, of which detectors are located before the antenna to avoid jitter from the pulse generator and the p-i-n switch. By using X-mode operation of the pulsed radar reflectometer, the critical density where the microwave is reflected is about $1\times\ 10^{16}$ m^3. Therefore, the X-mode reflectometer is useful to study edge plasma physics.

Li beam probe

A 30 keV lithium beam probe system to measure edge density and its fluctuation has been developed in LHD [47]. The beam current is 0.1 mA and no unfavorable beam divergence is observed in spite of a long distance more than 6 m from the injector. The beam penetrates up to $\rho = 0.8$. The lithium beam system consists of a beam injector and an optical detector. The electrostatically accelerated beam is injected to the plasma through the charge-exchange cell. The electron density profile is reconstructed from visible light, which is emitted from lithium atoms in the plasma due to the electron impact excitation. Electron impact, charge-

exchange processes and beam attenuation are considered in the reconstruction. The light emission from the Li beam is detected by the detector array with narrow band filter for the emission wavelength.

Electrostatic probe

The particle flux is measured by a Langmuir probe array embedded in the divertor tile. It has a spatial resolution of 5 mm [48, 49]. The peak of the particle flux appears at the positions of the long magnetic field lines calculated in each case of magnetic axis positions: R_{ax} = 3.6 m and R_{ax} = 3.75 m. Ion saturation current profile is also measured with fast scanning probe for observing helical diverter property. The scanning velocity of the probe is 3 m/s. Peak positions of ion saturation current profile agree well with those of field line connection length profile, which are seen as layers in the H_α CCD camera image [50].

Spectroscopic measurement using Zeeman effect

From the emission line profile of He I (λ = 728.1 nm :$2^1P - 3^1S$) observed with the 80 chord array, the intensity distribution around the stochastic layer is obtained. Figure 5 shows an example of the line profile of HeI line (λ =728.1nm) that is Zeeman splitted in LHD field. Locations of neutral emission He I are determined precisely using Zeeman effect, since the magnetic field is different at the different position on the same line of sight under the assumption that the line emission is localized [51]. Such emission comes from the divertor surface.

DIAGNOSTICS FOR STEADY STATE OPERATION

One of important features of LHD diagnostics is compatibility with long pulse operation [52]. Diagnostics for steady-state operations can be classified as either those for real-time monitoring or those for feed-back control. Real-time monitoring is necessary to insure that certain parameters do not exceed the limits of safe operation. Feedback control is necessary when one measured parameter is used to control a device in order to maintain the plasma in a steady-state condition. Long pulse operation up to 150 s was successfully conducted

TABLE V: Spectroscopy in LHD.

Spectroscopy	λ [nm]	$\Delta\lambda$ [nm]	[Refs.]
SOXMOS	0.1 - 130	0.1	[54]
VUV	30 - 310	0.005	[55]
UV/Visible	200 - 800		[56]
Crystal	0.17 - 0.4	10^{-4}	[22]
SX-PHA	0.4 - 200 [keV]	0.4 [keV]	[19, 20]

and recorded with complete data acquisition.

Impurity Diagnostics

Since the LHD experiment aims to confine high performance plasma, impurity accumulation due to plasma-wall interaction is revealed one of the most severe problems in the steady state operation. Table V present pectrometers for the detection of impurity line emissions in LHD. Figure 6 shows time evolution of emission of impurity lines, the electron temperature, the electron density and the radiation power during the long pulse operation. The electron temperature and the electron density are measured by ECE [16, 17] and by the FIR laser interferometer [7], respectively. In this plasma, the electron density starts to increases 10 seconds after turning off the hydrogen gas puffing. Correspondingly, the electron temperature decreases and the radiation power increases.

The impurity line emissions are measured by a high-resolution, time-resolving soft x-ray duo-multi-channel spectrometer (SOXMOS) [53, 54]. Intensity of impurity lines is averaged during the time width of 10 sec, and is normalized at t=15 sec. So finite values of the neon and oxybgen emission at 65 sec indicate the strong emissions near t=60 sec. SOX-MOS spectrometer reveals that neon gas comes out from wall after t=50 sec and finally it causes radiation collapse. This plasma was produced with hydrogen gas and NBI, but neon plasma experiment had been done in previous days. Therefore the saturation of wall pumping and desorption of gas, which is adsorbed on the walls, take place in the steady state plasma, and they terminate the long pulse discharge.

Magnetic diagnostics

Magnetic Probes

The toroidal flux is measured by a poloidal loop on the inner surface of the vacuum vessel. Careful compensation of the stray filed is necessary to obtain the internal plasma energy (W_p) and the β value. The stray field comes from the plasma current, the coil currents and the eddy current in the vessel wall and other structures of the vessel and coils. The current in coils and structures are measured by the use of the Rogowskii coils. The current in the vacuum vessel is estimated by solving circuit equations. Some mutual inductances between the diamagnetic loops and other components are directly measured, and some are estimated by the calculation of the Biot-Savart equation. Since the external flux due to the eddy current is as large as the plasma flux, those effects are carefully compensated in LHD [62].

Integrator for the steady state

Integrators are required for the magnetic measurement. The new-type integrator is developed for LHD. This integrator is made of three analog integrators and digital processing system. A time slice of magnetic signal is separated to three different short time slices. Each short time slice is integrated by a corresponding analog integrator and is digitized. By accumulating integrated signal digitally, the whole integrated signal is obtained. Integrated signals are transferred to VME system with DEC Alpha processor, where the integrated data are delivered to the real time display, the LABCOM data management system and to the control system. The integrator avoids saturation of integrated signal as the integration is made during a short time slice. Therefore, the integrator will work in the steady state operation.

Mortional Stark Effect

A mortional Stark spectroscopy (MSE) has been developed for measurement of magnetic field pitch angle in LHD [?]. The spectrometer consistes of a zigzag CCD as a detector and ferroelectric liquid crystal cells for the polarization modulation. The pitch angle is derived

from the polarization angle of σ and π components in the H_α line. Experimental result is as follows: the location of zero pitch angle is shifted 28 ± 16 mm in outboard side due to the Pfirsh-Schluter current as expected by the equilibrium calculation.

Polarimetry for the density measurement

A 3 channel CO_2 laser polarimeter has been developed in LHD to measure the Faraday rotation [57]. Interferometry, which is used on almost all magnetically confined fusion devices and has high resolution, needs a time history. The Faraday rotation is considered as a monitor of the electron density in the steady state plasma. The polarimeter in LHD utilizes the frequency-shift heterodyne technique with the use of acousto-optic modulators for high resolution. By utilizing the digital complex demodulation technique, the accuracy of the Faraday rotation angle with a time resolution of 16 ms is ~ 0.01 degrees, which is 100 times less than the total angle. The electron density obtained by the CO_2 laser polarimeter agrees well with that obtained by the FIR laser interferometer.

Data acquisition and storage/retreival system

A data acquisition system with parallel processing technology has been developed for diagnostics in 3 minutes cyclic LHD operation [58, 59]. Data of most diagnostics are taken by CAMAC systems. The total number of CAMAC modules and channels in LHD are about 300 and 2000, respectively. The raw data size is up to 740 MB/shot with 150 shots/day in the 2002 experimental campaign. The data acquisition system is made by a cluster of personal computers (PC), which acquires the data from own CAMAC crate, compresses them, and stores them in own hard disk. The data is also stored in the mass storages as follows: RAID hard disk systems; Magneto-optical-disk (MO) juke-boxes (3.6 T bytes); A digital-versatile-disk (DVD) changer (3.2 T bytes). The data are managed using the object-oriented-data-base technology (ObjectStore). A LINUX server named 'name server' keeps a indexing meta-table using the relational-data-base technology (PostgreSQL), as a user obtain the data immediately.

In the steady state operation, data are continuously digitized at 1 kHz with Yokogawa WE7000 modular PC-based instrumentation system [60]. Some of data are displayed on the

TABLE VI: Diagnostics for fluctuations and MHD Physics in LHD.

Parameter	Diagnostics	[Ref.]
$\tilde{T}_e$	ECE(Radiometer)	[18, 69]
$\tilde{n}_e$	CO_2 Laser Phase Contrast	[43]
$\tilde{n}_e$	Reflectometer (Pulse, Ultra-short pulse)	[45, 46]
X-ray	SX diode array	[63]
$\tilde{B}_\theta$, $\tilde{B}_\phi$	Mirnov Coil	[64, 65]

real time monitor, and help the experimentalists for implementing the steady state operation of LHD. The real-time data monitoring system using IP multicast technology is also under development to monitor plasma parameters continuously in the LHD long-pulse operation [61]. Since the IP multicast packets are sent to the sub-net, where clients receive the data, the network load and server load will be drastically reduced comparing to the one-to-one connection.

DIAGNOSTICS FOR MHD BEHAVIOR

Magnetohydrodynamic (MHD) behavior is monitored with soft X-ray (SXR) detector arrays [63], Mirnov coil arrays [62], and ECE systems [17, 18, 18]. PIN photodiode arrays are installed in two vertical port sections separated by a toroidal angle of 72 degrees. In one section, 40 PIN diodes are set in a top port and 40 in a bottom port, and in another section, 40 PIN diodes are set in a top port. In LHD, 64 Mirnov coils and 24 saddle loops are installed inside the vacuum vessel in order to measure magnetic fluctuations. The AT (Advanced Technology) probe has been developed [64]. AT probe is suitable for the steady state operation since it is heat resistant up to 1000 °C. Although the Mercier criterion is violated in most LHD plasmas when R_{ax} = 3.6 m, significant MHD activity has not been observed yet [65].

Sometimes fluctuations are observed with Mirnov coils, but large fluctuations have not been observed in SXR and ECE signals. Alfven-eigen-modes such as TAE, C-TAE, G-TAE, GAE, HAE, EAE are studied using Mirnov coils in wide parameter range [66, 67]. Those modes are excited by the fast ions from the 180 keV N-NBI in LHD. Sawtooth crash is

observed in the core region of the high β and high counter-I_p plasmas. T_e in the core drops and T_e in the peripheral region increases, and the heat pulse propagates toward outside as in tokamaks. Full sawtooth crash in helical system is not well understod as the $m = 1$ mode should not be unstable because of $q_0 \sim 3$ [69].

INNOVATIVE DIAGNOSTICS

heavy ion beam probe (HIBP)

A heavy ion beam probe (HIBP) can measure the plasma potential, its fluctuation and the electron density fluctuation simultaneously. In LHD, a 6 MeV HIBP is under construction. In this device, a singly charged negative gold ion beam (Au-) is accelerated with a 3 MV tandem accelerator at first. It becomes a positively charged ion beam when it passes through a charge stripping cell in the accelerator. It is accelerated again and obtains another 3 MeV energy. The singly charged positive gold ion beam (Au+) is swept and focused into the LHD plasma using electrostatic sweepers and lens. The secondary beam from the plasma is analyzed using a new tandem-parallel-plate analyzer which works in smaller anode voltage compared with conventional parallel-plate analyzers, and it is under development.

Tracer-Encapsulated Solid Pellet (TESPEL)

A Tracer-Encapsulated Solid PELlet (TESPEL) injection is one of the simplest idea to study the confinement of impurity [70]. Figure 7(a) shows a schematic view of a TESPEL ball which consists of polystyrene polymer (-CH(C6H5)CH2-)n as an outer shell, the diameter of which ranges from 300 to 900 μm, and tracer particles as an inner core. A tracer impurity can be locally deposited by TESPEL injection. The local deposition is really proven by observation of the light emission from the pellet with combining a spectrometer and a fast intensified-CCD camera. Time evolution of the ablation light (dominantly H_β line) is shown in Fig. 7(b). The pellet ablation started at the frame No. 6 and ends the frame No. 17. The interval between each frame corresponds to 84 ms in this case. The spectrum changes suddenly at the frame No.16, which shows the ablation of titanium, while until the frame No 15 the H_β line is dominant (the broad width is due to the Stark broadening) together with a CI line (493.2 nm) because of the usage of polystyrene shell. The timing is consistent

with the observation with the photomultiplier and a narrow band pass filter, and the total duration of the ablation emission of about 1ms is also consistent with the above observation.

Diffusion coefficient can be directly measured from the temporal evolution of impurity emission. The temporal evolution of the impurity emission in case of a titanium (Ti) tracer in the plasma with $< n_e > \sim 3 \times 10^{19}$ m^{-3} is shown in Fig. 8. The upper figure corresponds to the highly ionized Ti impurity: Ti K_α (He-like; E=4.7 keV) and the lower figure to Ti XIX (λ = 16.959 nm). These are measured by a soft x-ray pulse height analyzer [19] and a vacuum ultraviolet spectrometer SOXMOS [54], respectively. Observed decay time of the Ti K_α emission is fairly longer, while the Ti XIX emission is shorter. A transport analysis with the MIST code based on the evolutions of both line emissions resulted in the diffusion coefficient of D=0.6 m^2/sec and the inward convection velocity of V(a)= 0.76 m/sec. The inward convection cannot be explained by the neoclassical impurity transport. So, the effect of a radial electric field and/or some other effect should be taken into account additionally. The advanced application of TESPEL to particle transport study is to observe light emission due to charge exchange recombination of a tracer with a heating neutral beam. This has an advantage in the possibility of direct measurement of the local particle transport. The most adequate atom as a tracer for this purpose is now under investigation.

Cold Pulse

Owing to the flexibility of the size and material, the TESPEL injection makes a sudden drop in the electron temperature in the middle of plasma ($\rho \sim$0.5), the temperature drop (so called cold pulse) propagates across the flux surfaces. The $T_e(r,t)$ profile is measured every 5 musec with the 32 channel radiometer [18] covering R_{ax} = 2.9 – 3.5 m. By using cold pulse propagation induced by TESPEL, the electron heat conductions inside and outside the magnetic island structure are measured. The transport equation for the perturbation can be written as

$$\frac{3}{2} n_e \frac{\partial \delta T_e}{\partial t} = \frac{\partial}{r \partial r} \left(r n_e \chi \frac{\partial \delta T_e}{\partial r} \right) , \qquad (1)$$

This equation is solved numerically and compared with the experimental data, the heat conduction coefficient χ_e is obtained. It is observed that the electron heat conductivity (χ_e = 0.2 m^2/s) in the island is much lower than that in main plasma ((χ_e = 2 m^2/s) [72]. This dynamic measurement of heat conduction is consistent with the estimation from the

temperature and density profiles. This is the first direct measurement of heat conduction inside the magnetic island. This technique is also applied to analyze the heat transport in the ITB region of LHD plasmas.

SUMMARY

In this article diagnostics employed on LHD are reviewed. Standard diagnostics for fundamental plasma parameters (T_i, T_e, n_e) and for plasma physics (E_r, Impurity, Confinement, MHD) are routinely utilized for daily operation and physics study in LHD. Diagnostics for steady state plasma are intensively developed in LHD: CO_2 laser polarimeter, Data acquisition and storage/retreival system, integrator for magnetics in steady state. 2-D or 3-D imaging diagnostics are intensively developed in LHD: Tangential cameras (Fast SX, Photon counting CCD, H_α CCD), 2-D imaging (Bolometer, ECE, Reflectometer), and Tomography (Tangential SX CCD, Bolometer camera). Diagnostics for helical diverter, which is far different from tokamaks, are developed and installed in LHD. Advanced diagnostics are being intensively developed with national and international collaborators in LHD. Most of the diagnostics are working reliably with flexibility and reasonable accuracy owing to the well planned introduction of different types of methods for important parameters.

TThis work was supported by the Ministry of Education, Culture and Science.

[1] Motojima O et al 1999 Phys. Plasma **6**, 1021.

[2] Stroth U et al. 1996 Nuclear Fusion **39**, 1063.

[3] Sudo S et al 2001 Rev. Sci. Instrum **72**, 483.

[4] Sudo S et al 2003 Plasma Phys. Control. Fusion **45**, 1127.

[5] Komori A et al 2003 Plasma Phys. Control. Fusion **45**, 671.

[6] Kawahata K et al 1999 Rev. Sci. Instrum. **70**, 695.

[7] Kawahata K et al 1999 Rev. Sci. Instrum. **70**, 707.

[8] Tanaka K et al 2001 Proc. 5th Int. Workshop on Reflectmetry, NIFS-PROC-**49** (NIFS, Toki, Japan), pp.88.

[9] Sakakibara S et al 2000 J. Plasma Fusion Res. SERIES **3**, 109.

[10] Watanabe K Y et al 2002 J. Plasma Fusion Res. SERIES **5**, 124.

[11] Sakakibara S et al 1997 J Proc. European Phys. Soc. Conf. **21A**, 797.

[12] Takami S et al 1999 Proc. Meeting Eng. Tech. Basic Res. (http://www-eng.kek.jp/giken/procedng/index.pdf).

[13] Narihara K et al 2001 Rev. Sci. Instrum **72**, 1122.

[14] Yamada I et al 2001 Rev. Sci. Instrum **72**, 1126.

[15] Yamada I et al 2001 Rev. Sci. Instrum **74**, 1675.

[16] Nagayama Y et al 2001 Fusion Eng. Design **53**, 201.

[17] Nagayama Y et al 2003 J. Plasma Fusion Res. **79**, 601.

[18] Kawahata K, Nagayama Y, Inagaki S 2003 Rev. Sci. Instrum **74**, 1449.

[19] Muto S, Morita S 2001 Rev. Sci. Instrum **72**, 1206.

[20] Muto S et al 2003 Rev. Sci. Instrum **74**, 1993.

[21] Morita S et al 2002 Nucl. Fusion **42**, 1179.

[22] Morita S, Goto M 2003 Rev. Sci. Instrum **74**, 2375.

[23] Ida K, Kado S, Liang Y 2000 Rev. Sci. Instrum **71**, 2360.

[24] Ozaki T 2000 Rev. Sci. Instrum **71**, 2698.

[25] Ozaki T 2002 J. Plasma Fusion Res. SERIES **5**, 201.

[26] Krasilnikov A V et al 2002 Nucl. Fusion **42**, 759.

[27] Isobe M et al 2001 Rev. Sci. Instrum **72**, 611.

[28] Saida T, Sasao M, Isobe M and Krasilnikov A V 2003 Rev Sci. Instrum. **74,** 1883.

[29] Osakabe M et al 2001 Rev. Sci. Instrum **72,** 788.

[30] Goncharov P R 2003 Rev Sci. Instrum. **74,** 1869.

[31] Peterson B J et al 2001 J. Nucl. Material **290-293,** 930.

[32] Peterson B J et al 2001 Rev. Sci. Instrum **72,** 727.

[33] Peterson B J et al 2003 Plasma Phys. Control. Fusion **45,** 1167.

[34] Liu Y, Kostrioukov A Yu, Peterson B J 2003 Rev Sci. Instrum. **74,** 2312.

[35] Hirshman S P, Lee D K 1986 Comput. Phys. Comm. **39,** 143.

[36] Mase A et al 2003 Rev. Sci. Instrum **74,** 1445.

[37] Ohdachi S, Toi K et al 2003 Rev. Sci. Instrum **74,** 2136.

[38] Ohdachi S, Toi K 2001 Rev. Sci. Instrum **72,** 724.

[39] Liang Y et al 2001 Rev. Sci.Instrum, **72,** 717.

[40] Liang Y, Ida K 2002 Plasma Phys. Control. Fusion **44,**1383.

[41] Tanaka K et al 2001 Rev. Sci. Instrum **72,** 1089.

[42] Akiyama T et al 2003 Rev. Sci. Instrum **74,** 1638.

[43] Tanaka K et al 2003 Rev. Sci. Instrum **74,** 1506.

[44] Tanaka K et al 2002 Plasma Phys. Control. Fusion **44,** A231.

[45] Tokuzawa T et al 2001 Rev. Sci. Instrum **72,** 328.

[46] Tokuzawa T et al 2003 Rev. Sci. Instrum **74,** 1506.

[47] Morisaki T et al 2003 Rev. Sci. Instrum **74,** 1865.

[48] Masuzaki S et al 2002 Nucl. Fusion **42,** 750.

[49] Masuzaki S et al 2002 Plasma Phys. Control. Fusion **44,** 759.

[50] Shoji M et al 2000 J. Plasma Fusion Res. SERIES **3,** 440.

[51] Goto M and Morita S 2002 Phys. Rev. E **65,** 026401.

[52] Nakamura Y et al 2003 Plasma Phys. Control. Fusion **45,** 219.

[53] Schwob J L, Wouters A W, Suckewer S, Finkenthal M 1987 Rev. Sci. Instrum **58,** 1601.

[54] Kobuchi T, Sato K et al J. Plasma Fusion Res. to be pulished.

[55] Morita S and Goto M 2003 Rev Sci. Instrum. **74,** 2036.

[56] Kobuchi T et al 2000 J. Plasma Fusion Res. SERIES **3,** 121.

[57] Akiyama T et al 2001 Rev. Sci. Instrum **72,** 1073.

[58] Nakanishi H et al 2000 Fusion Eng. Design **48,** 135.

[59] Nakanishi H et al 2001 Fusion Eng. Design **56-57**, 1011.

[60] Yamaguchi Y et al 1998 Proc. IMEKO TC-4 Symposium on Development in Digital Measuring Instrumentation and 3-rd Workshop on ADC Modeling and Testing (Naples, Italy, 1998) **1**, 229.

[61] Emoto M et al 2002 Fusion Eng. Design **60**, 367.

[62] Sakakibara S et al 2001 Nucl. Fusion **41**, 1177.

[63] Ohdachi S, Toi K 2001 Rev. Sci. Instrum **72**, 727.

[64] Takahashi H et al 2001 Rev. Sci. Instrum **72**, 3249.

[65] Sakakibara S et al 2002 Plasma Phys. Control. Fusion **44**, A217.

[] Takayama S et al 2003 Rev. Sci. Instrum **74**, 78.

[66] Yamamoto S et al 2000 J. Plasma Fusion Res. SERIES **3**, 117.

[67] Toi K et al 2000 Nucl. Fusion **40**, 1349.

[68] Yamamoto S et al submitted to Phys. Rev. Lett.

[69] Nagayama Y et al 2003 Phys. Rev. Lett. **90**, 205001.

[70] Tamura N et al 2003 Plasma Phys. Control. Fusion **45**, 27.

[71] Sergeev V Yu et al 2002 Plasma Phys. Control. Fusion **44**, 277.

[72] Inagaki S et al submitted to Phys. Rev. Lett.

[73] Goto M et al 2003 Phys. Plasmas **10**, 1402.

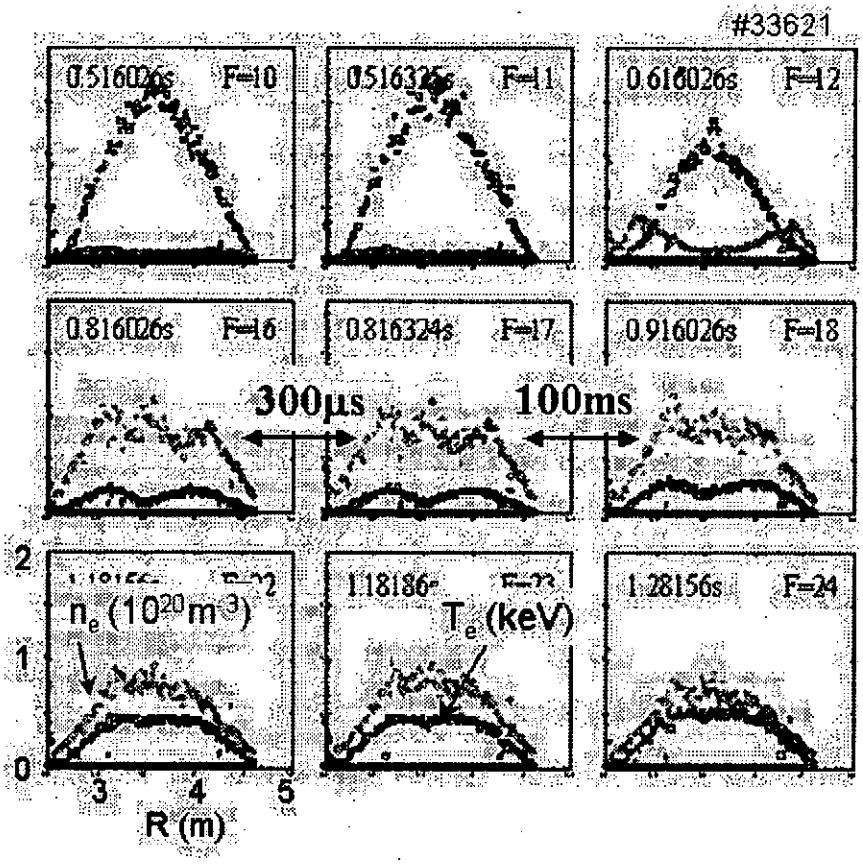

FIG. 1: Evolution of T_e and n_e profiles measured by the YAG laser Thomson scattering. The YAG laser Thomson scattering system has a very good flexibility for the repetition rate (from μs to hundreds ms) in addition to the good spatial resolution at 200 spatial points. For example, the interval from Frame No.16 to Frame No. 17 is 298 μs, and the interval from Frame No.17 to Frame No. 18 is about 300 ms owing to the multiple laser system.

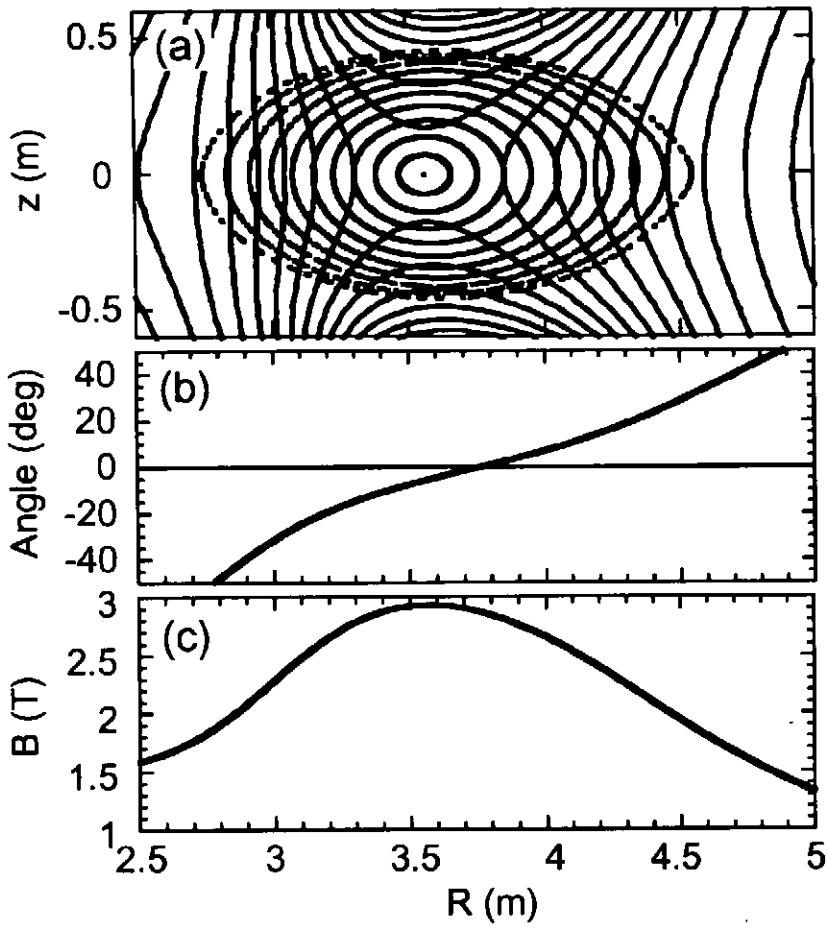

FIG. 2: (a) Contour plot of magnetic field (solid contour) and flux surface (dotted contour). (b) Radial magnetic field profile on the sight line of ECE diagnostics. (c) Field angle of the magnetic field.

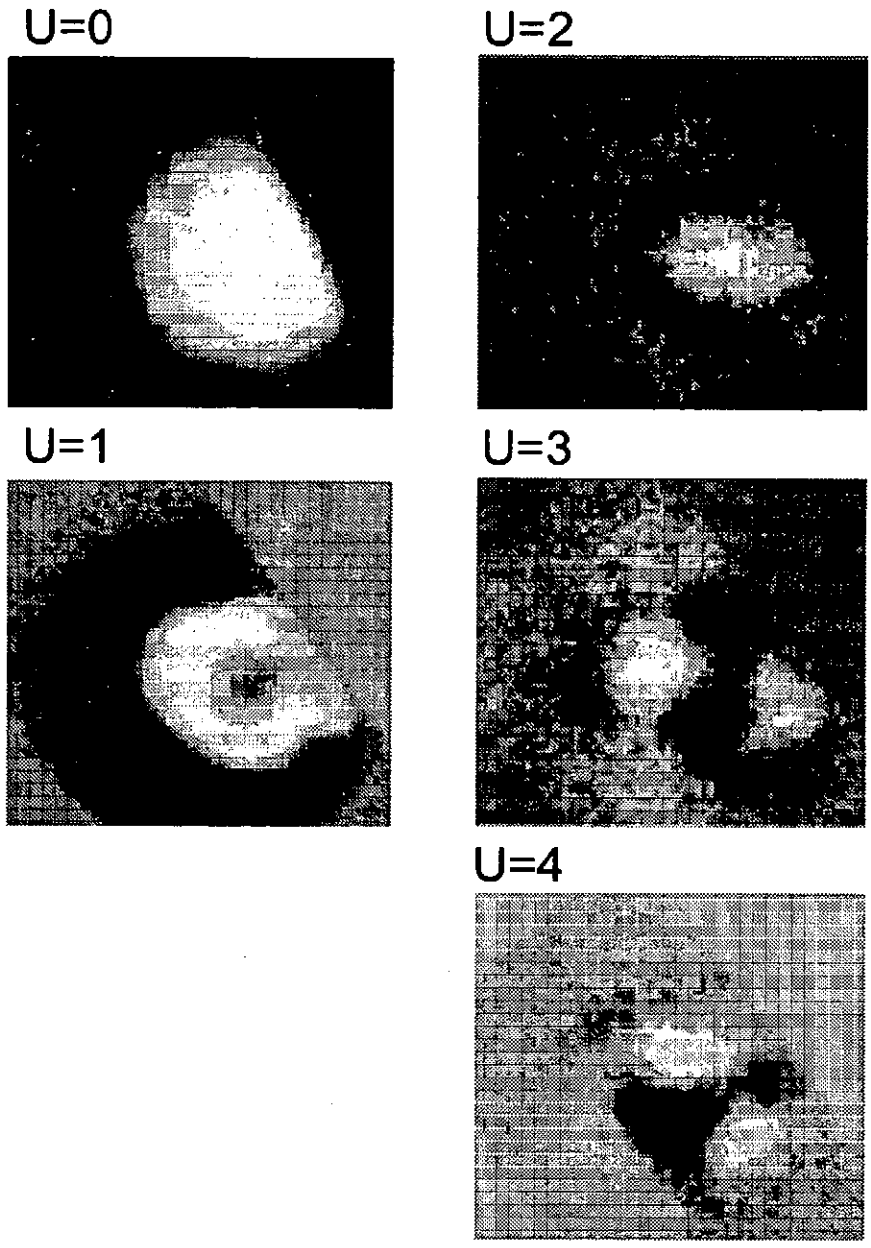

FIG. 3: The topos SVD components of the tangential SX image.

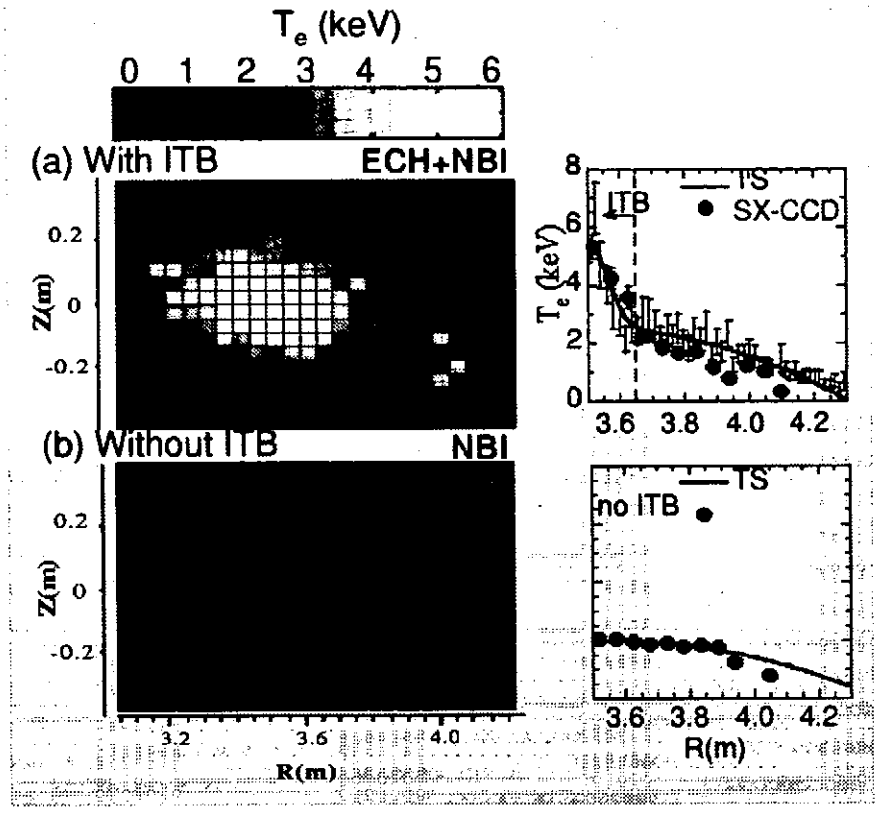

FIG. 4: 2-D T_e profile obtained by X-ray CCD camera. The X-ray T_e agree well with the Thomson T_e both for the plasmas with and without ITB.

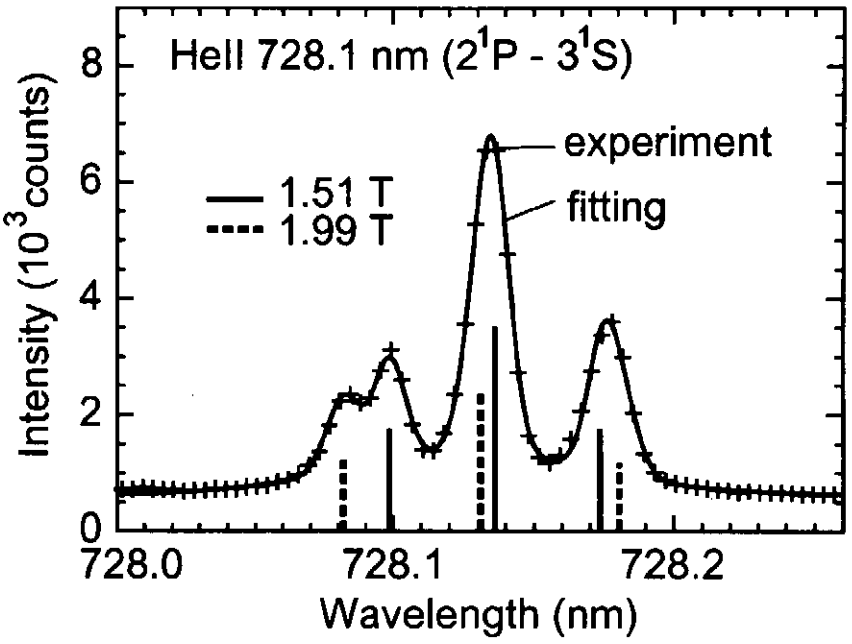

FIG. 5: Line profile of HeI line (λ =728.1nm) that is Zeeman splitted in LHD field.

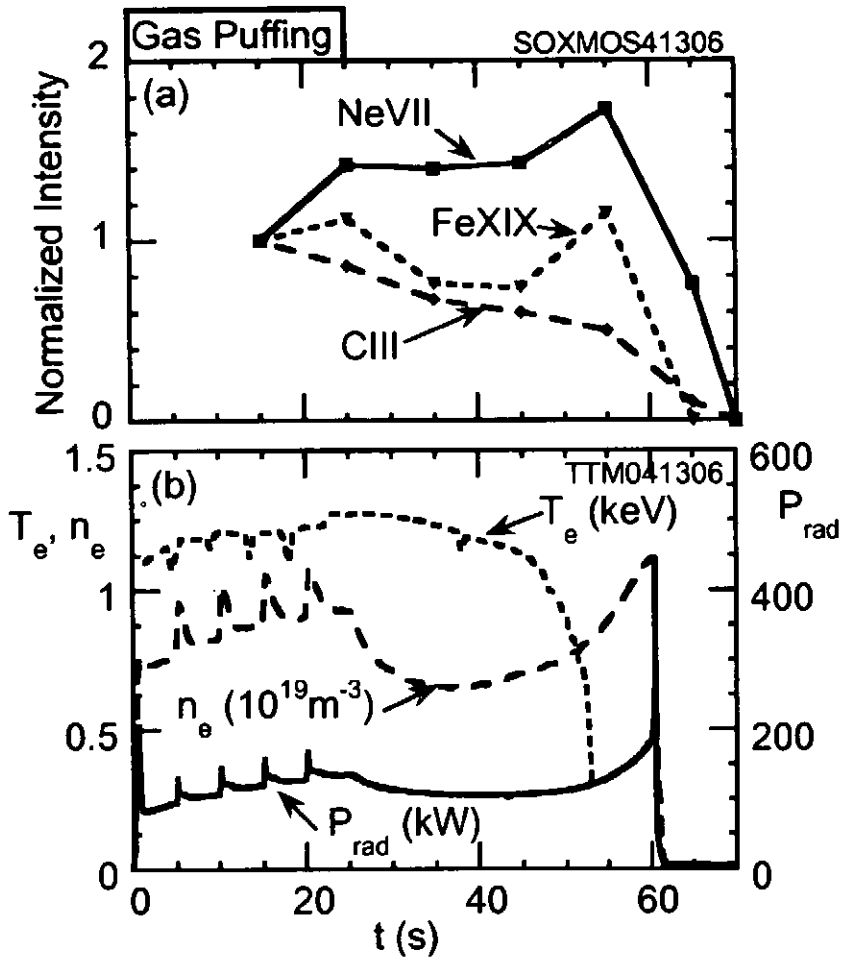

FIG. 6: (a) Time evolution of emission of impurity lines NeVII (*lambda* = 10.3 nm), FeXIX (*lambda* = 10.83 nm), CIII (*lambda* = 117.5 nm) measured by SOXMOS during the long pulse operation. The intensity of impurity lines is averaged for 10 sec, and is normalized at t=15 sec. (b) Time evolution ofthe electron temperature (T_e), the electron density (n_e), and the radiation power (P_{rad}).

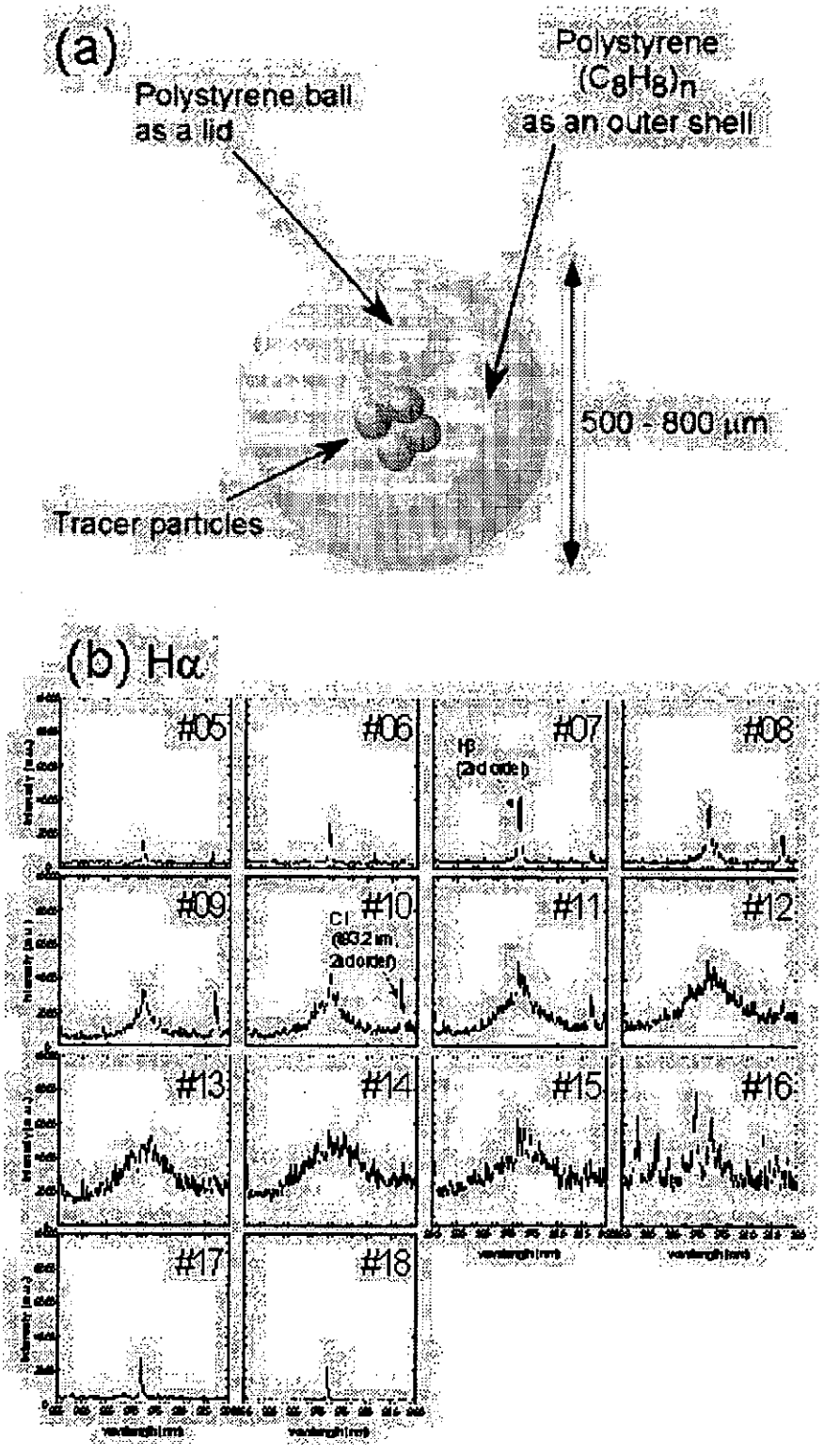

FIG. 7: (a) Schematic view of a TESPEL ball. (b) Time evolution of ablation light (dominantly H_β line).

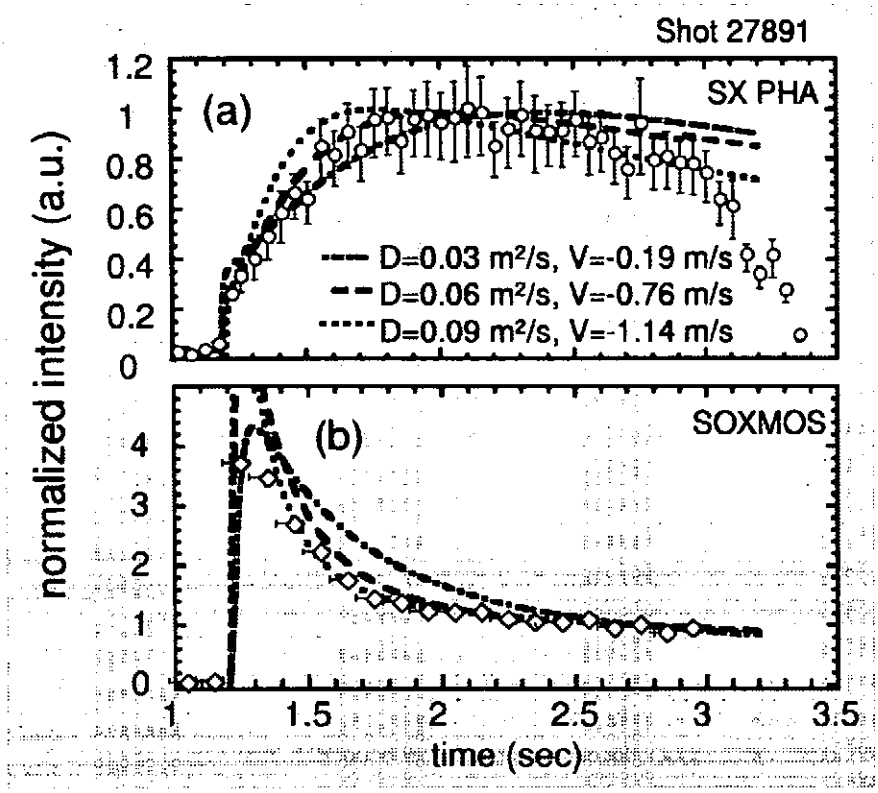

FIG. 8: (a) Evolution of Ti K_α (He-like; E = 4.7 keV) line emission measured by SX-PHA. (b) Evolution of Ti XIX (λ =16.959 nm) line emission measured by SOXMOS.

Fast spectroscopic measurements of the ablation clouds of Tracer-Encapsulated Solid Pellets injected into LHD plasmas

N. Tamura[1], V. Yu. Sergeev[3], D. Kalinina[2], S. Sudo[1], M. Goto[1], R. Ishizaki[1], A. Matsubara[1], K. Sato[1], S. Kato[1] and LHD experimental Group[1]

[1]*National Institute for Fusion Science,322-6 Oroshi-cho, Toki 509-5292, Japan*
[2]*Grad. Univ. Advanced Studies, 322-6 Oroshi-cho, Toki 509-5292, Japan*
[3]*State Polytechnical University, Politechnicheskaya 29, St.Petersburg 195251, Russia*

1. Introduction

In order to promote impurity particle transport studies, a tracer-encapsulated solid pellet (TESPEL) [1] has been developed [2]. TESPEL is a double-layered impurity pellet, which consists of polystyrene polymer (-CH (C_6H_5) CH_2-) as an outer shell (typically, 0.3-0.9 mm ϕ) and tracer particles as an inner core (typically, 0.2 mm size). TESPEL injection has been implemented for various important studies as well as for impurity transport study on the Large Helical Device (LHD) [3, 4]. For one thing, in order to investigate the behavior of fast ions, the active particle diagnostic referred to as the pellet charge exchange (PCX) diagnostic, which consists of a TESPEL injection and a natural diamond detector-based energy analyzer, has been utilized on LHD since the 2001 campaign [5]. The plasma ions neutralized by the charge exchange process in the TESPEL ablation cloud are measured with high time resolution. The time-resolved atomic energy spectra can be translated into a space-resolved measurement along the TESPEL trajectory. In this study, in order to estimate the space-resolved energy spectrum of plasma ions quantitatively, it is important to know the electron density, which changes with the TESPEL traveling across the plasma, in the TESPEL ablation cloud. In order to evaluate the electron density in the luminous cloud surrounding the TESPEL injected into the LHD plasma, measurements of Hydrogen Balmer beta line broadening are made, since the outer shell of TESPEL is made of polystyrene. In this paper, initial analysis results of the time-resolved spectra emitted from the TESPEL cloud will be described.

2. Experimental setup

The Large Helical Device (LHD) [6] is the world's largest heliotron device (l/m = 2/10) with a major radius of R_{ax} = 3.5 – 4.1 m, an average minor radius of 0.6 m and a toroidal magnetic field up to 3T. A TESPEL is injected from the outboard side of LHD by means of the pneumatic pipe-gun technique. In case of a titanium (Ti) tracer, several Ti micro-balls (with 80-100 μm diameter) have been filled inside the TESPEL. The total amount of Ti particle is varied approximately in the 0.5-3 x 10^{17} range. In order to obtain the characteristics of TESPEL deposited in the LHD plasmas, an optical fiber (800 μm core) with a collimator lens (19 mm diameter) is installed at the port adjacent to the injection port. The light emission from the ablating TESPEL is transmitted through the optical fiber to a spectrometer and photo-multiplier tubes (PMTs) with corresponding interference filters for shell and tracer. The spectra emitted from the TESPEL ablation cloud are measured with the Czerny-Turner

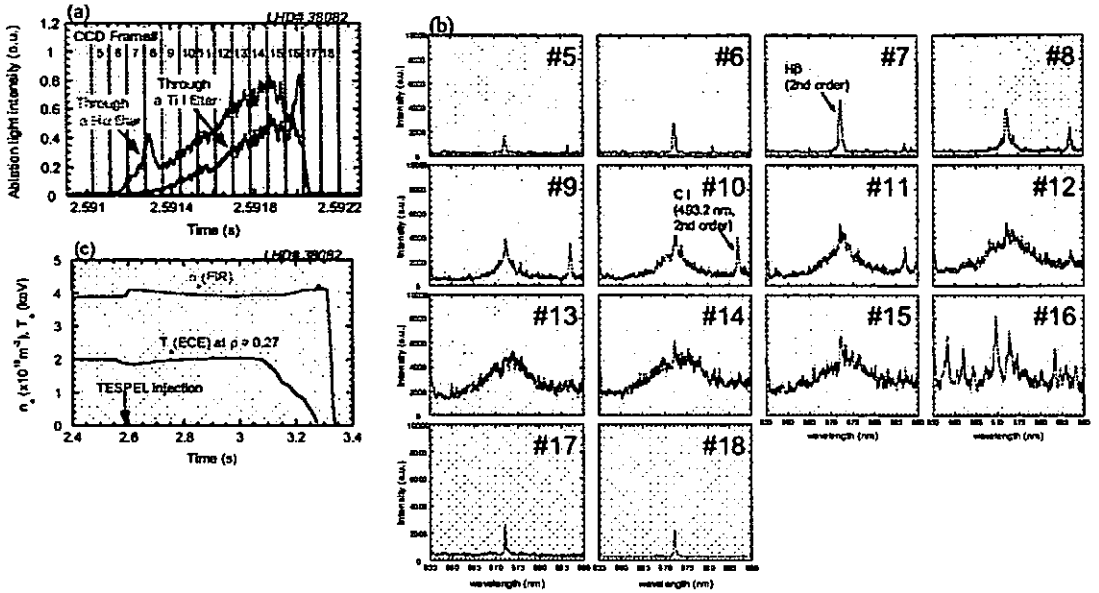

Figure 1. Typical spectral data of the light emission from the TESPEL ablation cloud measured with (a) the photo-multipliers and (b) the visible spectrometer and (c) the temporal behaviors of line-averaged electron density and temperature.

spectrometer (focal length of 250 mm, F/4.3) coupled with an intensified CCD, which operated in the fast kinetic mode. In order to efficiently measure the width of Balmer beta line (486.14 nm), the blazed wavelength of the grating with 1200 grooves/mm is set at 1 μm to measure the second order of the Balmer beta. The typical exposure time of this system is 84 μs. Therefore, the instrument can provide multiple spectra during a TESPEL event, since the typical time for the TESPEL ablation is ~ 1 ms.

3. Experimental results and Discussions

Figure 1 shows the typical spectral data of the light emission from the TESPEL cloud measured with the PMTs and the visible spectrometer and the temporal behavior of line-averaged electron density and temperature. In this case, the TESPEL, whose diameter is 0.73 mm, has a Ti tracer. As seen in Fig. 1(b), the line broadening of the hydrogen Balmer beta is clearly measured with the spectrometer. The line emission seen on the right side of the Balmer beta in the spectrum is identified as the second order of C I (493.20 nm). At the CCD frame number of 16, the spectrum with the line emissions from the Ti tracer ablation cloud, which can be distinguished from the shell ablation of TESPEL, are also measured. As seen from Fig. 2, the spectrum of titanium line emissions observed in a low electron temperature plasma, which interacts with a titanium end plate on a linear device named TPD, is rather different from that observed in the tracer ablation

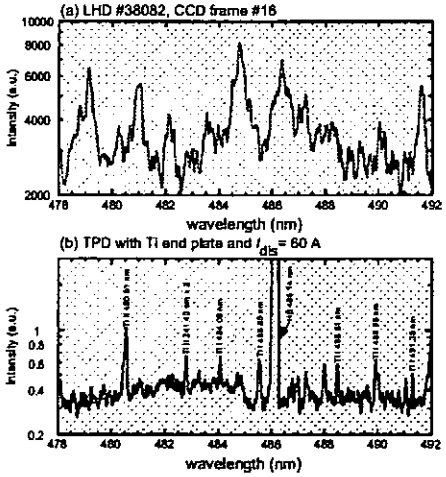

Figure 2. Comparison of the spectrum measured during the ablation of titanium tracer with that in a low electron temperature plasma (performed on a linear device named TPD with a titanium end plate).

cloud in the LHD plasma. This discrepancy may be attributed to the difference of the electron temperature, which gives the different atomic process.

The electron density in the TESPEL cloud is evaluated from the FWHM of a Lorentzian curve fitted to the measured Balmer beta line profile, together with the following relationship: $n_e = \sqrt[1.04]{(2.38\times10^{21})(\Delta\lambda)^{3/2}}$, which is derived from the Griem's table [7]. In this relationship, any temperature effect is ignored. The instrument function of this spectrometer is taken into account in determining the line width. In LHD #36912, at the time when the integrated Balmer beta line intensity reaches a maximum value, the FWHM of Balmer beta line profile is 1.19 nm, that is, the electron density in the TESPEL ablation cloud is evaluated as 1.3 x 10^{22} m^{-3}. As seen in Fig. 3(a), the theoretical Lorentzian profile fits the measured Balmer beta line profile well at that time. The electron density in the tracer ablation cloud is also to be measured in TESPEL PCX diagnostics. This can be done with comparative ease when the line emissions from the tracer ablation cloud do not lie in the same spectral domain as the Balmer beta. Since it is already confirmed that the line emissions from carbon (a component of TESPEL) have almost no influence on the Balmer beta line profile, the estimation of the electron density in the ablation cloud of the carbon tracer is tried. As seen from Fig. 3(b) and (c), there is a difference in the temporal behavior of the deduced electron density between the cases with and without the carbon tracer during the last half of the TESPEL ablation. The different behavior of the deduced electron density in the cloud between the two cases can be explained by the contribution of the carbon tracer. Therefore, the electron density in the tracer ablation cloud is estimated successfully with the carbon tracer and the local deposition of the tracer is demonstrated again with the behavior of electron density in the TESPEL cloud. Here, Let us discuss the question of whether the estimated electron density from the line broadening observed in the pellet cloud reflects the maximum electron density in that region or not. In order to simplify the problem, the hydrogen ice pellet case is considered. Figure 4 shows the radial profiles of atomic density, ion density and temperature, which are simulated using the CIP method [8] in the region surrounding the hydrogen ice pellet injected into the plasma, and reconstructed Balmer beta line profiles. As seen in Fig. 4(b), the fully integrated Balmer beta line profile, which is to be measured, is similar to the Balmer beta line profile, which is a spatial integration over the region with the maximum line intensity, not to that integrated over the region with

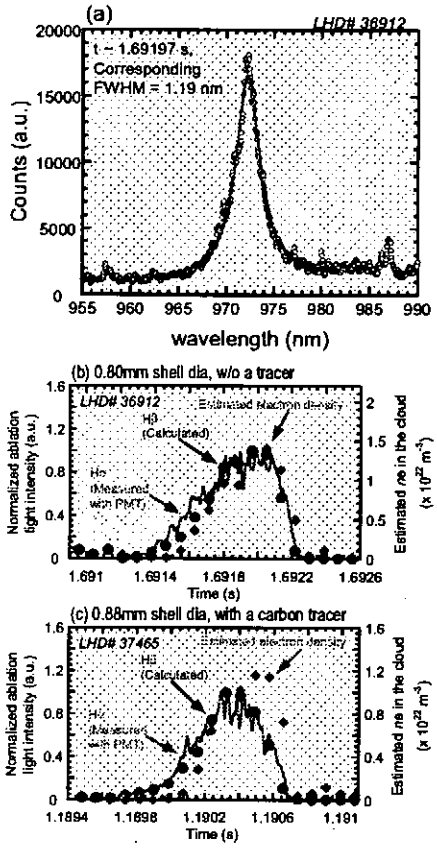

Figure 3. (a) Measured Balmer beta line profile with the fitted Lorentzian profile at t = 1.169197 s in LHD #36912. Temporal evolutions of the estimated electron density (blue closed circle) and the Balmer beta line intensity (purple closed diamond) calculated from the fitted Lorentzian curve, together with the Balmer alpha line emission (red solid line) measured with the PMT in the case of (b) the TESPEL without a tracer and (c) that with a carbon tracer.

the maximum electron density. This result indicates that the measured width of the line broadening in the pellet cloud does not always reflect the maximum electron density in that region. In LHD, in order to obtain accurate information about electron density in the TESPEL cloud, the space-resolved line broadening measurement is under development.

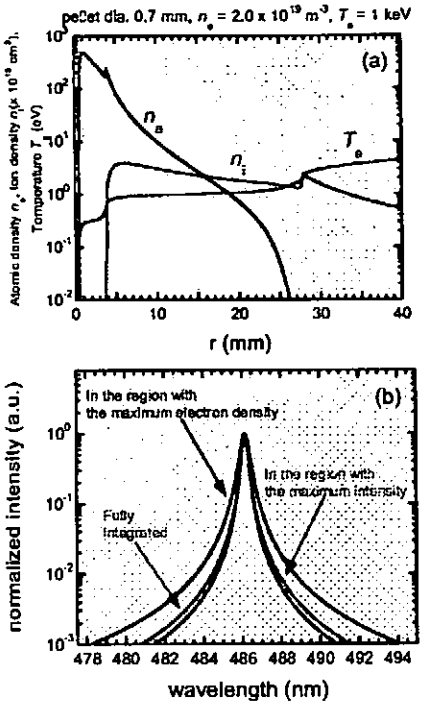

Figure 4. (a) Radial profiles of atomic density, ion density and temperature, which are simulated using the CIP method in the region surrounding the hydrogen ice pellet injected into the plasma. (b) Balmer beta line profiles reconstructed by the spatially integrated Lorentzian profile with the corresponding FWHM and intensity. (red line: Fully integrated, blue line: in the region with the maximum electron density, green line: in the region with the maximum intensity). The intensity is normalized by the peak value.

4. Conclusions

The highly time-resolved spectra of light emissions from the TESPEL ablation cloud were measured with a spectrometer coupled with an intensified CCD, which operated in the fast kinetic mode. The electron density in the luminous cloud surrounding the TESPEL injected into the LHD plasma was evaluated from the measurement of Hydrogen Balmer beta line broadening. In LHD #36912, the electron density in the ablation cloud of TESPEL, which has a diameter of 0.8 mm and no tracer, increased up to 1.3 x 10^{22} m^{-3}. The electron density in the tracer ablation cloud was also estimated successfully with the carbon tracer. The question of whether the deduced electron density from the line broadening observed in the ablation cloud reflects the maximum electron density in that region or not is discussed with the hydrogen ice pellet case. The result derived from the discussion indicates that the measured width of the line broadening in the pellet cloud does not always show the maximum electron density in that region.

Acknowledgments

This work is partly supported by Grant-in-Aid for Scientific Research (B) No. 10480109 and No. 15340201, grant No. L00537 of JSPS and JSPS Research Fellowships for Young Scientists. The authors would like to thank Professor O. Motojima, Director of NIFS, for his continuous encouragement of this work and all of the technical staffs of NIFS for their support.

References

[1] Sudo S 1993 *J. Plasma Fusion Res.* **69**, 1349. [2] Khlopenkov K *et al* 1998 *Rev. Sci. Instrum.* **69**, 3194. [3] Sudo S *et al* 2002 *Plasma Phys. Control. Fusion* **44**, 129. [4] Tamura N *et al* 2003 *Plasma Phys. Control. Fusion* **45**, 27, [5] Goncharov P *et al* 2003 *Rev. Sci. Instrum.* **74**, 1869. [6] Motojima O *et al* 1999 *Phys. Plasmas* **6**, 1843. [7] Griem H R 1974 "*Spectral line broadening by Plasma*", Academic press, New York. [8] Ishizaki R *et al* 2003 *J. Nucl. Mater.* **313-316**, 579.

Two Dimensional Diagnostic of Edge Plasma Structure using a Lithium Beam Probe in CHS

K. Nakamura[1], H. Iguchi[2], M. Ueda[3], T. Morisaki[2], M. Isobe[2], C. Takahashi[2], S. Nishimura[2], C. Suzuki[2], Y. Yoshimura[2], .A. Shimizu[2], S. Nagaoka[2], T. Minami[2], K. Ida[2], S. Okamura[2], K. Matsuoka[2]

[1] *The Graduate University for Advanced Studies, Toki 509-5292, Japan*

[2] *National Institute for Fusion Science, Toki 509-5292, Japan*

[3] *National Institute for Space Research, Sao Jose dos Campos, SP, Brazil*

Abstract

A neutral lithium beam probe (LiBP) for two-dimensional diagnostic of edge plasmas has been designed and installed on the Compact Helical System (CHS). The beam injection angle can be varied and the beam can cover the edge and separatrix region of helical diverter configuration. Two-dimensional emission profiles are obtained near and outside of the last closed flux surface (LCFS) for ECH and NBI heated plasmas, suggesting new knowledge on the edge plasma structures in the heliotorn type helical device.

1. Introduction

Diagnostics of edge plasma parameters are important because plasma properties in the region have key role to determine the global plasma confinement. Understanding and controlling edge plasmas are also important for the divertor design in fusion reactors. In order to study plasma structure in the area, two-dimensional measurements are essential.

A lithium beam probe (LiBP) is one of the best techniques for the measurement of edge plasma density profile. This method, which utilizes the emission of the LiI resonance line (2S-2P, 670.8 nm) from the injected neutral lithium by electron impact excitation, was first developed by Kadota et al.[1]. The LiBP can probe plasmas from the edge to the core crossing the last closed flux surface (LCFS) without perturbation or contamination to the plasma. It has been used in many magnetic confinement devices such as NBT-1M, ASDEX, TEXTOR, CHS, WVII-AS, JET, and more recently LHD. But all those measurements are in one dimensional along the fixed beam line.

A new LiBP system that can measure two-dimensional plasma structure in the edge region including the separatrix has been designed and installed on CHS. The system has a beam injector with variable injection angle and a multi-channel optical detection system. Changing the beam injection angle shot by shot, two-dimensional beam emission profile is obtained. When the target plasma density is low, in which beam attenuation is negligible, the electron density is simply proportional to the beam emission intensity Two-dimensional density profiles are directly obtained. But for higher density case, where beam attenuation

becomes significant, the density profile reconstruction from the emission intensity profile taking the attenuation effect into account is necessary. Details on the density reconstruction algorithm are found elsewhere[2].

2. 2D-LiBP system on CHS

The CHS is a l=2/m=8 heliotron type helical device with a major radius of 1.0 m and average minor radius of 0.2 m. The 2D-LiBP system has been installed on the CHS as shown in Figure 1. The beam injector is located on the upside of the torus, which consists of an ion gun with a thermoionic emission type Li source, a Pierce extractor and a cylindrical lens. The beam energy is in the range from 10 to 20 keV with an equivalent neutral beam current of about 0.1 mA. The ion beam is neutralized in the Cs neutralizing cell operated at the temperature about 180 °C. The beam energy is selected so that it offers both adequate spatial resolution and beam penetration. The spatial resolution is basically determined by the lifetime of the excited state of Li atom (~27 ns). For the 15 keV beam the spatial resolution is about 1 cm and beam penetration depth is expected to be about 10^{18} m^{-2} of line-integrated density. The neutral beam diameter is about 20 mm in the CHS vacuum chamber.

Light collection optics, which detects the emission from the LiI resonance line, is located on the side port of the torus. The optical system consists of a light collection lens, optical fibers, optical interference filters and Avalanche Photodiode (APD) detectors. Since the angle between beam line and sight line is not at right angle, the observed spectral line suffers Doppler shift. Maximum Doppler shift at beam energy of 15 keV is 0.9 nm. So the optical interference filters are selected with the bandwidth of 2.0 nm. Its peak transmission is about 65 %. Twenty-five couplers for optical fibers are prepared on the light collection lens corresponding to twenty-five observation points along the beam with about 8 mm spacing. Eight channel optical fibers can select eight observation points by choosing eight couplers among those.

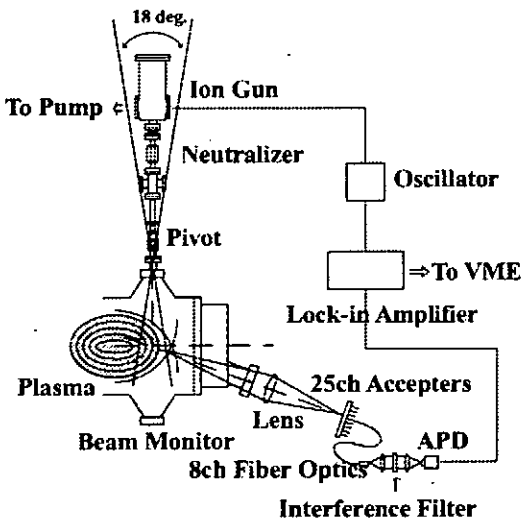

Fig. 1. Experimental setup for 2D-LiBP system on CHS.

The injection beam line angle can be varied between +18° and -18° in the major radius direction. Two-dimensional profile is obtained by changing the beam injection angle shot by shot. Figure 2 shows the map of the observation area. Shaded area indicates the possible sample volume location determined by the twenty-five optical couplers.

Since the signal to noise ratio for the present beam intensity is less than unity (S/N < 1), signals from APD detectors are introduced to phase sensitive detectors with 4 kHz beam modulation. Typical time resolution is 3-10 ms in the present measurements.

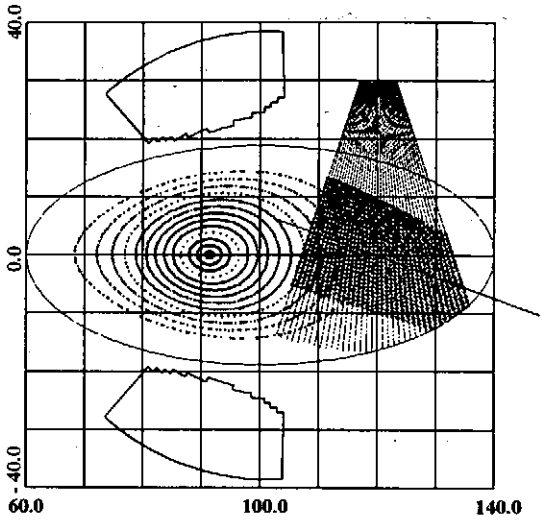

Fig. 2. Observation grid map. Shaded area indicates the possible sample volume location determined by the twenty-five optical couplers.

3. Experimental Result

Experiments have been carried out with the magnetic axis at R_{ax}=0.921 m, which is the inboard limiter configuration. The LCFS is touching the inboard vacuum chamber wall at 8 positions. The magnetic field strength is 0.95T on the axis.

Hydrogen plasmas are produced by electron cyclotron resonance (ECR) heating with a 53.2 GHz, 170 kW gyrotron and additionally heated by two neutral beam injectors (both in co-direction) with beam energy of 40 keV and total power of 1.3 MW. ECH is applied from t = 20 ms to 120 ms and NBI from t = 80 ms to 180 ms where t = 0 is the start of data acquisition for diagnostics. Average electron density in ECH phase is about $1\times10^{19}\,m^{-3}$ and in NBI phase is $4\times10^{19}\,m^{-3}$ respectively.

The Li beam injection angle is varied every 2° between 0 ° and -18° in the present experiments. Figure 3 shows an example of the light emission signal. Signal from a killer puff, which is introduced to prevent high-energy electron production during the turn off phase of the helical coils, is also detected at around t = 450 ms. Expanded signal at this phase is shown in the same figure. The emission signal comes from the collision of Li beam with neutral gas. Since the gas distribution becomes uniform in a short time, relative sensitivity between channels can be calibrated.

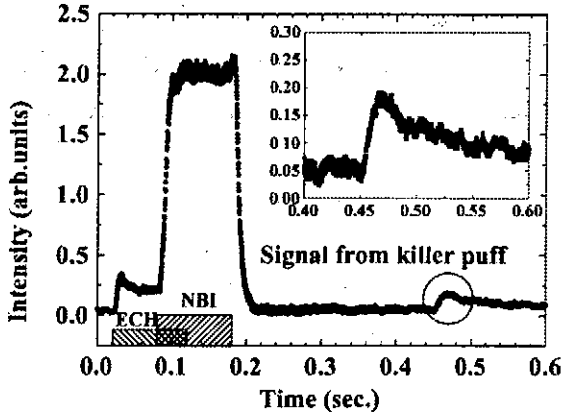

Fig. 3. An example of the light emission signal.

Two-dimensional beam emission profiles are shown for ECH phase (Fig. 4a) and NBI phase (Fig. 4b).

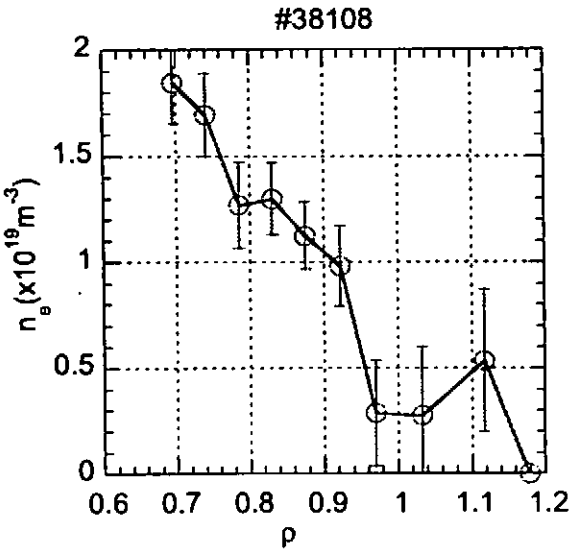

Fig.2 Plasma density profile from CO_2 - YAG two color interferometer. Error bars correspond to uncompensated vibrations.

detectors of two interferometers can be precisely matched. For CO_2 interferometer information from 32 chords with 8mm spacing for 250 mm total width of slab beam was recorded by photoconductor array. YAG interferometer operates using three avalanche photo diodes and 70 mm between chords. Structure of vibrations inside probe beam cross section is not uniform and phase shift for the different chords of CO_2 laser interferometer was interpolated from the second color interferometer data. Fig.1 shows the total phase shift recorded by CO_2 laser interferometer (1), YAG interferometer phase shift (2) and the compensated signal (3) for plasma with pellet injection. Second color correction reduces vibration phase shift by factor of 3 so remaining uncompensated component corresponds to linear integrated electron density of $2 \cdot 10^{18}$ m^{-2}. Plasma density profile for shot #38108 is plotted on Fig.2. Subtraction of vibrations allows to calculate density profile by Abel inversion procedure for shots with comparatively small plasma density about $n_e \approx 1\text{-}2 \cdot 10^{19}$ m^{-3}. However, because YAG laser radiation does not completely cover the CO_2 beam cross-section, residual uncompensated components is not small enough to permit accurate determination of the profile data near the plasma edge.

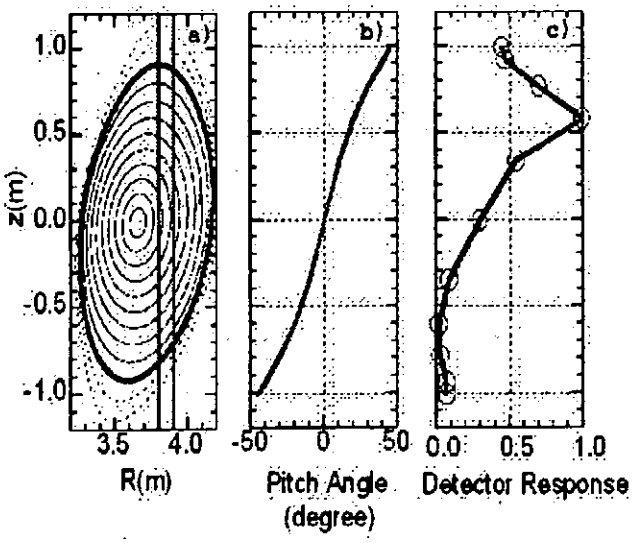

Fig. 3 Shear technique sensitivity.
a) – LHD plasma cross section;
b) – pitch angle of magnetic field;
c) – measured sensitivity.

The flexible arrangement of optics of CO_2 laser interferometer allows operation in both heterodyne interferometer (HI) mode for the profile measurements and in phase contrast interferometer (PCI) mode for observation of density fluctuations [2]. In PCI the phase modulation pattern produced by fluctuations is converted

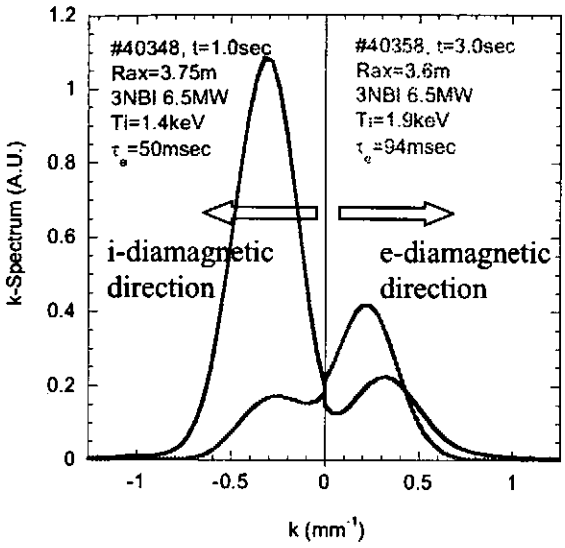

Fig. 4 Spatial spectrum of fluctuations for two plasma shots.

to the intensity variations and imaged to the detector array. Since standard PCI lacks for the spatial resolution along the beam axis, several approached was used to get the longitudinal resolution. One of them employs strong magnetic shear on LHD to obtain modest spatial resolution [3]. Fig.3a shows position of the interferometer probe Gaussian beam (red) with 100 mm ($1/e^2$ intensity) width in the cross section of LHD plasma. As one can see from Fig.3b the angle between the magnetic field direction at the plasma top and plasma bottom is almost 90°. The imaging optics was designed to record fluctuations with 2.5 mm sampling by one dimensional 32 channel linear detector array. The parallel to the magnetic field component of the wave vector of fluctuations is expected to be much smaller than perpendicular one and smaller than cut off wavenumber of PCI technique (which is about 2π divided by laser beam width). Therefore if detector is oriented normally to the magnetic field lines at the plasma top, projection of wave vectors of fluctuations located at plasma bottom is small. So signals form bottom fluctuations can not be detected. Sensitivity of the diagnostics was measured by recording the signal produced by the 10 kHz sound wave injected at different angles in air. Dependence of sensitivity on the longitudinal coordinate is presented at Fig. 3c. In this series of experiments the beam was tilted and detector axis was set transversely to the magnetic field line at $z = 0.6$ m. Fig. 4 shows an example of obtained spatial spectra of fluctuations. Two discharges with different magnetic configurations (magnetic axis positions $R_{ax} = 3.6$ with better characteristics of neoclassical confinement and 3.75 m which is optimized for interchange instability) and with the same plasma density are presented. Bigger signal was observed in the shot when plasma confinement was worse. With obtained spatial resolution of about a minor radius different poloidal propagation direction of fluctuations was detected. If fluctuation propagation is dominated by plasma rotation, obtained difference in poloidal propagation (electron diamagnetic directed at $R_{ax} = 3.6$ m and ion diamagnetic directed at $R_{ax} = 3.75$ m) agrees with theoretical predictions for parameters of this experiment [4].

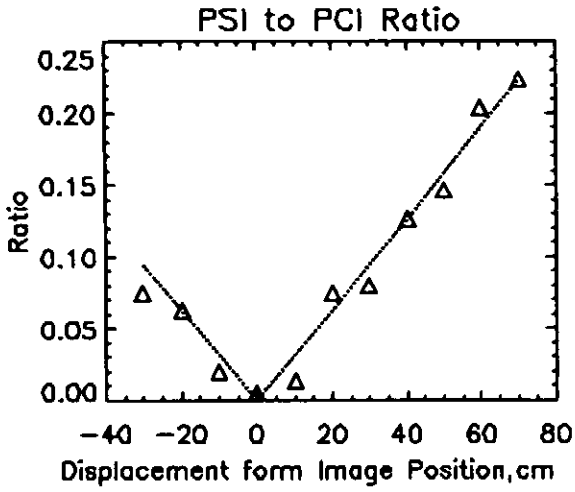

Fig. 5 Ratio of amplitude (PSI) and phase (PCI) signals for bench-top experiment. Theoretical dependence is plotted by dashed line.

New imaging scheme for the localized fluctuation study was also tested during last experimental campaign. Simultaneous record of phase and amplitude variations of radiation passed trough the plasma fluctuations makes possible axial localization of fluctuations from the ratio of two signals [5]. This technique, however, needs good SNR, therefore, we tried to increase contrast of the phase image. This can be done by reduction of non scattered components of probe radiation relative to scattered on plasma fluctuations components with the use of spatial filter placed in the Fourier plane of the detection optical system. The bench-top experiment was performed to determine the best spatial resolution, which can be achieved. This test experiment was done using two separate detectors to measure the phase and amplitude signals in the layout close to the real experiment geometry. Ultrasonic wave (US) in air with wavelength 1 cm and total phase shift of about $3 \cdot 10^{-4}$ radians was used as test object. The optical gain up to 5 was used during this test experiment. At Fig.5 the ratio of amplitude to phase signals versus the displacement of US from imaging plane along the CO_2 laser beam direction is plotted. Axial spatial resolution is limited by spread of data points form theoretical dependence and is better than 10 cm for fluctuations with 1 cm wavelength. First experiments for observation of fluctuations with two detector scheme was performed on LHD. Due to small amount of obtained data these results can be regarded as preliminary and new experiments are necessary to gain a better understanding of spatial distribution of microturbulence.

ACKNOWLEDGEMENTS

This work was supported by a Grant-in-Aid for JSPS Fellows from the Japanese Ministry of Education, Culture, sport, Science and Technology.

REFERENCES

1. T. Akiyama et al, RSI, **74**, 1638 (2003).
2. K. Tanaka et al, RSI, **74**, 1633 (2003).
3. S. Kado et al, Jpn. J. Appl. Phys., Part 1 **34**, 6492 (1995).
4. M. Yokoyama et al, Nucl.Fusion, **42**, 143 (2002).
5. L.N. Vyacheslavov at al, 29th EPS Conference on Plasma Physics and Controlled Fusion, Mountrex, 17-21 June 2002 ECA **26B**, P-5.105 (2002).

Effect of Magnetic Field on Asymmetric Radiative Collapse in the Large Helical Device

N. Ashikawa[1], B.J. Peterson[1] and the LHD Experiment Group[1]

[1]*National Institute for Fusion Science, Toki, Japan*

1.Introduction

The Large Helical Device (LHD) [1] is a large-scale superconducting heliotron system with a set of l/m =2/10 helical coils. Since the first experimental campaign in 1998 it has been operated with R/a=3.6~3.9/0.6 m, B_t=1.5~2.9 T. Electron cyclotron heating (ECH) is used for the plasma production and two or three negative-ion-based neutral beam injectors (NBI) are used to heat the plasma. In LHD, the localized high radiation region during radiative collapse was measured [2, 3] and this phenomenon is shown to be similar to the multifaceted asymmetric radiation from the edge (MARFE) [4] with regard to its position on the inboard side of the torus. Several diagnostics have measured the poloidal asymmetry of this phenomenon in LHD. In particular, infrared imaging video bolometer (IRVB)s have measured the two-dimensional plasma radiation brightness profiles and these results show that the localized radiation appeared at the lower side of the midplane [5].

2. Set up of IR Bolometer systems on LHD

For the diagnosis of the total plasma radiation, several bolometry systems are used [6]. Resistive bolometers are the main diagnostics for measuring the plasma radiation in LHD and infrared (IR) imaging bolometers and Absolute eXtreme UltraViolet (AXUV) diode detectors also are used.

The IR imaging bolometer is a two-dimensional diagnostic system for measuring the plasma radiation. The plasma radiation is absorbed by a metal foil in the vacuum vessel and the resulting temperature rise on the foil is measured by an IR camera from outside the vacuum vessel. For the metal foil, gold of 1 μm thickness is used and this foil was sandwiched by two identical copper mask frames. In particular, the type using a large foil area facing the plasma is

called the InfraRed imaging Video Bolometer (IRVB) [7]. Three IRVBs were installed in LHD for the LHD 6th campaign (2002-2003). For the vertical elongated plasma cross-section, one observed the plasma tangentially and the other from an upper port. For the horizontal elongated plasma cross-section, one observed from an outside port. Figure 1 shows the field view on the midplane of three IRVBs on LHD.

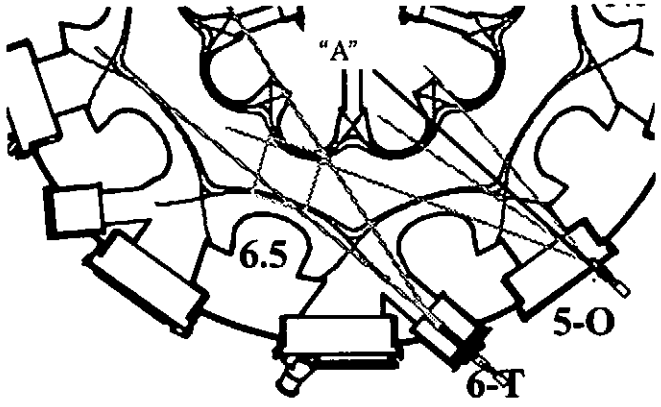

Figure 1 Each field of view on the midplane of three IRVBs on LHD

3. Effect of Magnetic Field on Asymmetric Radiative Collapse

In the 6th LHD campaign (2002-2003), radiative collapse of the LHD plasma was measured with a reversed magnetic field. Figure 2 shows a CAD drawing of the field of view (FOV) of the IRVB from the outside port on LHD. Shadow areas show the last closed magnetic surface and an orange line is a center of plasma. In this figure, the plane at line "A" passes through the horizontally elongated plasma cross-section as shown in Fig.1. If we assume the plasma radiation with a hollow profile, the high radiation loss is observed typically from the ergodic region of the plasma that is outside the last closed magnetic surface. In Fig.2, ergodic regions are seen in area "B" on the vertically elongated cross-section and "C" in the near edge region of the plasma on the horizontally elongated cross-section.

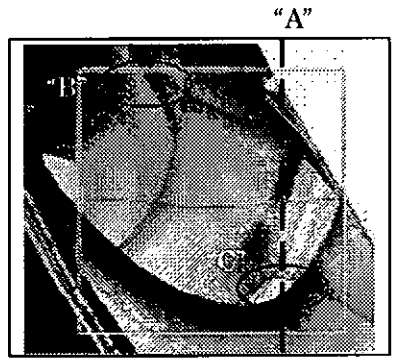

Figure 2 CAD drawing of field of view (FOV) of IRVB from outside port on LHD.

Figure 3 shows an IRVB image from an outside port for LHD shot #39631 with normal magnetic field direction and Fig. 4 shows LHD shot #40352 which has a reversed magnetic field, both during the radiation collapse, with the same magnetic axis of 3.75 m.

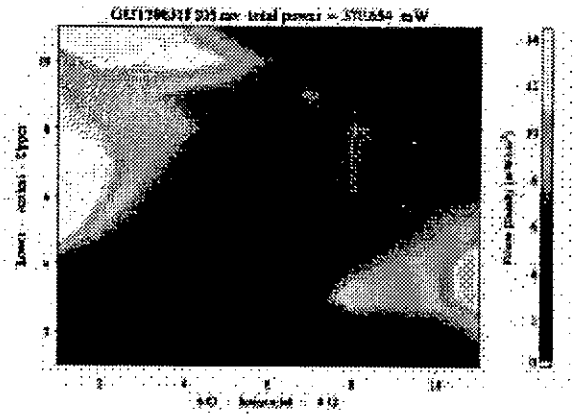

Figure 3 IRVB image from an outside port for LHD shot #39631.

From both discharges, at the left side channels with long lines of sight show the high radiation region. These structures are estimated to be localized radiation regions, since other IRVB data from the upper port at the same timing also observed localized radiation at the inboard side. The high radiation region for LHD shot #39631 in Fig. 3 at left side is wider than that of the reversed magnetic field discharge in Fig. 4. These channels of the outside port IRVB have a tangential FOV, therefore data have to be checked to differentiate the radiation loss and the NBI shine-through power. As channels on area "C" in Fig.2 show brightness radiation only during the discharge, these data are used as a reference.

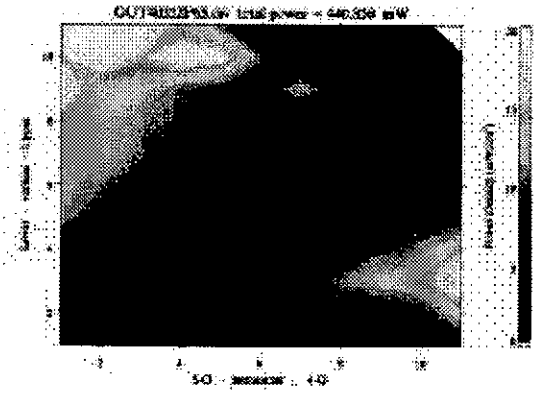

Figure 4 IRVB image of reversed magnetic field from an outside port for LHD shot #40352.

For the question of the high radiation region structure at the horizontally elongated cross-section, these data give a clue. Since the channels on the horizontally elongated cross-section on this FOV don't show high radiation losses at this frame, this indicates that the radiation at the horizontally elongated cross-section may not have a highly localized region of radiation.

4. Discussion and summary

In the tokamaks, the position of the MARFE was clearly observed to change depending on the direction of the magnetic field. In LHD, the position of the main source of the localized radiation during the collapse remained the same as in the 5th LHD campaign (2001-2002). But it was estimated that the width of the high radiation region was changing for different magnetic axis positions and magnetic field polarities.

Using data with a new FOV of IRVB, more details of radiation structure could be observed in LHD.

Acknowledgment

One of the authors (N. A.) work was supported by the Sumitomo Foundation.

References

[1] O. Motojima *et al., Phys. Plasmas* **6** (1999) 1021.

[2] B.J. Peterson, Yuhong Xu *et al., Phys. Plasmas* **8** (2001) 3861.

[3] Yuhong Xu, B.J. Peterson *et al., Nucl. Fusion* **42** (2002) 601.

[4] M.Z. Tokar, *Phys. Plasmas* **6** (2001) 2866.

[5] N. Ashikawa, B.J. Peterson et al., *J. Nucl. Mater.* 313-316C (2003) 1103.

[6] B.J. Peterson *et al., Plasma phys. Control Fusion* **45** (2003) 1167.

[7] B.J. Peterson *et al., Rev. Sci. Instrum.* **74** (2003) 2040.

Achievement of a High Ion Temperature with Ne- and Ar-Seeded Discharges by High-Power NBI Heating in LHD

Y. Takeiri, S. Morita, J. Miyazawa, K. Tsumori, K. Ikeda, Y. Oka, M. Osakabe, K. Nagaoka, O. Kaneko, S. Masuzaki, M. Goto, T. Mutoh, A. Komori, and LHD Experimental Group

National Institute for Fusion Science, Toki, Gifu 509-5292, Japan

1. Introduction

The Large Helical Device (LHD) is the world-largest superconducting helical system, and equipped with a negative-ion-based neutral beam injection (NBI) system, which consists of three tangential injectors [1]. The injection energy of hydrogen is as high as 150 – 180 keV, which is appropriate for relatively high-density plasmas of $(3–4)\times10^{19}m^{-3}$, aiming at high $n\tau T$ plasmas. However, the negative-NBI is not necessarily proper to raise the ion temperature in low-density plasmas as it is, because most of the ionized beam power goes to electrons due to the high-injection energy, and, moreover, a large part of the injected beam passes through the plasma without ionization in low-density hydrogen plasmas. As a result, the achieved ion temperature has been less than 2.5 keV in such a hydrogen discharge. There are two scenarios to increase the ion temperature in the LHD. One is to improve the ion transport by achievement of the neoclassical electron root generating a strong positive electric field. Although the electron root has been achieved with a centrally focused ECH (electron cyclotron resonance heating) [2], unfortunately, an increase in the ion temperature has not been observed yet. The other is to increase in direct ion heating power by producing high-Z plasmas. We already confirmed the increase in the ion temperature in high-Z plasmas with neon-seeded discharges in the 2001 experimental campaign [2,3]. In the previous (2002) campaign, the glow discharge cleaning with neon gas was applied to the wall conditioning and the argon gas was puffed to the target plasma to achieve higher-Z plasmas with a lower density. As a result, the ion temperature was further increased and reached 7 keV. In the following, the plasma characteristics of the low-density and high-Z discharges are presented with a view of the ion temperature.

2. Negative-Ion-Based NBI System

The LHD-NBI system consists of three tangential injectors, each of which has two large negative-ion sources [4]. One injector has the opposite injection direction to the other two injectors. The specified injection energy is 180 keV and the beam species is hydrogen. The injection power has gradually increased year by year since the NBI system was operational in 1998, and reached 10.3 MW in the previous campaign. High-power neutral beams are injected usually for 2 sec with high reliability. The shine-through beam, passing through the plasma without ionization, is incident on the beam-facing armor tiles installed inside the LHD vacuum vessel. The shine-through power is estimated with a calorimeter

array on the armor tiles, and the port-through injection power is determined with the shine-through power measurement [5].

3. High-Z Discharges with Low Densities

In the high-Z plasmas, the ionization rate of the injected neutral beam is higher and, therefore, the plasma absorption power is increased, especially in low densities. Figure 1 shows the ratio of the plasma absorption power to the port-through power of the injected neutral beams as a function of the line-averaged density. The beam absorption rate is fitted to $1-\exp(-\sigma_{eff} n_e \ell)$, using the line-density $n_e \ell$, and, then, σ_{eff} represents the effective cross-section for the beam ionization. As shown in Fig. 1, the plasma absorption power is enhanced in the Ne- and Ar-seeded plasmas compared with the H_2-puffed one, and the effective cross-section for the beam ionization is about 2 times larger. In low-electron density plasmas below $0.5\times10^{19}m^{-3}$ the plasma absorption power is increased 1.6 times. Since the ion number density is reduced compared with the electron number density in the high-Z plasmas, the direct ion heating power is much enhanced. Consequently, with the high-Z discharges, the ion heating power by the high-energy NBI can be increased even in the low-density plasmas. In other words, the high-energy NBI heating in the high-Z plasmas is equivalent to the low-energy NBI heating in hydrogen discharges where the ion heating is dominant, although the plasma characteristics such as the collisionality are not the same.

The high-Z plasma is diluted with the wall-absorbed hydrogen during the discharge, and a degree of the dilution is large in the low-density plasmas. To realize the low-density and high-Z plasmas, a glow discharge cleaning was intensively performed with neon gas for reduction of the wall-absorbed hydrogen. Successive three nights of Ne-glow discharge cleaning led to a gradual reduction of the wall-absorbed hydrogen. The H_2 partial pressures before the start of the main discharges (after the Ne-glow discharge cleaning) are shown in

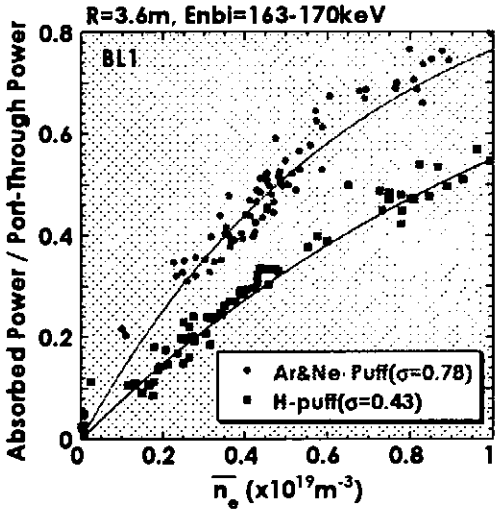

Fig. 1 Ratio of the plasma absorption power to the port-through NBI power as a function of the density.

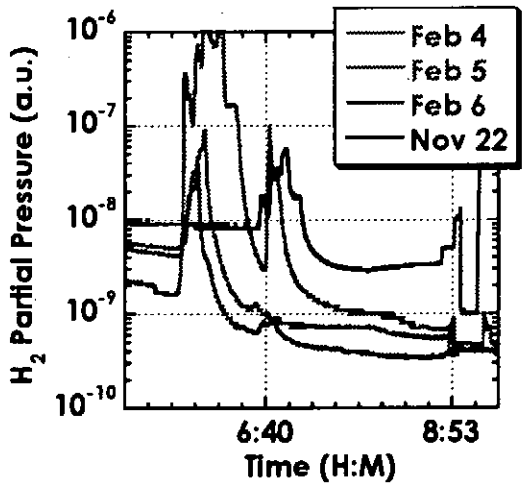

Fig. 2 H_2 partial pressures before the start of the main discharges (after the neon glow discharge cleaning).

Fig. 2, for the first, the second and the third days of the successive high-Z plasma experiments (Feb. 4–6). The Ne-glow discharge cleaning was continued for about 8 hours at a night. In the figure, the H_2 partial pressure in the case of the 2 hours of the Ne-glow discharge cleaning (Nov. 22) is also indicated for comparison. The H_2 partial pressure is reduced day by day, indicating the effectiveness of the Ne-glow discharge cleaning for the reduction of the residual hydrogen.

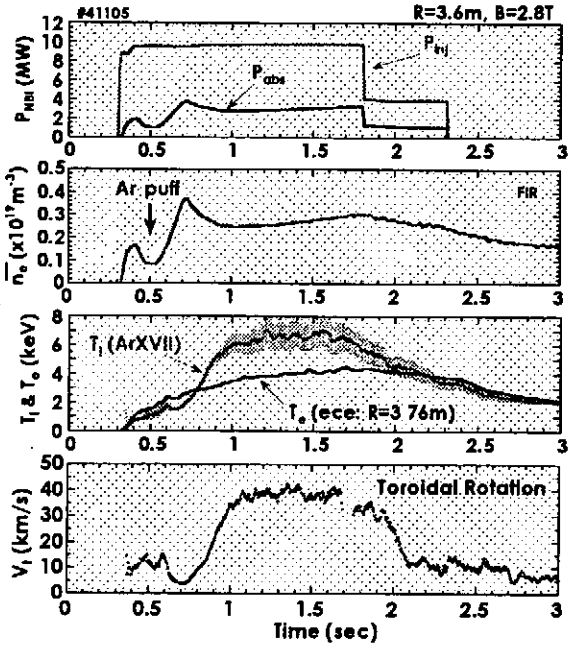

Fig. 3 Time evolution of the various plasma parameters in an Ar-puffed plasma. The central ion temperature is measured with the Doppler broadening of Ar XVII.

4. High-Ion Temperature with Neon- and Argon-seeded Discharges

To realize the high-Z discharges with low-densities, neon and argon gases were puffed in low-density plasmas. Figure 3 shows the time evolution of the various plasma parameters in an Ar-puffed plasma. The central ion temperature, measured with the Doppler broadening of an X-ray line of ArXVII, is much increased after the Ar gas puff and reaches 7 keV with an injection power of 9.8 MW at an electron density of 0.3×10^{19} m^{-3}. The electron temperature, measured with ECE, is also increased up to 4.3 keV, and, however, is much lower than the ion temperature. The toroidal rotation is correlated with the increase in the ion temperature, and the toroidal rotation velocity reaches 40 km/s, which is about 30 % of the Ar-thermal velocity. The ion temperature is dependent on the amount of the Ar gas puff, as shown in Fig. 4. It is increased with an increase in the Ar gas puff, and excessive amount of the Ar gas puff lowers the ion temperature.

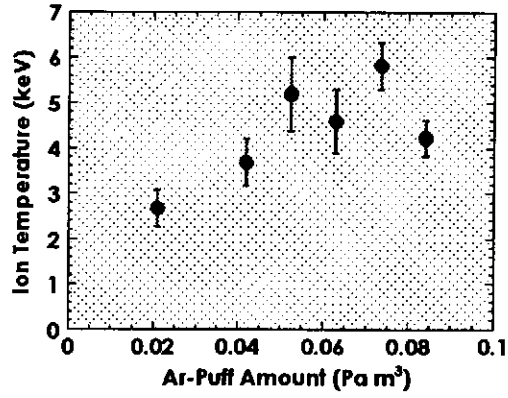

Fig. 4 Dependence of the ion temperature on the amount of the Ar gas puff.

Figure 5 shows the ion temperature as a function of the density-normalized NBI absorption power. Although the horizontal axis in the figure is the NBI power divided by the electron density, it roughly corresponds to the ion heating power divided by the ion density. In the Ne-puffed plasma, the ion temperature is achieved to about 5 keV at an

electron density of around $1x10^{19}$ m^{-3}, and is decreased below this density, probably because the ion number is not so relatively reduced due to the background hydrogen ions. In the Ar-puffed plasma, on the other hand, high-Z discharges are kept in lower densities less than $1x10^{19}$ m^{-3} due to its higher charge number. As a result, the density-normalized power is extended to higher values and the ion temperature is proportionally raised to 7 keV. It indicates that the ion temperature should be still increased linearly to the ion-density-normalized ion-heating power.

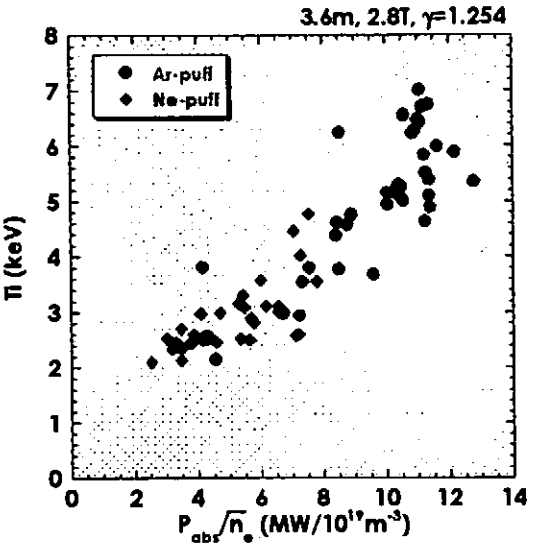

Fig. 5 Ion temperature as a function of the density-normalized NBI absorption power.

In the inward shifted configuration, $R_{ax} \leq 3.6$m, the neoclassical ripple transport is lower due to smaller helical ripple, and higher electron temperatures have been achieved. In the case of R_{ax}=3.75m, the achieved ion temperature is not so different from that in the case of R_{ax}=3.6m in the low-density high-Z plasmas, while the electron temperature is lower. The NBI heating profile is more centralized in R_{ax}=3.75m because a tangential radius of the NBI is 3.65–3.7m. Since the ion collisionality is high, plateau to collisional regime, due to Z^3 dependence, the ripple transport has no influence on the ion transport and the ion temperature should be dependent linearly on the heating power.

5. Summary

In the LHD, the ion temperature was much increased by high-power NBI injection of 10 MW in the Ne- and Ar-seeded high-Z plasmas. The ion temperature is increased with an increase in the density-normalized NBI-absorption power and reaches 7 keV. Saturation of the ion temperature increase to the heating power has not been observed yet. This result suggests that a high ion temperature should be achieved as well in hydrogen discharges if the direct ion heating power is increased to the same power as that in the Ar-seeded discharges.

References

[1] O. Kaneko, Y. Takeiri, K. Tsumori, *et al.*, 19th IAEA Fusion Energy Conference, Lyon, 2002, CT-6Rb.
[2] Y. Takeiri, T. Shimozuma, S. Kubo, *et al.*, Phys. Plasmas **10**, 1788 (2003).
[3] S. Morita, M. Goto, Y. Takeiri, *et al.*, 19th IAEA Fusion Energy Conference, Lyon, 2002, EX/P2-18.
[4] Y. Takeiri, O. Kaneko, K. Tsumori, *et al.*, Rev. Sci. Instrum. **71**, 1225 (2000).
[5] M. Osakabe, Y. Takeiri, T. Takanashi, *et al.*, Rev. Sci. Instrum. **72**, 586 (2001).

Analysis of ICRF Heating in LHD By Three-Dimensional Calculation

T. Seki, R. Kumazawa, T. Mutoh, A. Fukuyama[1], K. Saito, Y. Torii[2], N. Takeuci[2], T. Watari and LHD Experimental Group

National Institute for Fusion Science, Toki 509-5292, Japan
[1]Kyoto University, Kyoto 606-8501, Japan
[2]Nagoya University, Nagoya 464-8061, Japan

1. Introduction

Ion cyclotron range of frequencies (ICRF) heating is one of the heating methods for the plasma heating and has been used for many years for the plasma heating experiments. In the helical systems, it was theoretically predicted that the high-energy ions produced by ICRF heating escaped from the plasma and the ICRF heating was not effective for the ion heating. However, in LHD experiments, it is shown that the ICRF heating is effective in the helical device and the serious problem about confinement of the high-energy ions is not observed so far [1-4]. The ICRF heating has the potential to control the profiles of the plasma parameters by change of the power deposition profile. This is important for improvement of the plasma confinement. The study of the behavior of the high-energy ions generated by the ICRF heating is also important to understand the plasma confinement and instabilities. Therefore, evaluation of the ICRF heating is important for progress the confinement study of the plasmas heated by ICRF waves.

The full-wave code is one of the calculation method for analyze the ICRF heating. For helical devices, one-dimension and two-dimension codes have been used until now. These codes adapted the simplified magnetic configurations and do not include the complex magnetic field and the magnetic flux surface configurations. Then, the position between the ion

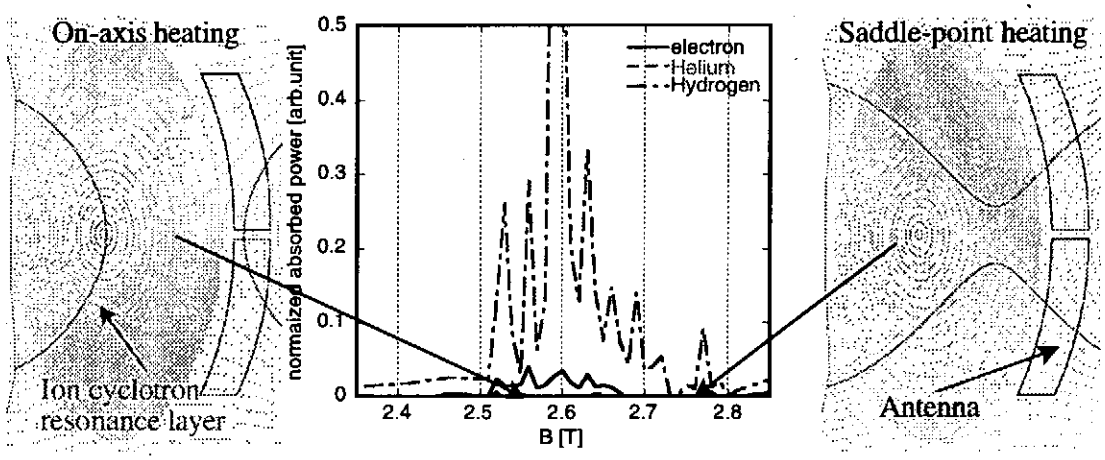

Fig.1. Dependence of power absorption on position of the ion cyclotron resonance layer.

cyclotron resonance layers and the plasma is different from the actual experimental situation. It is needed that the calculation model reflected the actual plasma configuration is utilized for the detail study. Three-dimensional calculation methods have been developed for reply to such demands. TASK/WM code is one of the global codes, which calculate three-dimensionally in the helical magnetic configuration.

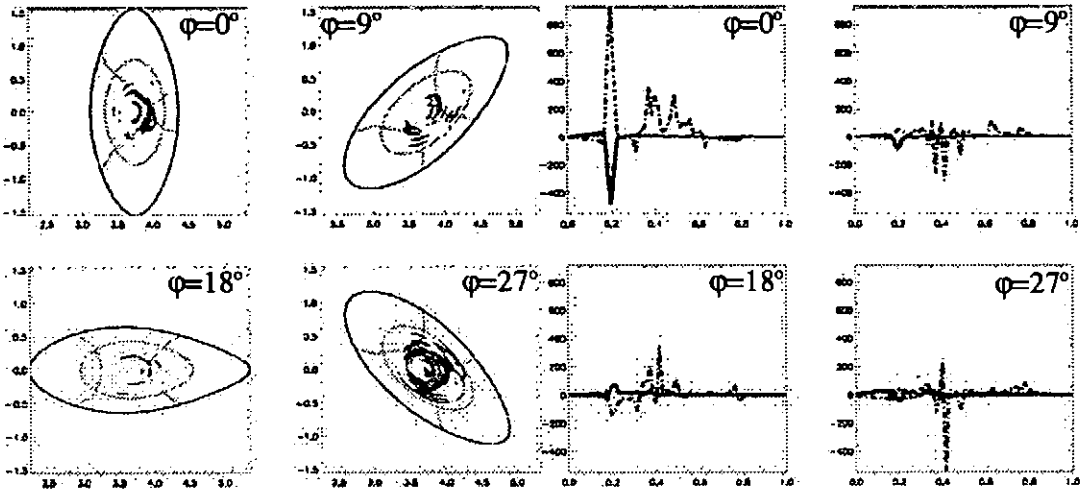

Fig. 2. Power absorption profile in case of the saddle-point heating. Poloidal plot shows the distribution of the hydrogen absorption and cyclotron layers. Purple is positive and yellow is negative. Radial plot shows the power absorption of all species of plasma. Line style of each species is same as Fig. 1.

2. TASK/WM code

The modeling of TASK/WM code was carried out by Dr. Vdovin et al. [5] and they were developed to calculation code by Dr. Fukuyama [6]. In a full-wave calculation, the toroidal and the poloidal harmonic expansions are used to solve the wave equation, $\nabla\times\nabla\times\mathbf{E}=\frac{\omega^2}{c^2}\bar{\varepsilon}\cdot\mathbf{E}+i\omega\mu_0\mathbf{j}_{ext}$, where ω is the wave frequency, E is the wave electric field, $\bar{\varepsilon}$ is the dielectric tensor, and $\mathbf{j}_{ext}$ is the external antenna current. The response of the plasma to the electromagnetic wave field is determined by the plasma current and the plasma conductivity tensor and expressed as $\mathbf{j}_p=\bar{\sigma}\cdot\mathbf{E}$. This is included through the plasma dielectric tensor. To solve the equation, finite Larmor radius expansion that assumes $k_\perp\rho<<1$, where $k_\perp$ is the perpendicular wave number and ρ is the ion Larmor radius, is used. Then, the effect of finite temperature is partially included and the cyclotron damping and the Landau damping are described. However, inclusion of the mode-converted ion Bernstein wave is incomplete. The spatial variations of the electric field and the medium are expanded in Fourier series in the toroidal and poloidal directions. The plasma configuration is given by VMEC MHD equilibrium code [7]. The calculation was carried out on the non-orthogonal flux coordinates

(ψ, θ, φ), where ψ is minor radius direction, θ is poloidal direction, and φ is toroidal direction. The antenna has a single loop in the poloidal direction for exciting the fast wave. The power absorption is expressed as $P = \mathbf{E} \cdot \mathbf{j}_p$.

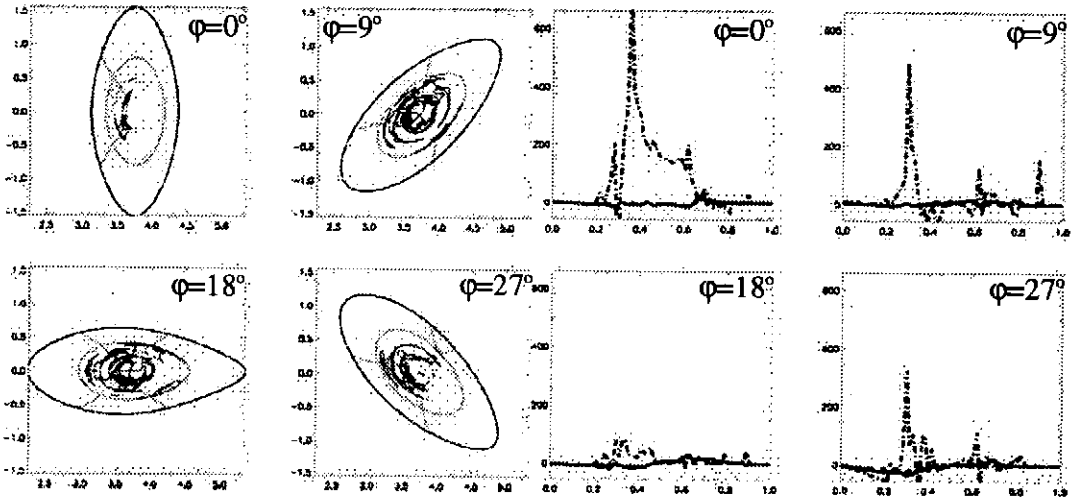

Fig. 3. Power absorption profile in case of the on-axis heating. The content of plot is same as Fig. 2.

3. Calculation Results

The absorption by hydrogen ion is very strong. If the ion cyclotron resonance layer of hydrogen exists in the plasma, most of absorption is generated by the hydrogen ion. Figure 1 shows dependence of the absorbed power in each species on the position of the ion cyclotron resonance layer. The central electron density and temperature are 1×10^{19} m^{-3} and 2 keV, respectively. Helium plasma with 10 % of hydrogen ion is assumed. In some cases the large electric field is resonantly generated and the absorbed power is amplified. To eliminate this effect, the power is normalized by square of the electric field. The position of the ion cyclotron resonance layer, which is the case of the heating at the saddle-point of the magnetic field configuration and the heating at the magnetic axis, are also shown in the figure. In the experiments, the best heating results are obtained in the saddle-point heating. However, in the calculation, larger hydrogen absorption is observed in the region between the saddle-point heating and on-axis heating. We investigated these heating cases taking notice of the toroidal absorption features. Figure 2 shows the power absorption profiles in the poloidal cross-section and along the normalized plasma minor radius at the four different toroidal angles. The main absorption is conducted by hydrogen ions. The power absorption mainly occurs at the toroidal angle of φ=0°, where the antenna is located. In this case, it looks like that optimization of the heating is attained only at φ=0°. Figure 3 shows the power absorption profile in case of the on-axis heating. A lots of power is absorbed at φ=0° as the same as the saddle-point heating. A small amount of power is absorbed at φ=9°

and φ=27°, which are the next calculation angles from the antenna location. Figure 4 shows the power absorption profile in the case that the ion cyclotron resonance layer is located between the saddle-point and the magnetic axis. The power is absorbed at all toroidal angles. This is large difference from the former two cases. The radio-frequency power, which is not absorbed near the antenna, can be absorbed at different toroidal angle. The difference of the power absorption in toroidal direction may affect on the property of the hydrogen absorption.

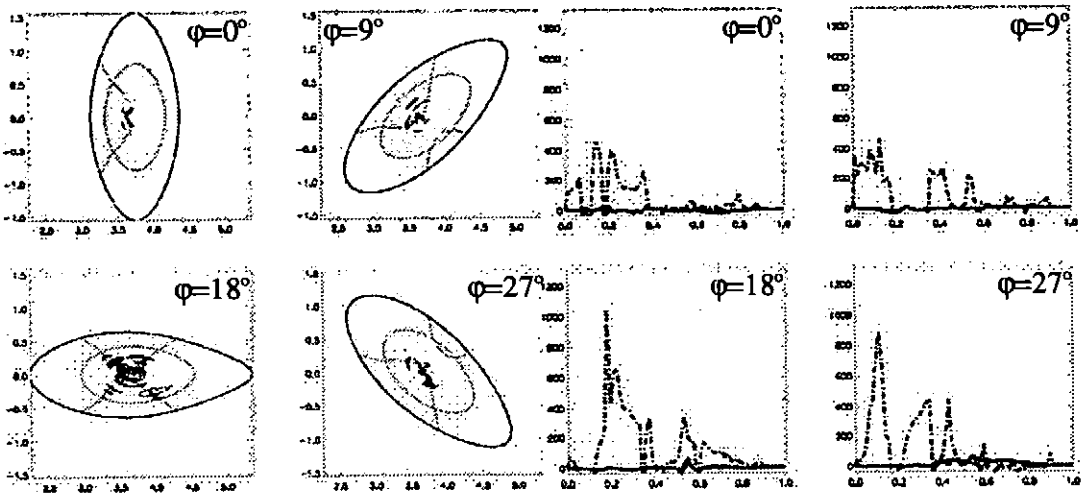

Fig.4. Power absorption profile in the case that the ion cyclotron resonance layer is located between the saddle-point and the magnetic axis. The content of plot is same as Fig.2.

4. Summary

The ICRF heating in helical device is investigated using the three-dimensional full wave code, TASK/WM. The dependence of the power absorption on the position of the ion cyclotron resonance layer is studied in detail and the strong ion absorption is observed when the ion cyclotron resonance layer is situated between the saddle-point and the magnetic axis. The power absorption in the toroidal direction is varied when the position of the cyclotron resonance layer is different. The difference of the toroidal power absorption may affect on the property of the total power absorption.

References

[1] T. Seki, et al., 14th Top. Conf. RF Power in Plasmas (2001) 67.
[2] R. Kumazawa, et al., to be published in Plasma Physics and Controlled Fusion.
[3] T. Mutoh, et al., IAEA Conference, 2002, Lyon, IAEA-CN-94/EX/P2-19.
[4] K. Saito, et al., to be published in 15th Top. Conf. RF Power in Plasmas (2003).
[5] V.L. Vdovin, et al., NIFS-469 (1996).
[6] A. Fukuyama, et al., IAEA Conference 2000, Sorrento, IAEA-CN-77/THP2/26
[7] S.P. Hirshman, et al., Comp.Phys. Comm. **39** (1986) 161.

30th EPS Conference on Contr. Fusion and Plasma Phys., St. Petersburg, 7-11 July 2003 ECA Vol. 27A, O-2.3A

EEFFECT OF L-H TRANSITION ON MHD STABILITY NEAR THE PLASMA EDGE IN THE LARGE HELICAL DEVICE

K. Toi, S. Ohdachi, S. Yamamoto [1)], S. Sakakibara, K. Tanaka, S. Morita, K. Narihara, N. Nakajima, T. Tokuzawa, K.Y. Watanabe, M. Goto, K. Ikeda, S. Inagaki, O. Kaneko, K. Kawahata, A. Komori, T. Masuzaki, K. Matsuoka , J. Miyazawa, K. Nagaoka, Y. Nagayama, Y. Oka, M. Osakabe, N. Oyabu, Y. Takeiri, K. Tsumori, H. Yamada, I. Yamada, and LHD Experimental Group.

National Institute for Fusion Science, Toki 509-5292, Japan
[1)]Dep. Energy Eng. Sci., Nagoya Univ., Nagoya 464-8603,Japan

1. Introduction

Improvement of global plasma confinement in a toroidal plasma is realized by formation of the transport barrier having a steep pressure gradient in the plasma edge and/or core regions. The H-mode with edge transport barrier (ETB) and ITB modes with internal transport barrier (ITB) are typical improved confinement regimes observed in not only tokamaks but also helical systems. Magneto-hydrodynamic (MHD) stability of these plasmas with transport barriers is an important issue for toroidal plasma confinement. MHD stability of a tokamak H-mode plasma seems to be determined by ballooning and/or peeling modes, where the plasma edge is in the magnetic well. On the other hand, H-mode discharges were obtained in helical devices such as CHS heliotron/torsatron [1] and W-7AS shearless stellarator [2]. Recently, on LHD that is a larger version of CHS but has a complete helical divertor, the L-H transition was observed in the so-called inward-shifted configuration. This configuration is favorable for particle confinement but is unfavorable for MHD stability because of wide magnetic hill region. MHD stability in the hill region is crucial for an LHD plasma. The formation of ETB in magnetic hill region provides an excellent opportunity to study MHD stability of edge region. In this paper, we present characteristics of the L-H transition in LHD plasmas and the impact of ETB on edge MHD stability.

2. Experimental Results

The L-H transition takes place in hydrogen and helium plasmas at low toroidal field (Bt=0.5 T to 0.75T) where the toroidal (diamagnetic) beta value $<\beta_t>$ is more than ~1.5%[3]. So far, the transition is observed in the magnetic configurations of R_{ax}=3.6m and 3.55 m (R_{ax}: the magnetic axis position of the vacuum field). Although detailed heating power scan is not yet done, absorbed NBI heating power is required to be more than ~2.5 MW for the above plasma conditions. The heating power is about two times larger than that predicted by the ITER H-mode power threshold scaling for hydrogen

plasma [4].

A typical hydrogen discharge with the L-H transition is shown in Fig.1, where R_{ax}=3.55m, toroidal field B_t=0.75T, and absorbed NBI power P_{NBI}=4.3 MW. The transition takes place at t=1.749s, exhibiting rapid depression of H_α light and rapid increases in the line averaged electron density $\langle n_e \rangle$ and the plasma stored energy W_p. At the transition, the density profile becomes further broad, as seen from Fig.1(b) which shows a radial profile of the relative increase in line integrated electron density. Note that the electron density profile obtained by Abel inversion is slightly hollow both in L- and H-phases, having different density gradient near the edge. In some shots, the electron

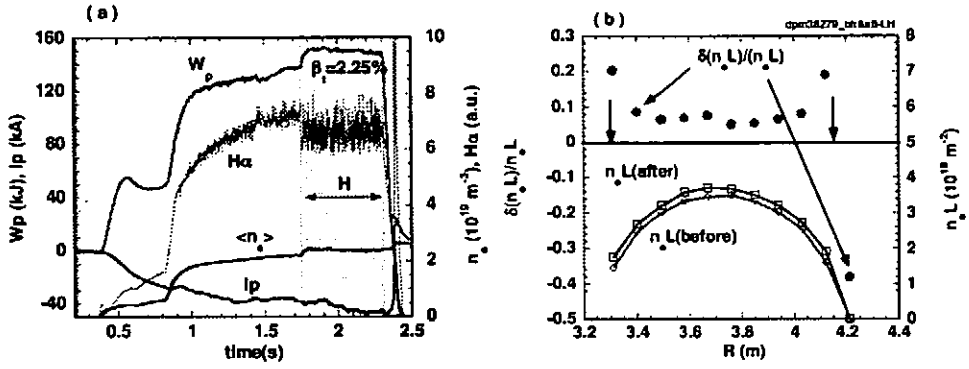

Fig.1(a) A typical hydrogen plasma with the L-H transition, where Bt=0.75T, Rax=3.55 m, and PNBI=4.3 MW.

(b) Relative increase in line integrated electron density across the L-H transition, where data at t=1.74s and t=1.77s are compared each other. The vertical arrows indicate the LCFS of the vacuum field.

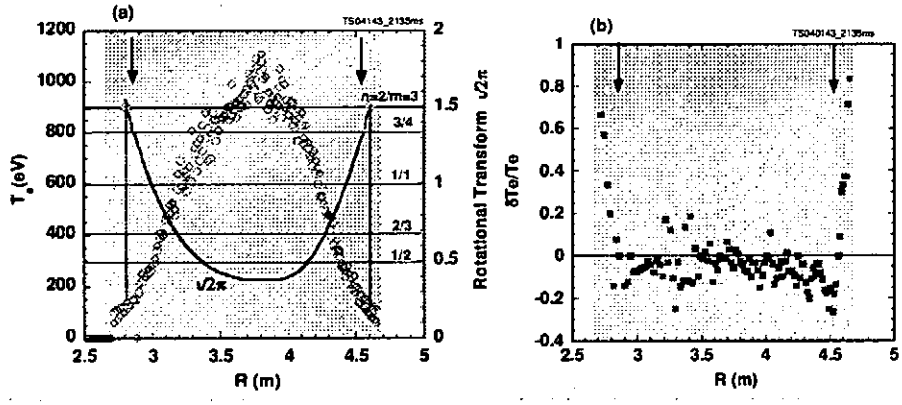

Fig.2(a) Radial profiles of electron temperature just before (blue diamonds) and after (red circles) the transition, and rotational transform profile for the vacuum field. Two arrows stand for LCFS of the vacuum field. The shaded zone indicates the expected plasma region. (b) Radial profile of the relative increase of electron temperature across the transition.

temperature at the very edge appreciably rises across the transition (Fig.2). Improvement of particle confinement time is roughly estimated to be by about 30 % from the rates of the density rise and the reduction of Hα-light. The improvement of global energy confinement, however, is fairly small (<10%) for ISS95 scaling. This modest improvement of plasma confinement in LHD with helical divertor is quite similar to that in a CHS H-mode plasma bounded by a limiter. Note the plasma boundary in relatively high beta regime (>1.5%) slightly expands into the ergodic layer beyond the last closed flux surface (LCFS) defined in the vacuum field (Fig.2). This fact was first reported in ref.[5]. The ETB formation outside LCFS of the vacuum field supports the fact of the plasma expansion.

As seen from Fig.1, the H_α-light is clearly depressed at the transition and a quiescent phase that $<n_e>$ and $<\beta_t>$ linearly increase persists for a short interval (up to ~10ms). Then, the H_α-light is modulated by small but frequent ELMs, of which amplitude is enhanced by about 30% having high repetition rate up to 500 Hz. Figure 3 shows a typical shot with constant gas puffing where ELMs obviously affect the stored energy or the toroidal beta. The occurrence of ELMs limits the improvement of global energy confinement. Of course, the ELMs prevent from the increase in impurity concentration.

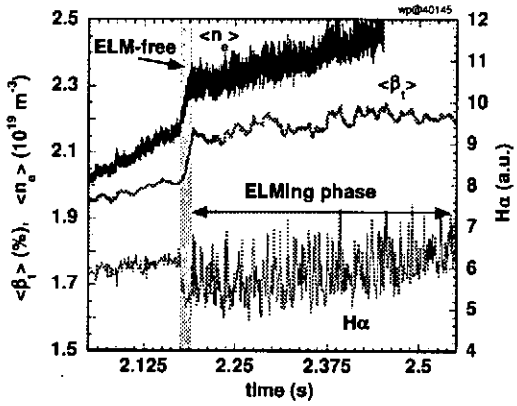

Fig.3 Time evolution of $<\beta_t>$, $<n_e>$ and Hα-light in an H-mode discharge that ELMs clearly affect the stored energy or $<\beta_t>$, where $<n_e>$ is continuously increased by gas puffing.

At the L-H transition of LHD plasmas, magnetic fluctuations are strongly enhanced as shown in Fig.4. The dominant mode is m=2/n=3 (m, n: poloidal and toroidal mode number) of which relevant rational surface is in the vicinity of ETB. In this shot m=2/n=2 mode was enhanced but suppressed by the first ELM. The Hα-light spikes by ELMs correlate well with m=2/n=3 mode bursts. This edge MHD mode is thought to be resistive interchange mode because the rational surface is in high magnetic shear region but in the magnetic hill. The m=2/n=3 mode rotates with 2-6 kHz in the electron diamagnetic drift direction. If the MHD mode saturates by local flattening of the pressure profile at the rational surface, the mode frequency approximately corresponds to the ExB drift frequency. In a typical shot at Bt=0.75 T, the frequency of ~6 kHz gradually decreases to ~3.5 kHz with the increase in $<\beta_t>$, and suddenly decreases down to ~2.5 kHz at the transition. This means that the radial electric field Er at the $\iota/2\pi = 3/2$ rational surface evolves from about –4 kV/m (inward) in L-phase to about –3 kV/m in H-phase, where m=2 is taken into account. However, there is no information about the change of the Er shear. For the edge region of these plasmas, data of charge recombination spectroscopy are not available. Note that

Repetitive Pellet Fueling on LHD

R. Sakamoto, H. Yamada, Y. Takeiri, K. Tanaka, T. Tokuzawa, S. Masuzaki, H. Suzuki,
S. Sakakibara, M. Goto, S. Morita, B.J. Peterson, Y. Nagayama, K. Matsuoka,
N. Ohyabu, O. Motojima and the LHD experimental group
National Institute for Fusion Science, Japan

1. Introduction

For the purpose of investigations of fueling issues towards the steady state operation of fusion plasmas, a repetitive pellet injector with compact cryo-coolers has been developed. This injector has been installed to Large Helical Device (LHD), which is a heliotron type device with super-conducting coils, and repetitive pellet fueling experiments have been started.

Our previous study with a conventional pipe-gun type pellet injector indicates that pellet fueling has transiently extended the operational region of the LHD plasmas to higher densities, which cannot be attained by gas puffing while maintaining the favorable dependence of the energy confinement on the density [1]. If this advantage of the pellet fueling is demonstrated in steady state operation, pellet fueling offers significant advantage for future a fusion reactor.

2. Experimental set-up

Fig. 1 (a) shows the schematic drawing of the repetitive pellet injector that is based on a screw-extruder [2], which is capable of solidification of hydrogen and continuous extrusion the 2.5 mmϕ solid hydrogen rod at a rate of 35 mm/s (Fig. 1 (b)). This facility is capable of completely steady state pellet injection in principle with the repetition rate up to 11 Hz [3]. Maximum pellet mass is 5×10^{20} atoms per pellet, and the mass is adjustable by changing the extruding speed of the solid hydrogen. The pellet velocity is adjustable in the range of

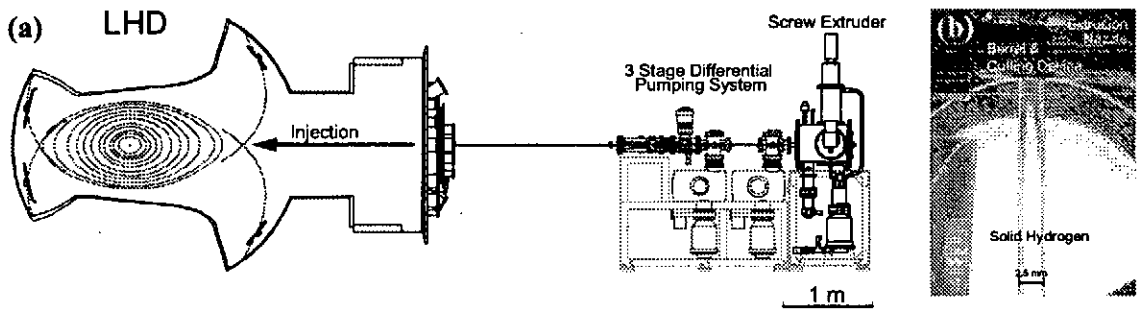

Fig. 1 (a) The schematic drawing of the repetitive pellet injector for LHD.
(b) The photo image of continuously extruded solid hydrogen.

Measurement of the Damping Rate of Toroidicity-Induced Alfvén Eigenmodes in the Compact Helical System

G. Matsunaga, K. Toi, C. Suzuki, K. Matsuoka and CHS Group

National Institute for Fusion Science, Toki 509-5292, Japan

The researches of Alfvén eigenmodes (AEs) such as toroidicity-induced Alfvén eigenmodes (TAEs) are being carried out in major tokamaks [1] and helical devices [2–4]. Because unstable AEs have a potentiality of enhancing the loss of energetic alpha particles in a future burning plasma. Therefore, the stability of AEs is very important and interesting issues. The stability of AEs is determined from the competition between energetic ion drive (growth rate : γ_g) and various damping effects (damping rate : γ_d). The stability of AEs is evaluated by the effective damping rate $\gamma_{eff} = \gamma_d - \gamma_g$. Several damping mechanisms for AEs are taken into account in stability analysis of AEs [5], that is, electron Landau damping, ion Landau damping, collisional damping, continuum damping and radiative damping. In the JET tokamak, excitation of AEs without energetic ions was attempted by using saddle coils installed inside the vacuum vessel, and the damping rate of AEs was experimentally evaluated from the plasma response to applied magnetic perturbations [6]. On the other hand, several types of AEs excited by energetic ions were already observed in a plasma of the Compact Helical System (CHS) heliotron/torsatron [3, 4]. The CHS is $l = 2$ heliotron/torsatron with the toroidal field period number $N = 8$, where the major and averaged minor radii of the plasma are $R \simeq 1$ m and $\langle a \rangle \simeq 0.2$ m, respectively. The magnetic shear is negative in a whole plasma region and is high near the edge. In this configuration, the strong continuum damping is expected.

For this reason, development of a new system is required to excite AEs without energetic ions and to measure the eigen-frequency and the damping rate [7]. This system is designed to apply to a low temperature and low density plasma where measurement of internal structures of AEs becomes easy by using an insertable magnetic probe array. This system consists of two electrodes that are arranged apart from 180 degrees in the toroidal direction to specify the toroidal mode number n. The electrode has a metallic plate of 30 mm × 10 mm size perpendicular to the equilibrium magnetic field line. One side of the metallic plate is insulated with a block of boron-nitride to specify the path of oscillatory current in one direction. The most significant point of this system is that magnetic perturbations induced by the oscillatory current are perpendicular to the equilibrium magnetic field, and would generate shear Alfvén waves very effectively. In this experiment, the electrodes were inserted inside the last closed flux surface (LCFS) up to the radial position $\rho\ (= r/\langle a \rangle) \simeq 0.6$ in a low density and low temperature helium plasma. The plasma was produced with 2.45 GHz electron cyclotron resonance (ECR) up to 1 kW at low magnetic field (~ 0.09 T). Typical electron density and electron temperature of the plasma are $\sim 3 \times 10^{16}$ m^{-3} and ~ 4 eV, respectively. The expected TAE gap frequency and position are in the range of $100 - 300$ kHz and $\rho \leq 0.8$, respectively. The peak voltage applied to each electrode is ± 75 V, and the electron saturation current reaches to the order of 200 mA. When the electrodes are placed at $\rho \simeq 0.65$, the oscillatory current will flow on the

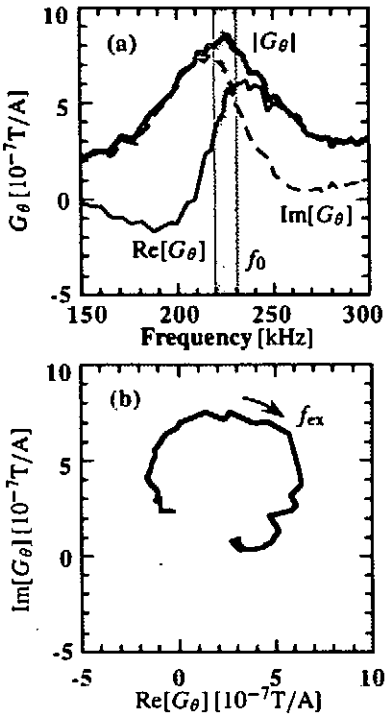

Fig. 1 (a) Absolute $|G_\theta|$, real part $\mathrm{Re}[G_\theta]$ and imaginary part $\mathrm{Im}[G_\theta]$ of the transfer function G_θ. (b) The transfer function in the complex plane.

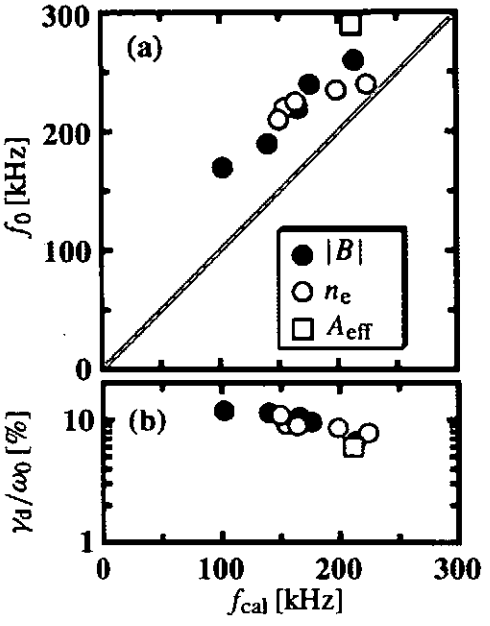

Fig. 2 Observed resonance frequency and damping rate of excited TAEs for several experimental conditions (toroidal magnetic field, electron density and mass of gas).

magnetic field line that is on the magnetic surface of $\iota \simeq 2/4$, where ι is the rotational transform. Accordingly, the generated dominant Fourier mode is $m = 4/n = 2$ (m, n: poloidal and toroidal mode numbers) and the sideband of $m \pm 1$ mode components will also be generated through a toroidal effect.

A resonance character in a plasma response for applied magnetic perturbations is successfully derived from the transfer function defined as $G_\theta(f) = b_\theta(f)/I_0(f)$, where $b_\theta(f)$ and $I_0(f)$ are the Fourier transforms of poloidal magnetic field fluctuations excited in a plasma and oscillatory current induced by electrodes, respectively. When the frequency of the current is swept in the frequency range covering TAE gap frequency (f_{TAE}), $G_\theta(f)$ would exhibit a character of resonance behavior related to f_{TAE}. An example of the transfer function obtained in this experiment is shown in Fig. 1, where the electrodes are placed at $\rho \simeq 0.65$ near the relevant TAE gap. In Fig. 1(a), the absolute value $|G_\theta|$, real part $\mathrm{Re}[G_\theta]$ and imaginary one $\mathrm{Im}[G_\theta]$ are shown as an enlarged figure around the resonance frequency f_0. The transfer function draws a circle in the complex plane around the resonance frequency f_0, as shown in Fig. 1(b). The toroidal mode of the induced magnetic fluctuations was derived as $n = 2$ from the toroidal array of magnetic probes. Plasma parameters related to the Alfvén velocity v_A, that is, the toroidal field B_t, the electron density n_e and the mass of the fuel ion A_i are varied in order to confirm that this resonance is related to TAEs, where the density is scanned by the

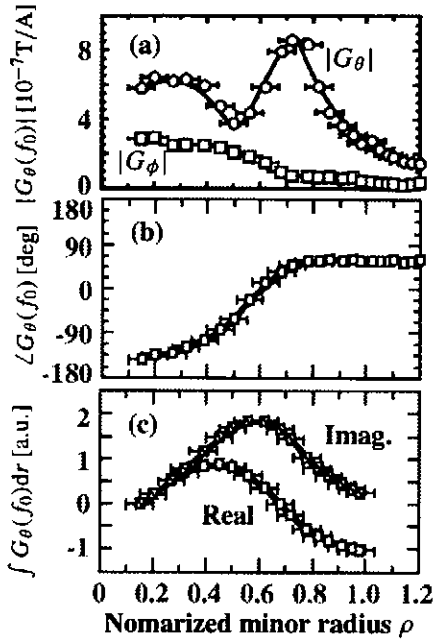

Fig. 3 Radial profile of the transfer function. (a) The absolute, (b) the phase of the transfer function and (c) the eigenfunctions $\int G_\theta(\rho)dr$.

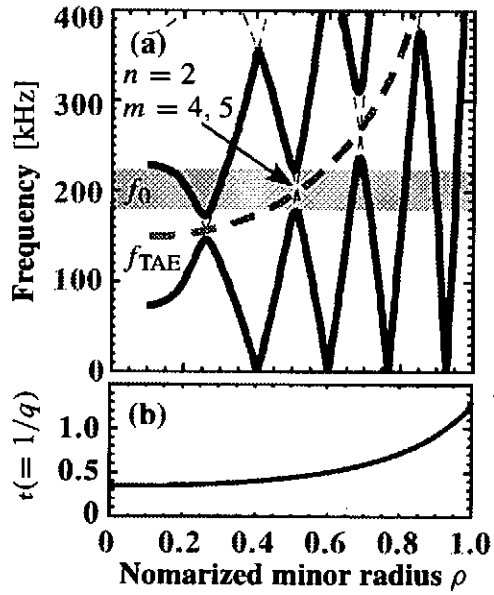

Fig. 4 Calculated Alfvén continua for $n = 2$ in a helium plasma produced by 2.45 GHz ECR.

change of ECR heating power. Figure 2 indicates the relationship between the observed resonance frequency f_0 and the calculated TAE gap frequency $f_{cal} = [v_A t/(4\pi R)]_{\rho=\rho_0}$. Here, f_{cal} was evaluated as that of the TAE gap formed at $\rho = \rho_0 \simeq 0.5$ by the poloidal mode coupling between $m = 4$ and $m = 5$ Fourier modes, where $\iota(\rho_0) = 0.44$. This figure clearly indicates that the resonance is related to TAEs. In a plasma without fast ions such as 2.45 GHz ECR produced plasma, the effective damping rate is equivalent

for the damping rate γ_d because of $\gamma_g = 0$. Therefore, the damping rate is evaluated from the half width of the resonance around the resonance frequency f_0 shown in Fig. 1(a). Thus derived damping rate is fairly large to be $\gamma_d/\omega_0 \sim 10\%$, where $\omega_0 = 2\pi f_0$, as shown in Fig. 2(b)

It is important and interesting to get spatial information of AEs. The radial profile of the poloidal $|G_\theta|$ and toroidal component $|G_\phi|$ of the transfer function at $f = f_0$ is shown in Fig. 3(a). $|G_\phi|$ is obviously smaller than $|G_\theta|$ indicates that the induced magnetic fluctuations have a character of shear Alfvén waves. The magnitude $|G_\theta|$ has a peak around $\rho \simeq 0.75$, and the phase $\angle G_\theta$ is inverted at $\rho \simeq 0.6$ (Fig. 3(b)). The radial displacement of TAE may be derived from the data shown in Fig. 3(a). If a cylindrical configuration is assumed for simplicity, the radial displacement ξ_r is roughly evaluated as $\xi_r \simeq -\frac{1}{B_p}\int_0^a b_\theta dr \propto \int_0^a G_\theta dr$. The spatial integration of G_θ is shown in Fig. 3(c). This indicates that the eigenmode has a peak in the radial location of $\rho \simeq 0.4 - 0.6$. The $n = 2$ shear Alfvén continua are calculated for a helium plasma obtained by 2.45 GHz ECR, where a singly ionized helium plasma is

assumed because of low T_e and the ion density profile shape of the electron density (Fig. 4(a)). Here, the rotational transform profile in the $R_{ax} = 97.4$ cm magnetic configuration of zero plasma pressure is adopted (Fig. 4(b)). The eigen-frequency obtained with the transfer function is indicated by a gray zone and agrees well with the TAE gap frequency related to $m = 4$ and $m = 5$ mode coupling. If the eigen-function extends as shown in Fig. 3(c), the excited $n = 2$ TAE would suffer from considerable continuum damping in the edge region outside the relevant TAE gap.

Electron and ion Landau damping can be neglected because electron and ion pressures are very low in the present plasma condition. In this plasma, the ionization degree is fairly low ($\sim$ 5%). The neutral density is on the order of $\sim 10^{17}\,\mathrm{m}^{-3}$. The collision frequency of electrons with neutrals is about 110 kHz. This neutral effect on the damping rate, however, is negligibly small [8]. Continuum damping is estimated using equation of Ref.[9]. Around $\rho \geq 0.7$ where the eigen-function of this mode interacts with the Alfvén continuum, the damping rate is estimated to be $\sim 5-20\%$. It is consistent with experimental result. Radiative damping is expected to be sensitive to ion gyroradius, but the damping rates for hydrogen and helium plasmas are almost same. It is thought that the radiative damping is not important in this experimental condition.

In conclusion, the TAEs in a low density and low temperature plasma of CHS were effectively excited with a newly developed electrode technique. The eigen-frequency and damping rate of the excited TAE were successfully derived from the characteristics of the measured transfer function G_θ. The frequency agrees well with the $n = 2$ TAE gap frequency related to $m = 4$ and $m = 5$ mode coupling. The derived damping rate of $\sim 5 - 10\%$ is thought to be dominantly caused by continuum damping. Application of this electrode technique to a low temperature and low density plasma will has an advantage for basic understanding of excitation and damping of TAEs in heliotron/torsatron configuration which has fairly high edge magnetic shear.

References

[1] K. L. Wong, Plasma Phys. & Controlled Fusion **41**, R1 (1999).

[2] A. Weller et al., Phys. Plasmas **8**, 931 (2001).

[3] M. Takechi et al., Phys. Rev. Lett. **83**, 312 (1999).

[4] K. Toi et al., Nucl. Fusion **40**, 1349 (2000).

[5] E. J. Strait et al., Nucl. Fusion **33**, 1849 (1993).

[6] A. Fasoli et al., Phys. Rev. Lett. **75**, 645 (1995).

[7] G. Matsunaga et al., Rev. Sci. Inst. **72**, 402 (2001).

[8] Y. Amagishi and A. Tsushima, Plasma Phys. & Controlled Fusion **26**, 1489 (1984).

[9] M. N. Rosenbluth et al., Phys. Rev. Lett. **68**, 596 (1992).

Particle transports and related turbulent fluctuations on LHD

K. Tanaka[1], L. N. Vyacheslavov[2], A. Sanin[1], T. Akiyama[1], K. Kawahata[1], T. Tokuzawa[1], Y. Ito[1], S. Tsuji-Iio[3], S. Okajima[4], H. Yamada[1], S. Morita[1], M. Goto[1], J. Miyazawa[1], K. Ida[1], Y. Takeiri[1], M.Yokoyama[1], S. Murakami[5], A. Wakasa[6] and LHD Experimental Group[1]

[1]*National Institute of Fusion Science, Toki, Japan*
[2]*Budker Institute of Nuclear Physics, Novosibirsk, Russia*
[3]*Tokyo Institute of Technology, Tokyo, Japan*
[4]*Chubu University, Kasugai, Japan*
[5]*Kyoto University, Kyoto, Japan*
[6]*Hokkaido University, Sapporo, Japan*

Microturbulence is one of the most important physical mechanisms, which determines the anomalous transport. Turbulent fluctuations can induce enhanced particle and energy fluxes. In order to understand correlations between transport and fluctuations, the estimation of transport coefficients and measurements of the fluctuations are necessary. Density modulation experiments were run to estimate diffusion coefficients and convection velocities of particles in the plateau regime of LHD. These were done on a typical configuration with Rax (the magnetic axis position) = 3.6 m, where the best global energy confinement time was achieved. The density fluctuations which reveal microturbulence were measured by Phase Contrast Interferometer (PCI).

Fig. 1 (a) and (b) show electron temperature and density profiles in NBI heated discharges, which were measured by Thomson scattering and with a multi- channel interferometer. As shown in Fig. 1, the density profiles change from peaked profiles to flat ones along with the increase in electron temperature by higher NBI heating power. This suggests there is a strong link between the electron temperature and the density profile.

The difficulty of the particle transport analysis is experimental indeterminacy of the particle source and the existence of a convection term. The particle flux can be written as the sum of diffusion and convection terms as follows.

$$\Gamma = -D\nabla n_e + n_e V \quad (1)$$

Here, D is a diffusion coefficient, V is a convection velocity. The particle balance equation is the following.

$$\frac{\partial n_e}{\partial t} = -\nabla \cdot \Gamma + S = -\frac{1}{r}\frac{\partial}{\partial r} r\Gamma + S \quad (2)$$

Here S is a particle source rate of electrons. If the particle source, which is localized at the edge, is modulated, the modulated density propagates from the edge to the core.

Parameters D and V characterize this propagation. From the analysis of modulated components, D and V can be determined independently of the absolute value of the particle source, which is difficult to estimate experimentally[1]. For simplicity of the analysis, spatially constant D and V(r)=r/a V are used for the analysis. The source profile (only relative shape) is obtained from Hα measurements in the edge region and 1-D calculation of the neutral penetration in the core region. The amplitude of the density modulation was kept less than 2.5% of the line density along the central chord. The modulation frequency was 2 and 5 Hz, which was determined to have about 5 ~ 10 periods during a density flattop.

Fig. 2 shows spatial profiles of the amplitude and the phase of modulated density, which fit experimental data. From Fig. 1 (b), the difference of the background density profile at $\rho > 0.7$ is small, however, the difference of modulated components (amplitude and phase) becomes clearer in as shown Fig. 2.

Fig. 3 (a) shows the dependence of particle and thermal diffusion coefficients on electron temperature at $\rho = 0.75$ under constant density. In this series of experiments, the density at $\rho = 0.75$ was kept constant at $1.27(+-0.08)\times10^{19}m^{-3}$. Experimentally obtained D are values from 2 and 5 Hz from modulation experiments. As shown in fig. 2 (b), the modulation amplitude has a peak around are $\rho = 0.75$. This indicates modulation results has a weight around $\rho = 0.75$, although simple constant D are used for analysis. Neoclassical values (D_{neo}) are calculated with DCOM[3] at $\rho = 0.75$. Thermal diffusion coefficients χ_{eff}, which is defined as flows,

$$\chi_{eff} = -\frac{Q_e + Q_i}{n_e \nabla T_e + n_i \nabla T_i} \qquad (3)$$

is calculated from power balance analysis calculated with PROCTR[2]. This definition is used since it is difficult to evaluate the equipartition between electrons and ions.

The followings are concluded from fig. 3 (a). 2 Hz and 5 Hz modulation indicates almost same values. Spatially constant D model can fit experimental data well. This suggests D is spatially almost constant in the edge, where modulated region at $\rho > 0.5$. χ_{eff} is 3 ~ 5 times larger than D_{exp}. The particles are better confined than energy. T_e is dominant parameter to determine D_{exp} under constant density in this experiment regime (plateau regime) and the following dependence are obtained.

$$D_{exp} \propto T_e^{1.38} \qquad (4)$$

The correlation function of the fitting of eq. (4) is 0.94. This temperature dependence of

D is close to gyro-Bohm diffusion like behavior ($\propto T_e^{1.5}$). D_{exp} is more than one order larger than D_{neo}. The particle diffusion is anomalous in this experimental regime. However, the difference between D_{exp} and D_{neo} becomes slightly smaller at higher T_e.

Fig.3 (b) shows temperature dependence of V. Unlike fig. 3 (a), very weak temperature dependence is observed. And fitting determination of V is worse than that of D. These suggest existence of the hidden parameter and imply that present model V(r)=r/a V is not appropriate. However, it can be concluded inward pinch exists taking into account the fitting error. The particle flux including off-diagonal terms is expressed as follows.

$$\Gamma = -D_n \nabla n_e - D_t n_e \nabla T / T - D_n e E_r (n/T) \qquad (5)$$

In Eq. (5), the first and the second terms show outward direction. Since radial electric field Er is predicted to be negative from the neoclassical theory[4] (experimental data of Er was not available, but Er follows neoclassical prediction well in LHD[4]), the third term becomes outward direction as well. Therefore, the observed inward pinch is contradictory to neoclassical prediction.

Microturbulence is observed by PCI in two different confinement discharges within $0.1 < k_{poloidal} < 1.25$ mm^{-1} and $5 < f < 125$ kHz ranges. By using magnetic shear, local measurement around the minor radius was possible[5].

One discharge is 1-MW and the other is 6.5-MW NBI heating both with Rax = 3.6 m, the global energy confinement time is 264 and 94 ms respectively. The difference of the temperature from the available data, which is central ion temperature from Doppler broadening of ArXVII resonance line measured with a crystal spectrometer, is factor 1.5. From eq. (4), this difference results in factor $1.5^{1.38} = 1.7$ change of D. From fig. 3 (a) and (b), factor 1.5 in temperature difference results in modification of D rather than V. As shown in Fig. 4, the edge density is almost the same, however, a clear difference of the spectrum of the fluctuation was observed as shown in Fig.4 (b) and (c).

For simple random motion diffusion process, if the diffusion process is determined by turbulence, the diffusion coefficient is given as follows,

$$D_{random} \propto \frac{(Correlation\ \ length)^2}{Correlation\ \ time} = \frac{\delta f}{k^2} \qquad (6)$$

Here, δf is the frequency width and k is the perpendicular wave number of turbulence. For worse confinement (6.5-MW heating), the width of frequency spectrum is around 2.4 times wider than that of the better confinement (1-MW heating), and the peak wave number is 2/3

of the case with 1-MW heating as seen in Fig.4 (b) and (c), respectively. This results in,

$$\frac{D_{6MWheating}}{D_{1MWheating}} \approx 2.4x(3/2)^2 = 5.4 \qquad (7)$$

This does not agree expected factor 1.7 difference of D. The uncertainty of frequency width can affect. However, rough correlation between increase of D and change of fluctuation spectrum is observed.

References

1) K.W. Gentle *et al.*, Plasma Phys. Contr. Fusion **29**, 1077 (1987).
2) H.C. Howe, ORNL/TM-11521 (1990).
3) S. Murakami *et al.*, Nuclear Fusion **42** (2002) L19-L22.
4) M.Yokoyama *et al.*, Nucl. Fusion **42** (2002) 143.
5) A. Sanin *et al.*, in this proceedings.

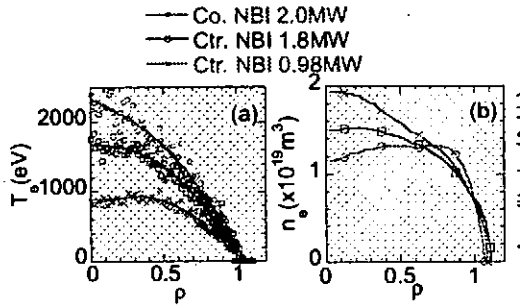

Fig.1 Background profiles (a) Te and (b) ne of density modulation experiments at Rax=3.6m, Bt=2.8T

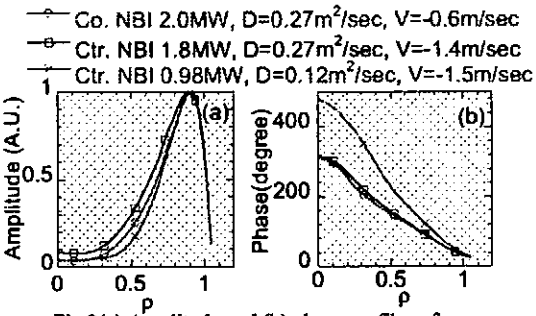

Fig.2(a) Amplitude and (b) phase profiles of 5Hz density modulation. Negative V indicates inward direction

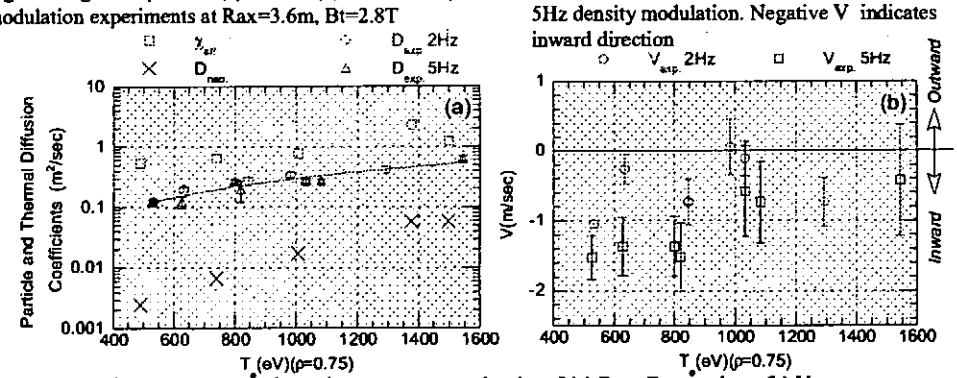

Fig.3 Temperature dependence at constant density of (a) $D_{exp.}$, $D_{neo.}$ and χ_{eff} (b) V. Errors are fitting error of the model.

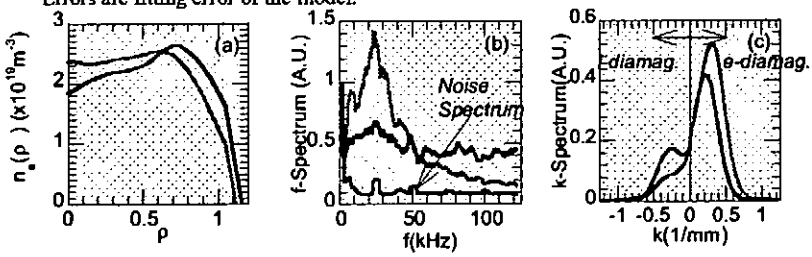

Fig.4 (a) ne profiles, power spectrums of (b) frequency and (c)wave number. Red lines indicate P_{NBI}=1MW,τ_c=260ms,Ti(0)=1.3keV, Blue lines indicate P_{NBI}=6.5MW,τ_c=94ms,Ti(0)=1.9keV.

Repetitive Pellet Fueling on LHD

R. Sakamoto, H. Yamada, Y. Takeiri, K. Tanaka, T. Tokuzawa, S. Masuzaki, H. Suzuki,
S. Sakakibara, M. Goto, S. Morita, B.J. Peterson, Y. Nagayama, K. Matsuoka,
N. Ohyabu, O. Motojima and the LHD experimental group
National Institute for Fusion Science, Japan

1. Introduction

For the purpose of investigations of fueling issues towards the steady state operation of fusion plasmas, a repetitive pellet injector with compact cryo-coolers has been developed. This injector has been installed to Large Helical Device (LHD), which is a heliotron type device with super-conducting coils, and repetitive pellet fueling experiments have been started.

Our previous study with a conventional pipe-gun type pellet injector indicates that pellet fueling has transiently extended the operational region of the LHD plasmas to higher densities, which cannot be attained by gas puffing while maintaining the favorable dependence of the energy confinement on the density [1]. If this advantage of the pellet fueling is demonstrated in steady state operation, pellet fueling offers significant advantage for future a fusion reactor.

2. Experimental set-up

Fig. 1 (a) shows the schematic drawing of the repetitive pellet injector that is based on a screw-extruder [2], which is capable of solidification of hydrogen and continuous extrusion the 2.5 mmϕ solid hydrogen rod at a rate of 35 mm/s (Fig. 1 (b)). This facility is capable of completely steady state pellet injection in principle with the repetition rate up to 11 Hz [3]. Maximum pellet mass is 5×10^{20} atoms per pellet, and the mass is adjustable by changing the extruding speed of the solid hydrogen. The pellet velocity is adjustable in the range of

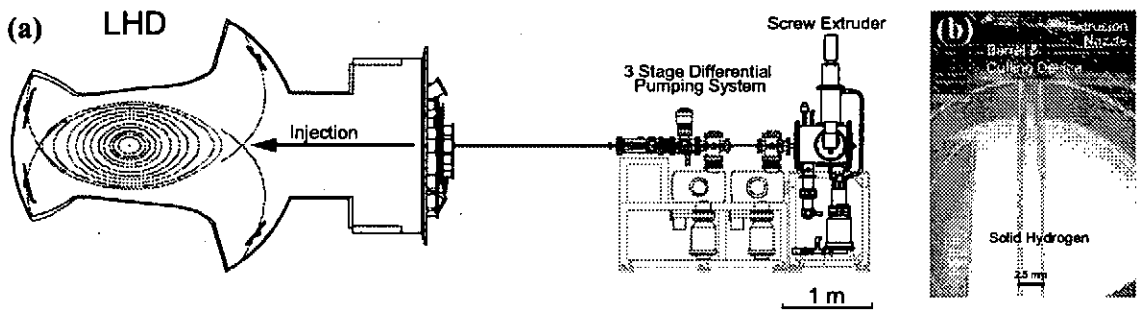

Fig. 1 (a) The schematic drawing of the repetitive pellet injector for LHD.
(b) The photo image of continuously extruded solid hydrogen.

150-550 m/s.

The hydrogen pellets are injected into NBI heated hydrogen plasmas with the standard magnetic configuration (R_{axis}= 3.6 m, B_t≈ 2.8 T) from an outboard side at the horizontal elongated cross-section. Typical NBI heating power is 4 - 5 MW for 5 s discharges at the energy of 130 - 150 keV. Effective pumping speed of the vacuum vessel is about 150 m^3/s and there is no active pumping at divertor.

3. Experiments and discussion

Though deep inside fueling is one of the important purposes for pellet fueling, it is necessary to avoid perturbation in the core region. Therefore we use relatively small size pellet for a repetitive injector compared to the existing in-situ pipe gun injector, which have 3 mmϕ barrels. Fig .2 shows the temporal change of ablation light and electron density for one pellet injection. Typical density rise per pellet just after pellet ablation is around 1.5×10^{19} m^{-3} and this is consistent with pellet mass, namely the pellet mass is 5×10^{20} atoms/pellet and the plasma volume is 30 m^3. The penetration depth that is estimated from the duration of the ablation light (H_α) is 20–30 cm, namely a pellet penetrates to around 0.7 in the normalized minor radius, and these value are consistent with a prediction from the scaling of neutral gas shielding model [4]. Outward density redistribution just after the pellet ablation within several 100 μs was observed, and then density peaking due to rapidly decreasing the boundary density proceeds on the several 100 ms time scale.

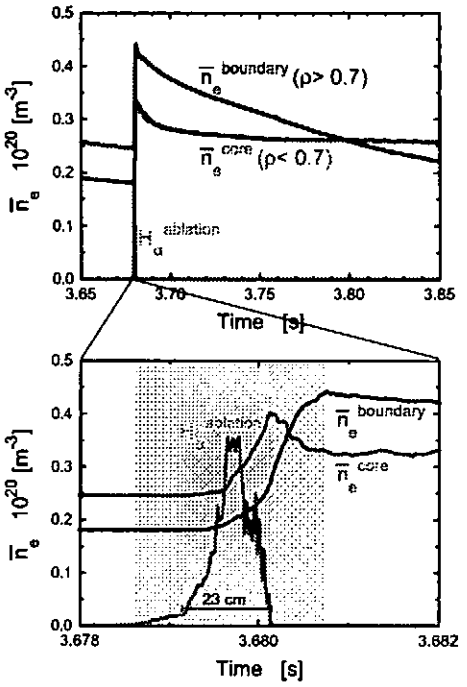

Fig. 2 The temporal evolution of the ablation light and electron density.

Fig. 3 shows typical waveform of the repetitive pellet fueling discharge. 50 pellets were injected with repetitive rate of 10 Hz to a NBI heated plasma. Quasi steady-state operation of 2 s was achieved at plasma parameters of $\bar{n}_e$= 0.8×10^{20} m^{-3}, T_i= 1.3 keV, T_e= 1.0 keV with 4 MW NBI heating from 3.6 s to 5.6 s. In this quasi steady state phase, the line averaged

electron density ($\bar{n}_e$) and the center temperatures ($T_i(0)$, $T_e(0)$) stay at constant value. However, edge parameters such as the neutral pressure (p_{np}), the hydrogen emission (H_α) and the divertor flux (Γ_{div}) continue to increase. These phenomena suggest an increase of recycling in quasi steady state phase. Plasma stored energy (W_p) declines in this phase.

A plot of energy confinement time ($\tau_E^{dia.}/\tau_E^{ISS95}$) that is normalized by the ISS95 scaling [5] respect to the electron density is shown in fig. 4 (a). Neutral pressure increase in proportion to the electron density until electron density reaches 0.8×10^{20} m^{-3}, then the neutral pressure continue to increases in spite of no density rise. At the same time, normalized energy confinement time goes down responding to the increase of the neutral pressure. Fig. 4 (b) shows the normalized energy confinement time respect to the neutral pressure. The normalized energy confinement time monotonically decreases with increase in the neutral pressure. Though it cannot tell that the neutral pressure rise is a cause or a result of the confinement deterioration, it is suggested that the neutral pressure have close connection to the global confinement. In order to make clear the role of neutral pressure, the active pumping at divertor is needed because the wall pumping dominates a pumping characteristic during a discharge,

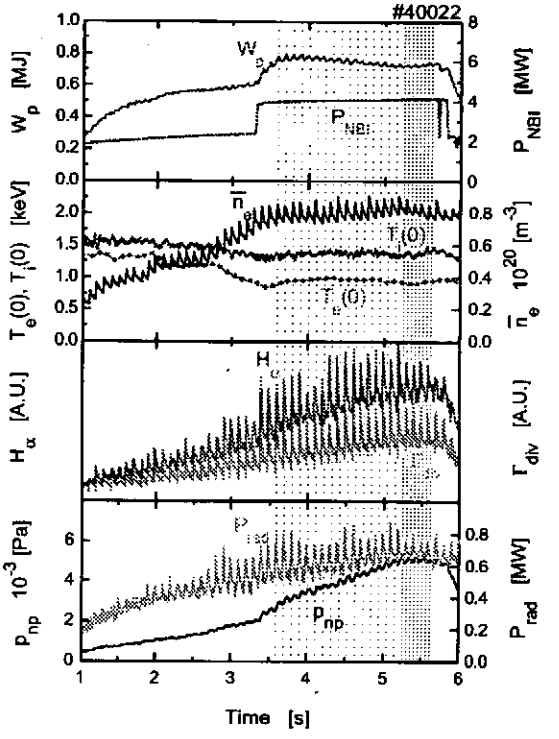

Fig. 3 The temporal evolution of the key parameters in repetitive pellet fueling discharge.

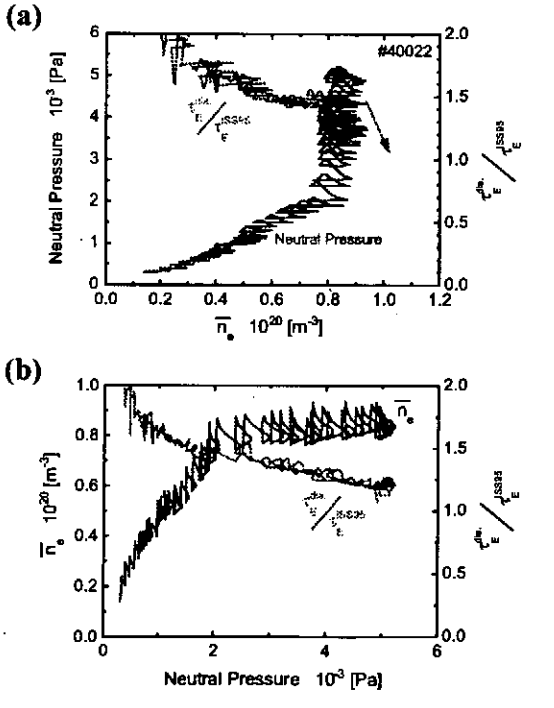

Fig. 4 Change of normalized energy confinement time ($\tau_E^{dia.}/\tau_E^{ISS95}$) respect to (a) electron density and (b) neutral pressure.

namely typical pumping speed of the wall and pumping system are around 10 Pa·m^3 and less than 1 Pa·m^3, respectively.

Fig. 5 shows diagrams of stored energy, which normalized by NBI power, respect to electron density for high density discharges. As for gas puff fueling, a high density discharge around 1.0×10^{20} m^{-3} is also possible by using massive gas puff, but the obvious confinement deterioration is observed at the density of 0.35×10^{20} m^{-3} and above. In the case of the large pellet, favorable confinement is achieved at high density region, though this behavior is transient. In the case of repetitive pellet, though the confinement deterioration is observed at the density of 0.5×10^{20} m^{-3} and above, positive dependence on electron density is kept until 0.8×10^{20} m^{-3}.

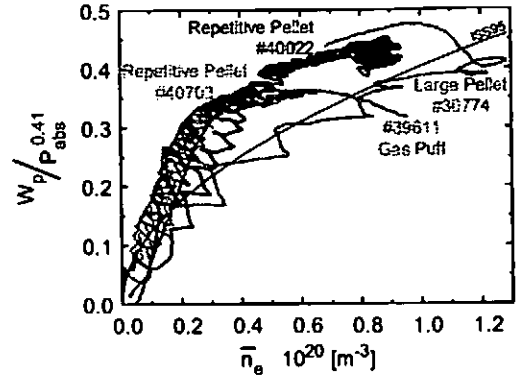

Fig. 5 The diagram of the normalized plasma stored energy respect to electron density.

4. Conclusion

10 Hz repetitive pellet injection for 6 s is successfully performed in LHD. Quasi steady state operation was achieved at plasma parameters of $\bar{n}_e = 0.8\times10^{20}$ m^{-3}, $T_i = 1.3$ keV, $T_e = 1.0$ keV with 4 MW NBI heating. Repetitive pellet fueling shows improved energy confinement compared with massive gas puff fueling at high density region.

However, gradual confinement degradation is observed with keeping high density. In this phase, an increase of recycling particles is observed. It is suggested that the neutral pressure have close connection to the confinement. To achieve long pulse discharges without confinement degradation at high density region, active pumping at divertor in addition to efficient fueling should be needed.

Reference

[1] R. Sakamoto, et al., Nucl. Fusion **41** (2001) 381.

[2] I. Viniar, et al., Instrum. Exp. Tech. **5** (2000) 722.

[3] H. Yamada, et al., Fusion Eng. Des., to be published.

[4] L.R. Baylor, et al., Nucl. Fusion **37** (1997) 445.

[5] U. Stroth, et al., Nucl. Fusion **36** (1996) 1063.

OBSERVATION OF PLASMA RESPONSE AND ION TEMPERATURE INCREASE AFTER IMPURITY PELLET INJECTION IN NBI DICHARGES OF LHD

S.Morita, H.Nozato[1], M.Goto, Y.Takeiri, K.Ikeda, S.Inagaki, O.Kaneko, K.Kawahata, J.Miyazawa, S.Muto, T.Mutoh, K.Nagaoka, Y.Nagayama, Y.Oka, M.Osakabe, B.J.Peterson, S.Sakakibara, R.Sakamoto, K.Tanaka, T.Tokuzawa, K.Tsumori, H.Yamada and LHD Experimental Group

National Institute for Fusion Science, Toki 509-5292, Gifu, Japan
[1]Department of Frontier Science, University of Tokyo, Tokyo 113-0033, Japan

1. Introduction

Many trials on ion heating have been done hitherto in the LHD mainly using NBI and ICRF. Successful ion heating was found in ICRF minority heating (H-minority, He-majority). The ion heating, however, has been still insufficient in H_2 and He NBI discharges [1] because of the high beam energy (E_{NBI}=150-180keV). The NBI absorption power, P_{abs}, is mostly deposited in bulk electrons (P_e/P_{abs}~80%) due to a higher value of E_{NBI}/T_e ratio (~50). Then, the $T_i(0)$ saturates at less than 2.5keV [1].

Recently, neon gas was seeded in order to increase the P_{abs} and to reduce the bulk ion density, n_i, in low-density discharges. As a result, the ratio of P_i/n_i (P_i: direct deposition power from fast ions to bulk ions) could be increased roughly by 5 times in these neon discharges. A $T_i(0)$ of up to 5keV was successfully obtained under a neutral beam injection power, P_{NBI}, of 8 MW and a linear relation was also found between the $T_i(0)$ and P_i/n_i [2,3], although the hydrogen amount could not be sufficiently reduced.

On the other hand, an H_2 ice pellet has been injected to achieve a peaked profile followed by the confinement improvement. However, an apparent temperature increase was not observed, although the operational density range was successfully extended [4]. Thus, a carbon pellet having a much higher melting point was injected as an alternative way to modify the density profile and to increase the P_{abs} at the plasma center using a newly installed impurity pellet injector [5]. In this paper, results on the impurity pellet injection are briefly reported in terms of the ion heating [6].

In the LHD the central ion temperature, $T_i(0)$, has been routinely measured by a crystal spectrometer with a CCD detector observing the Doppler broadening of x-ray lines of He-like TiXXI and ArXVII [7]. No other methods to measure the $T_i(0)$ exist in the present LHD.

2. Plasma Response to impurity pellet injection

Spherical and cylindrical impurity pellets (size: 0.5-1.0mm) of C(Z=6), Al(13), Ti(22) and Mo(42) have been injected into NBI discharges (R_{ax}=3.60m). Typical results are shown in Fig.1. Injected pellet sizes were $1.0mm^{\phi}x1.2mm^{L}$, $0.8mm^{\phi}x0.5mm^{L}$, $0.6mm^{\phi}x0.5mm^{L}$ and $0.4mm^{\phi}x0.4mm^{L}$ for C, Al Ti and Mo, respectively. When $n_e(r)$=const. and $T_e(0)$=2keV are assumed, a density rise (Δn_e) of 2.1, 0.65, 0.54 and $0.42x10^{13}cm^{-3}$ is expected. The results roughly satisfy with the expectation and it means that the injected pellets are fully ablated and confined in the plasma.

The plasma response is clearly different among the 4 elements. In case of the carbon pellet the density quickly goes up and the plasma can be heated up as appeared in the plasma stored energy and central ion temperature behaviors. In case of heavier elements, however, the plasma is immediately cooled down. The Mo pellet injection is the severest case showing the plasma collapse. The $T_e(0)$ drops from 2.7keV to 0.7keV within 100ms after injection. During the temperature decay phase a strong MHD activity, which can induce the plasma collapse, is not observed at present. Then, the temperature drop is mainly triggered by the ionization and radiation losses. The two losses (P_{ionize}, P_{rad}) and maximum ionization stages (q^+) at plasma center are calculated (see Fig.2). In the calculation $T_e(0)$=2keV and $n_e=2x10^{13}cm^{-3}$ is assumed and the size of pellets is fixed in sphere with $0.5mm^{\phi}$ diameter. It is clear that the radiation loss is comparable to the NBI absorption power. When the T_e drops, of course, the P_{rad} becomes larger, and exceeds the P_{abs}. The energy confinement time ($=W_p/P_{abs}$) of the discharge is ~100ms and the decay time of W_p after Mo pellet injection is ~60ms. These similar values also indicate the thermal collapse mainly due to the radiation loss.

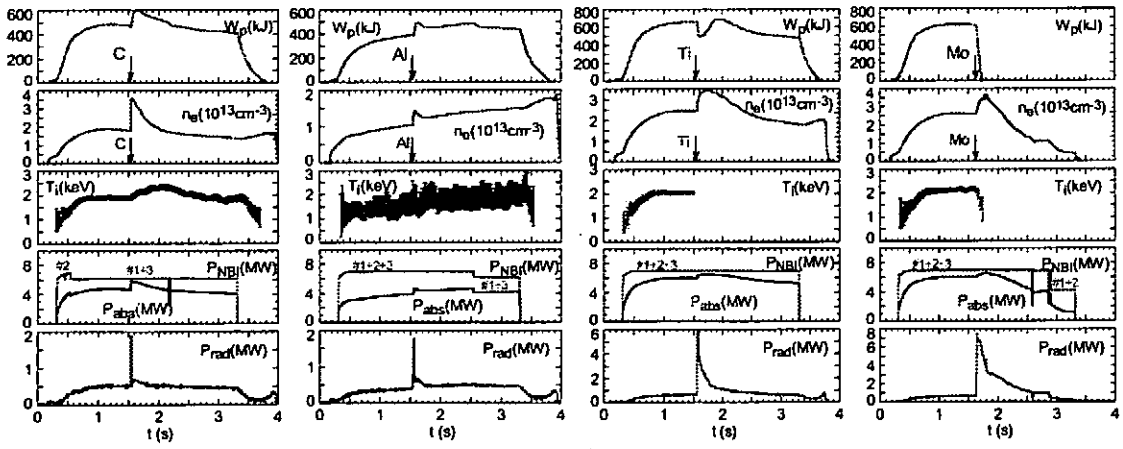

Fig.1 Plasma response to C, Al, Ti and Mo pellets (from left to right). Plasma stored energy (W_p), line-averaged density (n_e), ion temperature ($T_i(0)$), port-through power (P_{NBI}), ionized power (P_{abs}) and total radiation loss (P_{rad}) (from top to bottom).

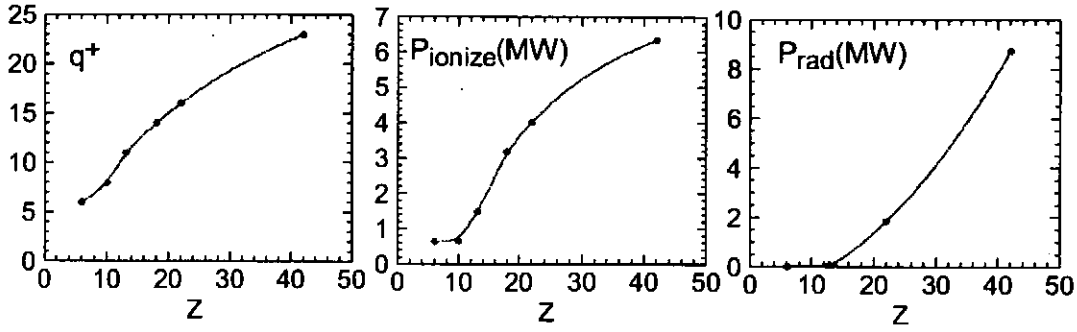

Fig.2 Ionization stage (q^+), Ionization loss (P_{inize}) and radiation loss (P_{rad}) as a function of nuclear charge after impurity pellets are evaporated. The P_{ionize} and P_{rad} is calculated for ablation of spherical pellet with a diameter of 0.5mm$^{\phi}$.

3. Increase of ion temperature after C pellet injection

A typical result for the large pellet (1mm$^{\phi}$x1mm^{L}) injection is shown in Fig.3 (right). The carbon pellet was injected in Ne-seeded discharges. Waveforms of the Ne-seeded NBI discharge without carbon pellet are also traced in Figure 3 (left) for comparison. Both discharges are carried out for the R_{ax}=3.60m configuration. The density of n_e=0.4-0.5x10^{13} cm^{-3} is produced mainly by the puffed neon and recycled hydrogen. A $T_i(0)$ of 3keV is sustained during the Ne-seeded discharge (see Fig.3(a) left). When the carbon pellet is injected, the $T_i(0)$

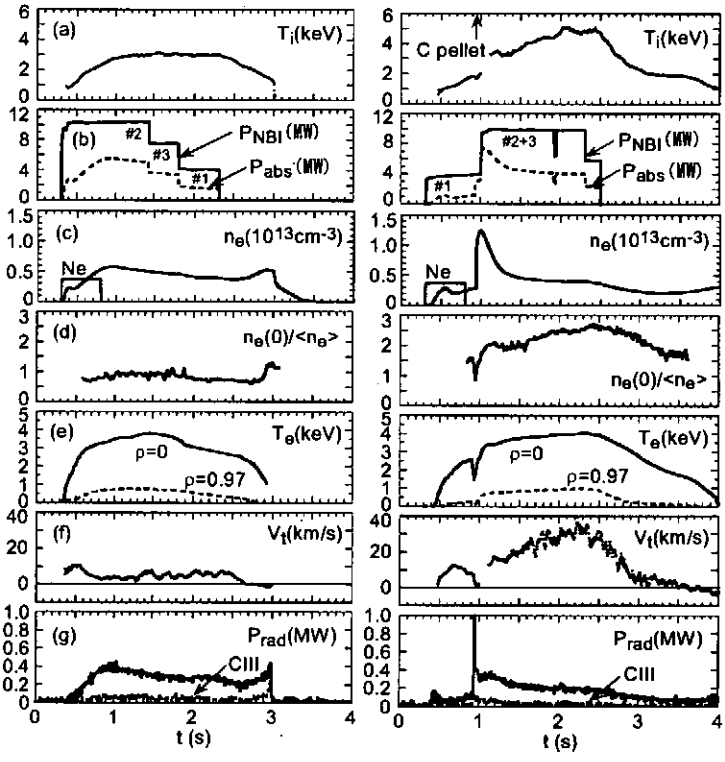

Fig.3 Ne-seeded NBI discharges without (left) and with (right) carbon pellet injection. (a) central ion temperature, (b) NBI power (solid: port-through power, dashed: absorption power), (c) line-averaged electron density (Ne: neon gas puff), (d) density peaking factor ($n_e(0)$: central electron density, $<n_e>$: line-averaged electron density), (e) electron temperature from ECE, (f) central toroidal rotation speed and (g) radiation power (dashed: CIII intensity in arb.

gradually increases and reaches 5keV. The lack of T_i data after the pellet injection is caused by a decrease in ArXVII emission due to the sudden T_e drop.

In low-density discharges, the beam-ion slowing-down time (τ_s) becomes quite long because of the high beam energy (e.g. τ_s>1s for n_e<1x10^{13}cm^{-3}) and the beam-stored energy becomes also very large. Then, the heat flux from the beam ions strongly influences the pellet ablation [8]. The pellet is ablated at outer region of plasmas in low-density range. Therefore, the NBIs #2 and #3 are injected just after the pellet injection in order to avoid ablation at the outer plasma region and to achieve a central particle deposition. This was very effective in increasing the $T_i(0)$. The density profiles are shown in Fig.4. The density peaking factor increases up to ~2.5 after carbon pellet injection, whereas it is around 1 for the Ne-seeded discharge (see Fig.3(e)). The injected carbon ions probably contribute to the formation of the density peaking. From the viewpoint of the experience on this impurity pellet injection, a heavier element is seemed to stay in the plasma core longer time.

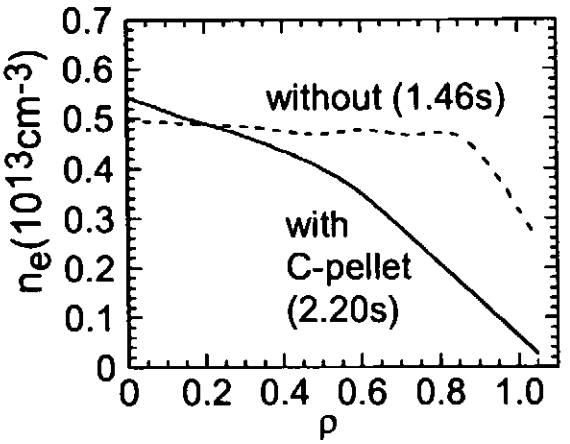

Fig.4 Electron density profiles without (dashed line) and with (solid line) carbon pellet.

Due to the density peaking, the central toroidal rotation speed, V_t, is largely increased and reaches 35km/s, which corresponds to 12% of the carbon ion thermal velocity. The $T_i(0)$ continuously increases, whereas the P_{abs} becomes constant after t=1.5s. Improvement of the ion transport, at least at the plasma center, is expected. The similar $T_i(0)$ increase is also observed for R_{ax}=3.75m configuration having a larger ε_{h_eff}. Ion transport analysis is currently underway, based on the estimation of H, C, and Ne ion densities in both discharges.

References

[1] S.Morita *et al.*, Nucl.Fusion **42**, 1179 (2002).
[2] S.Morita *et al.*, 19th IAEA Fusion Energy Conference, Lyon, 2002, EX/P2-18.
[3] Y.Takeiri *et al.*, Phys.Plasmas **10**, 1788 (2003).
[4] R.Sakamoto *et al.*, Nucl.Fusion **41**, 381 (2001).
[5] H.Nozato *et al.*, Rev.Sci.Instrum. **74**, 2032 (2003).
[6] S.Morita and M.Goto, Rev.Sci.Instrum. **74**, 2375 (2003).
[7] S.Morita et al., to be appeared in Plasma Sci. Nucl. Fusion **79**, No.7 (2003).
[8] S.Morita *et al.*, Nucl.Fusion **42**, 876 (2002).

Dynamics of pellet ablation clouds observed in LHD by a fast-framing tangentially viewing soft X-ray camera

S. Ohdachi[1], K. Toi[1], R. Sakamoto[1], H. Yamada[1], G. Fuchs[2] , S.Yamamoto[3], and LHD experimental Group[1]

[1]*National Institute for Fusion Science, Toki-shi 509-5292, Japan*
[2]*Institut für Plasmaphysik, Forschungszentrum Juelich GmbH, EURATOM Association, D-52425 Juelich, Germany*
[3]*Dep. of Energy Eng. and Science, Nagoya University, Nagoya 464-8603,*

1 Introduction

Hydrogen ice pellet injection is a very promising candidate to fuel large-scale magnetically confined plasmas. In the present scenario of reactor relevant experiments, e.g. ITER, operations with an electron density close to the Greenwald limit are required. Further understanding of pellet–plasma interaction towards improvement of the core fuelling efficiency is needed; to this end the motion of ablated clouds has been extensively studied. E.g., in order to increase the refuelling efficiency, injections from the high field side of the tokamak have been tried in ASDEX upgrade [1]. Due to the drift of the ablated material toward the low magnetic field side, the pellets get deposited deeper into the plasma, thereby significantly improving the fuelling efficiency. In contrast to radial displacements, expansion of ablation clouds along magnetic field lines has not attracted so much attention[2].

In the Large Helical Device(LHD) pellet injection has been successfully used for fuelling as well [3]. By sequential injection of pellets – typically five in sequence – we can reach an operational regime with an electron density in excess of $1 \times 10^{20}\mathrm{m}^{-3}$. Although the pellets do penetrate deeper, the density increase is localized near the edge region. Recently injections from the inboard side (averaged high field side) and from the helical coil side (local high field side) have been carried out on LHD [4]. It turned out, that the outward density re–distribution is thereby reduced, however, the dynamics of the ablated materials could not fully be understood.

Here, we report on movements of the material ablated from the pellet seen by soft X-ray (SX) measurements that do have good space and time resolution. In addition to the standard SX array measurements, a tangentially viewing SX camera[5] has been used (cf., Fig, 1). This camera is based on a pinhole camera. It converts SX images – seen through a tangentially viewing port – into visible ones by use of a phosphor plate and records them with a fast framing video camera. The framing rates are respectively 4.5kHz (full frame) and 13.5kHz (reduced frame width). This speed is sufficient to investigate the structure in space of transient pellet–induced density asymmetries.

2 Experiments

LHD is an Heliotron type device (l = 2 / m = 10) with a major radius R = 3.5 – 3.9 m and an averag minor radius $\overline{a}$ = 0.6 m. A pneumatic pipe–gun type injector is used to refuel the

LHD plasma. Thereby hydrogen ice pellets with a velocity of $\sim$ 1.2 km/s are injected from the outboard side.

The time evolution of plasma parameters following pellet injection (from outboard port) is shown in Fig 2. Expanded graphs of fluctuating SX radiation (SXR) measured at a vertically elongated section (SX3.5) are shown in (B) and (C). Two kinds of oscillations with two different time–scales are found. While the pellet is being ablated, short peaks in the SXR – propagating from the outboard side to the inboard side – can be seen (0.6598 – 0.66 s in Fig.2(C)). After the ablation, slow (f$\sim$ 400 Hz) and damped oscillations are observed in Fig.2(B). From the phase between the inboard line of sight and the outboard one we find a poloidal mode number m = 1. The radial profile of the relative amplitude of the SXR fluctuations together with an estimate of the rotational transform profile is shown in Fig.3. Slower oscillations are localized in the edge region where the rotational transform ι is about unity, whereas fast oscillations peak in the inner region. The maximum fluctuation level is 10% – 20 % for the fast and 5% – 15% for the slow oscillations.

SXR measured at different toroidal positions are shown in Fig.4, where three signals are measured along the sight lines shown in Fig. 1. When the areas observed are connected via magnetic field lines, the oscillations do have the same phase; this suggests that the oscillations are caused by the movement of a perturbed structure that has a small wavenumber along flux tubes. We noted as well, that the correlated oscillations can be observed at the opposite end of the injection port of LHD; then the length of the perturbed region should be at least as long as the circumference of LHD. The fast oscillations are measured as well by the tangentially viewing SX camera. The SXR images from the core region are shown in Fig.5. In the images viewed tangentially, flux tubes in the core region are seen as localized bright spots, this is, because the rotational transform there is small and the lines of the sight are almost parallel to the magnetic field lines. These spots rotate in the electron diamagnetic drift direction.

The results of the two kinds of SXR measurements can be summarized as follows (see Fig.6); several hundred micro seconds after the ablation, one or sometimes several bright regions appear at $\rho \sim 0.5$. This region is elongated along the magnetic field lines. They rotate in the electron diamagnetic drift direction and the radius of the rotating structure does gradually increase. After the disappearance of the above mentioned fast oscillations slower oscillations near $\rho = 0.9$ are observed, they persist for 1 – 10 ms.

3 Discussion

SXR depends on the electron temperature, the electron density and the impurity densities. In Fig.4(A), the peak of fast density fluctuations measured by the FIR interferometer is well correlated to the peaks in SXR. The fluctuation level ($\sim$ 10 %) is consistent with those in SXR ($\sim$ 10 % – 20 %). The fluctuations are therefore caused by the rotation of a flux tube containing a high–density plasma. What we have observed by SXR fluctuations is the motion of the material ablated from the pellet. The increase in the density in the edge might be caused by the outward motion of the perturbation.

In our measurement, beryllium foils with 15 μm (SX array) and 40μm (SX Camera) thick have been used. Since the lower cutoff energy of the X-rays is about 1.3keV and 1.7keV respectively, the electron temperature in the high density tube must reach at least several hun-

dred eV. This high-density region shows up several hundred μs after the injection of a pellet. The heating time is rather short. Assuming that the high density tube were 0.1 m in diameter and 12 m long, which is about half the circumference of LHD, the electron density inside the region is 10^{20} m^{-3} and the electron temperature rises from 1eV to 500eV within 200 μs. The energy needed is about 0.3kJ. Assuming also the electron heat conductivity across the magnetic field $\chi_\perp = 5$ m^2s^{-1}, then it takes about 10ms to heat up the region across the side surface of the cylinder. Parallel heat flux should therefore be important. A heat flux of the order of 30 MJm^{-2} would then be needed.
Slower oscillations are detected neither by the density measurement(Fig.4(B)(d2)) nor by the impurity measurement. The oscillations might be due to those of the electron temperature. Unfortunately – due to the cutoff – ECE measurements are not available after each injected pellet. If the perturbed region is heated mainly by parallel heat flux, an occasionally asymmetry localized on the $t = 1$ rational surface can persist for as long as several milliseconds, since the heat flow parallel to the magnetic field does work only for a finite number of turns on a rational surface. The slowly damping oscillations localized at $\rho \sim 0.9$ might be explained by this.

In summary, the motion of pellet ablated material is studied using SXR measurements. The rotation of the high–density region stretching along magnetic field lines has been observed. A high–density region is moving towards outside. After the high–density region disappeared, slow damped oscillations with a m = 1 mode structure are observed; they are similar to the oscillations sometimes observed in tokamaks under pellet injection.

References

[1] P. T. Lang *et al.*, Phys. Rev. Lett. **79**, 1487 (1997).

[2] S. Milora, W. Houlberg, L. Lengyel, and V. Mertens, Nucl. Fusion **35**, 657 (1995).

[3] R. Sakamoto *et al.*, Nucl. Fusion **41**, 381 (2001).

[4] R. Sakamoto *et al.*, 29th EPS Conference on Plasma Phys. and Contr. Fusion Montreux **26B**, 1074 (2002).

[5] S. Ohdachi *et al.*, Rev. Sci. Instrum **74**, (2003).

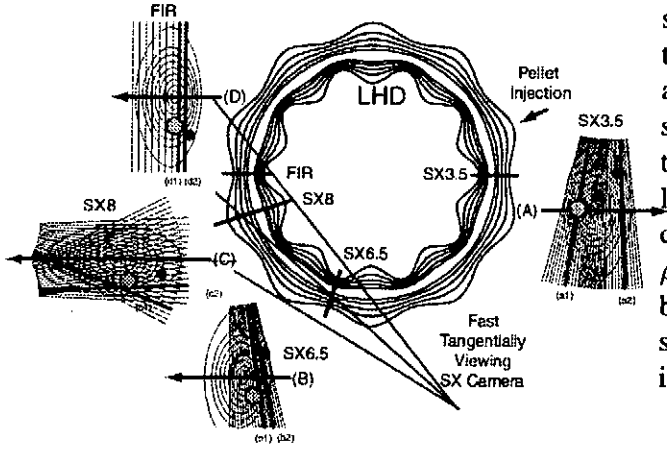

Fig.1: Soft X-ray diagnostics and the flux surface on LHD. The lines of sight and the flux surface at the sections 3.5(A), 6.5(B) 8(C) and 8.5(D) are shown as well. Closed circles and shaded hexagons are drawn to show the areas connected by magnetic field lines. Circles and hexagons are located at $\rho \sim 0.9$, $t \sim 1.0$ and $\rho \sim 0.5$, $t \sim 0.5$, respectively. Labels, (a1), (a2), ... , (d2) mark the sight-lines where the signals shown in Fig.4 have been measured.

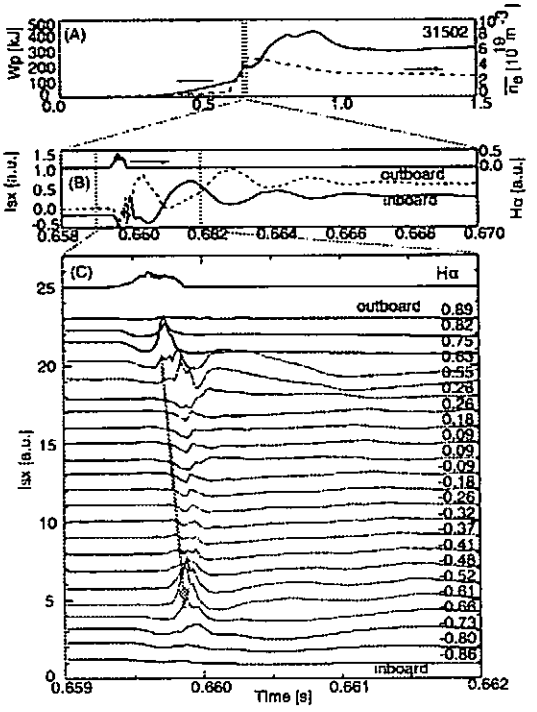

Fig.2: Time evolution of the plasma parameters are shown; the stored energy W_p and the line averaged density $\overline{n_e}$(A), H_α radiation and the SX radiation at inboard/outboard side(B), the SX radiation profile measured at 3.5 port(C). An ice pellet is injected about 0.6595s.

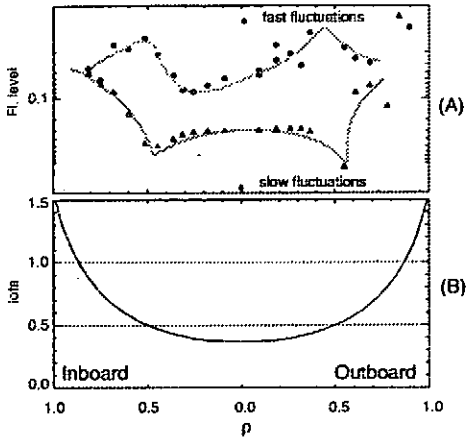

Fig.3: Profile of the fluctuation amplitude(A) measured by SX detector array and the estimated rotational transform profile(B).

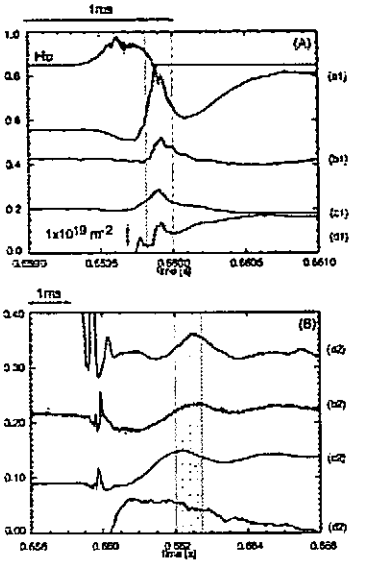

Fig.4: Oscillations at toroidally different positions are shown with faster time scale(A) and slower time scale(B). The labels displayed on the right hand side of the plots correspond to the labels in Fig.1.

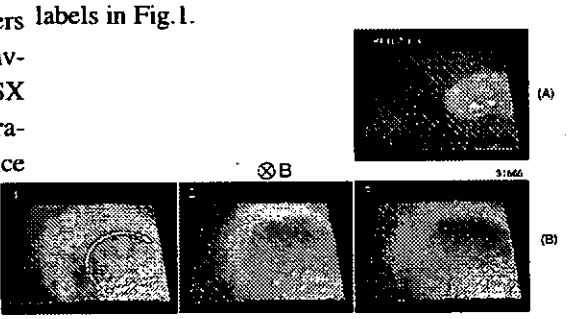

Fig.5: SX image taken by the tangentially viewing SX camera. A simulated image of a flux tube with 10cm in diameter, at the rational surface ι = 1/2 is shown in (A). Sequential images of SXR during the fast fluctuations are shown in (B). The framing rate of the camera was 13.5kHz.

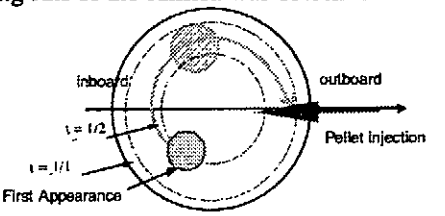

Fig. 6: Schematic diagram of the rotation of the high–density region. It rotates in the electron diamagnetic drift direction and expands outwards. It vanishes near the ι = 1 surface.

30th EPS Conference on Contr. Fusion and Plasma Phys., St. Petersburg, 7-11 July 2003 ECA Vol. 27A, P-3.16

Global and Local Confinement Scaling Laws of NBI-Heated Gas-Puffing Plasmas on LHD

K. Yamazaki, J. Miyazawa, S. Sakakibara, H. Yamada, K. Narihara,
K.Tanaka, M.Osakabe and the LHD Experimental Group
National Institute for Fusion Science, 322-6 Oroshi-cho, Toki, 509-5292 Japan

Abstract

The relation between global confinement scaling laws and local transport characteristics is evaluated on the Large Helical Device (LHD). Previous "new LHD" global scaling laws are revised using the precise plasma edge definition and the recent LHD data of 4th, 5th and 6th experimental campaigns. Strong Gyro-Bohm-like feature of global confinement is reconfirmed. The magnetic field dependence and geometrical scale dependence are stronger than the conventional scaling laws. Using same database of LHD data, the radial profiles of transport coefficients are evaluated, and it is reconfirmed that the local transport in the core is Gyro-Bohm-like, and that near the boundary is strong Gyro-Bohm-like. The global confinement property is consistent with effective transport coefficient near the edge.

1. Introduction

In order to realize high-performance steady-state reactor plasmas, the transport scaling laws should be clarified. Especially, burning plasma performances strongly depend on the local transport as well as global confinement scaling laws. Therefore, it is important to clarify the relation between local and global transport characteristics.

By adding the LHD data of 2nd and 3rd experimental campaigns to medium-sized helical plasma database, several "New LHD" scaling laws have already been derived [1], such as

$$\tau_{NLHD-1} = 0.263 P^{-0.58} \bar{n}_e^{\,0.51} B^{1.01} R^{0.64} a^{2.59} \quad (1)$$

$$\tau_{NLHD-2} = 0.115 P^{-0.64} \bar{n}_e^{\,0.54} B^{0.85} R^{1.02} a^{2.09} \quad (2)$$

Some scaling laws were also derived based on Kadomtsev's dimensional constraints,

$$\tau_{NLHD-D1} = 0.269 P^{-0.59} \bar{n}_e^{\,0.52} B^{1.06} R^{0.64} a^{2.58} \sim B^{-1} \rho_*^{\,-3.61} \nu_{0*}^{\,-0.17} \quad (3)$$

$$\tau_{NLHD-D2} = 0.115 P^{-0.64} \bar{n}_e^{\,0.54} B^{1.03} R^{1.04} a^{2.08} \sim B^{-1} \rho_*^{\,-3.41} \nu_{0*}^{\,-0.08} \beta^{-0.22} \quad (4)$$

Units used here are $P(MW)$, $\bar{n}_e(10^{20} m^{-3})$, $B(T)$, $R(m)$, $a(m)$, respectively. There are well-known four conventional global confinement scaling laws based on medium-sized helical experiments: old LHD scaling (LHD), Gyro-Reduced Bohm scaling (GRB), Lackner-Gotardi scaling (LG) and International Stellarator Scaling 1995(ISS95),

$$\tau_{LHD} = 0.17 P^{-0.58} \bar{n}_e^{\,0.69} B^{0.84} R^{0.75} a^{2} \quad (5)$$

$$\tau_{GRB} = 0.25 P^{-0.6} \bar{n}_e^{\,0.6} B^{0.8} R^{0.6} a^{2.4} \quad (6)$$

$$\tau_{LG} = 0.17 P^{-0.6} \bar{n}_e^{\,0.6} B^{0.8} R a^{2} \iota_{2/3}^{\,0.4} \quad (7)$$

$$\tau_{ISS95} = 0.26 P^{-0.59} \bar{n}_e^{\,0.51} B^{0.83} R^{0.65} a^{2.21} \iota_{2/3}^{\,0.4} \quad (8)$$

The previous "new LHD" scaling laws were compared with these conventional scaling laws, and clarified strong Gyro-Bohm features of LHD plasmas.

In this paper, recent high-heating-power LHD data of 4th, 5th and 6th experimental campaigns will be added to revise new confinement scaling laws.

2. Transport Analysis Code Development

For the precise experimental data analysis on LHD, the 3-D equilibrium reconstruction in the axis, core and edge regions, has been carried out using virtually expanded VMEC edge coordinates [3] in the TOTAL (Toroidal Transport Analysis Linkage) code. This code is

characterized by including the self-consistent equilibrium with experimental data, magnetic multiple-helicity effect and radial electric field effects on neoclassical transport, time-varying NBI deposition profile, bootstrap current effects on equilibrium-transport, and so on. In the analysis of experimental transport coefficient, time-dependent neutral-beam power deposition profile and slowing down calculation are carried out based on experimentally obtained density and temperature profiles.

3. Data Analysis for NBI Discharges

(1) New database

The self-consistent equilibrium has been treated with measured radial profiles by 11-channel FIR laser measurement and 120-channel Thomson scattering electron temperature measurement. The MHD equilibria are calculated iteratively and self-consistently using the "slice and matrix inversion" technique of FIR data, and inner-outer averaging method of plasma pressure.

To clarify the relationship between global and local transport, we used same experimental database to evaluate the both global and local transport based on kinetic pressure. As for the ion temperature profile, we assumed the same temperature profile as electron temperature using central ion temperature value. The global kinetic pressure obtained using this assumption is slightly lower on average than the diamagnetic energy obtained by the magnetic measurement (average ~ 95% and standard derivative ~ 18%, Fig.1).

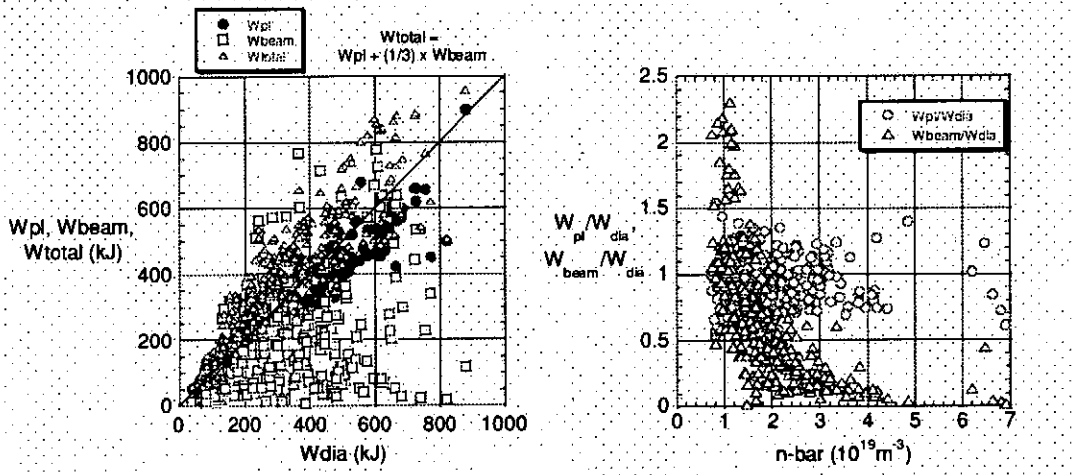

Fig.1 plasma kinetic and beam energies vs. values from diamagnetic measurement (left), and their density dependence (right).

Different from previous works, we used new high-heating-power data (4th, 5th and 6th experimental campaigns) mainly focusing on gas-puffing NBI-heated hydrogen plasmas. The previous database utilized the plasma radius and the volume relevant to vacuum magnetic surfaces. Here the precise semi-empirical evaluation of the zero-pressure plasma boundary using virtual extended VMEC boundary was taken into account [3]. The 98% energy plasma radius a_{98} were used in the confinement scaling laws. The relevant plasma major radius R_{98} was determined by the m=0/n=0 component of the magnetic surface, and the magnetic field strength B_{98} is determined by $B_{98}=R_{vac}B_{vac}/R_{98}$. Almost 300 typical quasi-steady-state shots from 3rd ~5th experimental campaigns were chosen for local and global confinement analysis. The global scaling evaluations using measured diamagnetic energy can be found as same as those using kinetic plasma energy.

(2) Global Transport Analysis

According to the previous "New LHD" scaling laws (see Eqs.(1)~(4)), the magnetic field dependence on confinement is strong comparing with well-known conventional scaling laws. We reconfirm using new kinetic databases that ~ 1.5 times higher confinement time than the ISS95 scaling is obtained (average ~1.53, standard derivative ~0.46) (Fig.2), which corresponds to ~ 2 times of the LHD scaling value (average ~2.10, standard derivative ~0.86).

The "Modified New LHD" confinement scaling laws by the log-linear regression analyses are derived as follows:

$$\tau_{NLHD-1M} = 0.350 P^{-0.59} \bar{n}_e^{0.49} B^{0.95} R^{0.67} a^{2.81}, \quad (R^2 \sim 0.97) \quad (9)$$

$$\tau_{NLHD-2M} = 0.127 P^{-0.60} \bar{n}_e^{0.49} B^{1.00} R^{1.14} a^{2.20}. \quad (R^2 \sim 0.96) \quad (10)$$

The NLHD-1M (Fig.2(b)) is based on experimental data from heliotron-type devices (LHD,ATF,H-E and CHS), and the NLHD-2M based on those from all helical devices including W7-AS, W7-A experimental data set. In this analysis we did not include the effect of magnetic rotational transform.

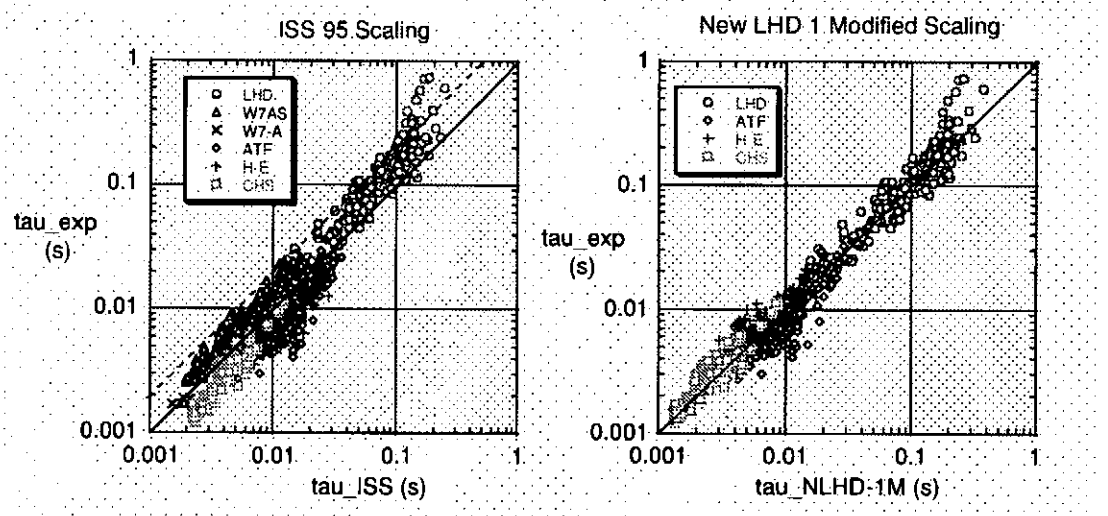

Fig.2 Experimental confinement time vs. the ISS-95 scaling law (left), and "New LHD Modified" scaling laws (Eq.9) (right).

The log-liner regression analysis is also applied to dimensionless values using normalized gyro-radius ρ_*, collisionality ν_{0*} and beta value. Here we used special analysis to keep Kadomtev's constraint:

$$\tau_{NLHD-D1M} = 0.374 P^{-0.60} \bar{n}_e^{0.52} B^{1.15} R^{0.504} a^{2.76} \sim B^{-1} \rho_*^{-3.89} \nu_{0*}^{-0.217} \quad (R^2 \sim 0.98) \quad (11)$$

$$\tau_{NLHD-D2M} = 0.137 P^{-0.58} \bar{n}_e^{0.49} B^{1.11} R^{1.00} a^{2.19} \sim B^{-1} \rho_*^{-3.66} \nu_{0*}^{-0.228} \quad (R^2 \sim 0.98) \quad (12)$$

Again, D1M scaling is based on only heliotron-type devices, and D2M is obtained from all database. These global scaling laws suggested the strong gyro-Bohm like features, which is different from previous conventional scaling laws (Gyo-Bohm like) based on only medium-sized devices (Eqs. (5)~(8)).

(3) Local Transport Analysis

Local transport analysis has been carried out using 120 channel Thomson electron profiles and FIR electron density profiles. Ion density and temperature profiles are assumed to be equal to those of electron. The NBI power deposition is calculated by TOTAL code, and effective thermal diffusivity χ_{eff} is defined including radiation loss as

$$\chi_{eff} = -(Q_{NBI} + Q_{RF} - \frac{dW_p}{dt}) / (n_e \frac{d(T_e + T_i)}{dr}) . \quad (13)$$

Here, we use the following dimensionally normalized scaling:

$$\chi_{eff} / (r^2 B) \sim 10^C \rho^{C_\rho} \nu^{C_\nu} \beta^{C_\beta} . \quad (14)$$

The exponents of each parameter are obtained as a function of normalized minor radius by regression analysis as shown in Fig.3. It is reconfirmed that the radial distribution is Gyro-Bohm in the core and strong Gyro-Bohm near the edge. The global confinement including radiation loss is qualitatively consistent with strong Gyro-Bohm-like local effective transport coefficient near the edge region where the radiation loss should be evaluated.

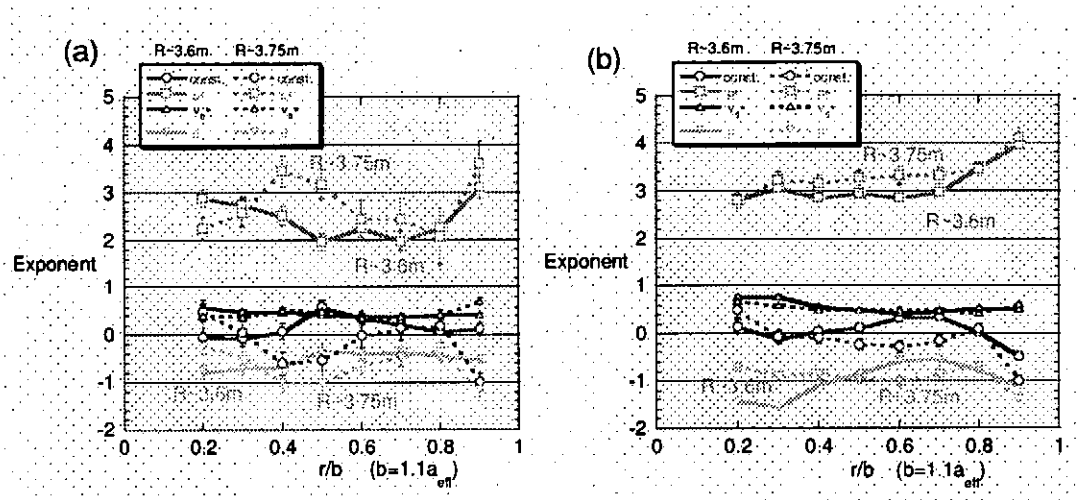

Fig. 3 Exponents of dimensionless $\chi_{eff} / (r^2 B)$ scaling vs. normalized minor radius.

4. Summary

The transport analysis based on recent high-heating-power LHD data (4th, 5th and 6th experimental campaigns) using the definition of the precise plasma radius has been carried out, and came to the following conclusions:

(1) The "New LHD" global confinement scaling laws, previously derived using LHD data (2nd and 3rd experimental campaigns) and medium-sized helical devices, are revised to "New LHD Modified" scaling laws (NLHD-1M (Eq.9) and NLHD-2M (Eq.10)). The strong dependences of magnetic field and geometrical scale factors are reconfirmed.

(2) The dimensional Kadomtev's constraints give rise to the modified scaling laws (NLHD-D1M (Eq.11) and NLHD-D2M (Eq.12)). The global confinement is reconfirmed to be strong Gyro-Bohm-like.

(3) The Radial profiles of normalized transport coefficients are evaluated using normalized gyro-radius, collisionality and beta values. The local transport in the core is weak Gyro-Bohm-like and that near the edge is strong Gyro-Bohm-like.

(4) The global confinement feature is consistent with effective transport coefficient near edge region without considering radiation loss power.

References

[1] K.Yamazaki et al., "Helical Reactor Design Studies Based on New Confinement Scalings" 18th IAEA-Fusion Energy Conference IAEA-CN-77/FTP 2/12 (Sorrento, Italy, 4-10 October 2000)

[2] M. Fujiwara et al., Nucl. Fusion Vol.41 No.10 (2001) 1355-1367.

[3] K.Yamazaki and LHD Experimental Group, "Semi-Empirical Approach to Determine Plasma Boundary of Toroidal Helical Equilibria in LHD", J. Plasma Fusion Res. (to be published)

30th EPS Conference on Contr. Fusion and Plasma Phys., St. Petersburg, 7-11 July 2003 ECA Vol. 27A, P-3.17

Interpretation of a Low-Frequency Alfvén Instability in an NBI Experiment on LHD

Ya. I. Kolesnichenko[1], K. Yamazaki[2], S. Yamamoto[3],V. V. Lutsenko[1],
N. Nakajima[2], Y. Narushima[2], K. Toi[2], Yu. V. Yakovenko[1]

[1] *Institute for Nuclear Research, Prospekt Nauky 47, 03680 Kyiv, Ukraine*

[2] *National Institute for Fusion Science, Oroshi-cho 322-6, Toki, 509-5292, Japan*

[3] *Department of Energy Engineering and Science, Nagoya University, Nagoya, Japan*

I. INTRODUCTION

Alfvén instabilities caused by energetic ions were observed in many experiments on tokamaks. Various Alfvén modes were destabilized also in stellarators [1,2]. Theory predicts that instabilities in stellarator plasmas have a number of peculiarities because, first, there are additional gaps in the Alfvén continuum where specific eigenmodes can reside [3] and, second, there exist "non-axisymmetric" resonances in the wave-particle interaction [4]. However, these peculiarities are relevant mainly to the high-frequency part of the Alfvén spectrum, which is not considered in the present work. In this work, we study Alfvén instabilities with low-frequencies ($50 - 80$ kHz) and low-mode-numbers ($|n| = 1, 2$ and $|m| = 2 - 4$, where m and n are the poloidal and toroidal mode numbers, respectively) observed during Neutral Beam Injection (NBI) in the Large Helical Device (LHD) shot #24512. These instabilities were first reported in Refs. [5,6]. In the mentioned works, a detailed description of the observations was presented, and the Alfvén continua were calculated. It was found that the frequencies of the observed modes correspond to the region of the Toroidicity-induced Alfvén Eigenmode (TAE) gap. On this ground, the instabilities were identified as TAE instabilities. In addition, a guess was made through careful comparison with experimental observations in Compact Helical System (CHS) [1,7] that the observed $|n| = 1$ modes were core-localized even and odd TAEs, whereas the $|n| = 2$ modes were global TAEs, although no eigenmode calculations were carried out. Here, we further study the instabilities: We solve the eigenvalue problem, analyze the mode interaction with the energetic ions, and calculate the growth rates of the instabilities.

II. ANALYSIS OF THE INSTABILITIES

The instabilities in the LHD shot #24512 were driven by hydrogen ions injected tangentially with the particle energy $\mathcal{E}_0 \approx 150\,\mathrm{keV}$ into a helium plasma. The major radius

of the torus in the mentioned experiment was $R_0 = 3.6\,\mathrm{m}$, which was favourable for the confinement of various groups of the particles.

We began our analysis of the observed instabilities with solving the eigenvalue problem with the code BOA [3]. The equilibrium characteristics of the bulk plasma and the energetic ions were obtained with the code described in Refs. [8,9]. We made calculations for both $n = -1$ and $n = -2$ modes observed experimentally. The solutions showing the existence of two TAE modes with $n = -1$ (which we refer to as the $n = 1$ mode) were obtained. However, no discrete modes with $n = -2$ were found in the framework of the used equilibrium and the used equations. The calculated $n = -1$ modes are localized around the radius $r/a \sim 1/3$ and have the dominant modes numbers $m = -2, -3$. Their eigenfrequencies, ω, and the radial structures are shown in Fig. 1. These eigensolutions were obtained for various meshes, the number of points varying from 100 to 500. Therefore, the obtained solutions indeed describe discrete modes. It follows from Fig. 1 that the TAE mode with lower ω consists of harmonics with the same phase (i.e., this is an "even" TAE), whereas the higher mode consists of harmonics with the different phases (an "odd" TAE). Furthermore, the ratio of the frequencies of these modes agrees with experimental data.

The next step in our analysis is a study of the destabilization of the $n = 1$ even and odd TAE modes by the beam ions. Using the resonance condition describing both the conventional resonance and "non-axisymmetric" resonances [4], we have found that the modes are affected by the energetic ions mainly through the conventional (toroidicity-induced) resonance. One could conclude from here that the instability is driven by particles with $|v_\parallel| \approx v_A/3$ ($v_\parallel$ is the ion longitudinal velocity, v_A is the Alfvén velocity), because $v_0 < v_A$ with v_0 the injection velocity. However, this conclusion is wrong: The finite magnitude of the region where the mode is located, Δr_{mode}, provides the interaction between the modes and the particles with $\mathcal{E} \lesssim 150keV$ through the resonance $|v_\parallel| = v_A$, see Fig. 2. We observe that $|v_\parallel| \sim v_0$ at $r/a \sim 0.32$ (a is the plasma radius) for the even mode and $r/a \sim 0.36$ for the odd mode. Because the even mode amplitude is considerable and its radial derivative is large at $r/a \sim 0.32$, one can expect that the finite radial width of the mode will strongly enhance the growth rate, γ, [by a factor of $(3v_0/v_A)^4$ because, roughly speaking, $\gamma \propto v_\parallel^4$]. The enhancement of the growth rate of the odd mode should be much weaker because for this mode both the mode amplitude and its derivative are much less in the region where $|v_\parallel| \sim v_0$. Direct numerical calculations taking into account the mode structure confirmed these conclusion. It was found that $\gamma/\omega \approx 20\beta_b(0)$ ($\beta_b = 8\pi p_b/B_0^2$, p_b is the beam pressure) for the even mode and $\gamma/\omega \approx 2\beta_b(0)$ for the odd mode.

In the calculations we took the beam density distribution in the following two forms:

$n_b(r) \propto (1-r^2/a^2)^2$ and $n_b(r) \propto \exp[-(r-r_0)^2/L_b^2]$ with $L_b = 0.5a$, $r_0 = 0.17a$, $a = 70\,\mathrm{cm}$. Both these expressions resulted in the same growth rate.

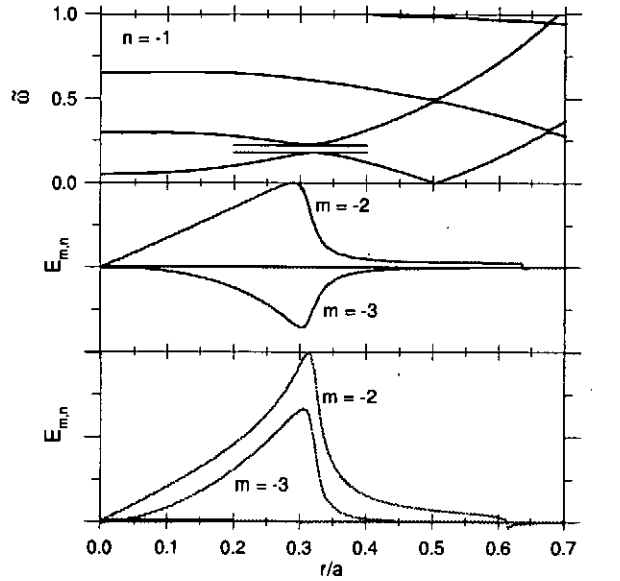

FIG. 1. The calculated even and odd TAE modes in the LHD shot #24512. The ratio of eigenfrequencies is 1.236, which agrees with experimental data.

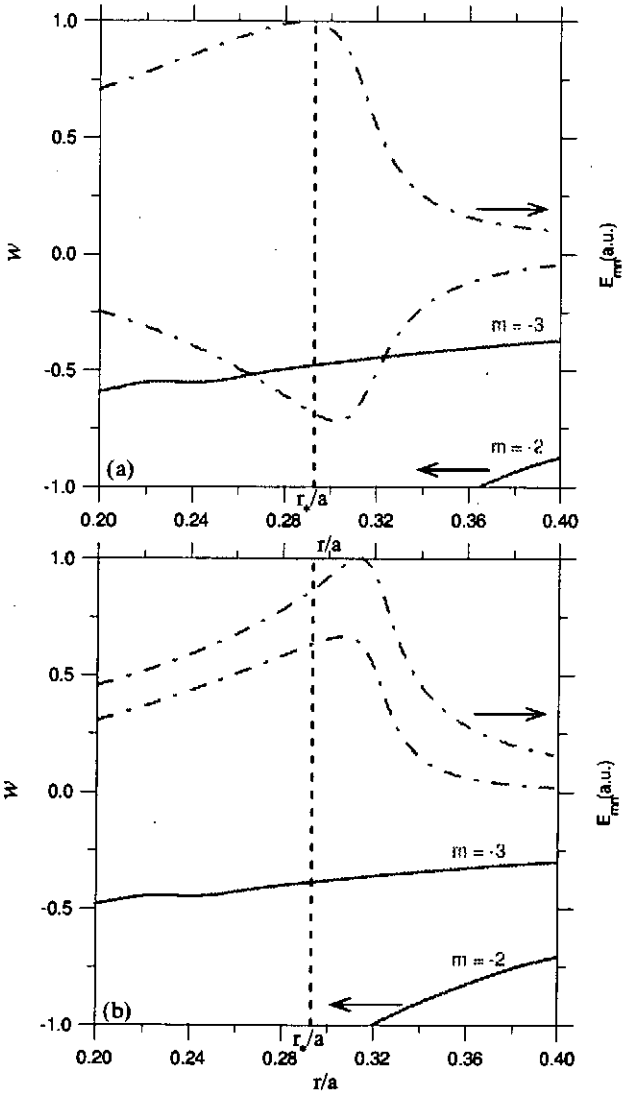

FIG. 2. The normalized resonant velocities ($w \equiv v_\parallel/v_0$) shown by solid lines for the dominant components of the even and odd TAE modes in the LHD shot #24512: (a), the odd mode; (b), the even mode. Dashed-dotted lines show the mode amplitudes. We observe that there are no resonant particles at $r = r_*$ (r_* is a characteristic point where two cylindrical branches of Alfvén continuum intersect), whereas in the lower figure the resonant particles with $|w| \sim 1$ appear at $r/a \approx 0.32$, where the radial derivative of the mode amplitude is large.

III. SUMMARY

The eigenmode calculations carried out with the BOA code [3] showed that there are two discrete $n = 1$ TAE modes, the ratio of their frequencies being 1.2, in agreement with experimental data. The lower calculated mode represents an "even" TAE, and the "upper" mode is an "odd" one, like in tokamaks, which corresponds with a guess made in Ref. [6]. The obtained radial structure of the $n = 1$ TAE modes enabled us to calculate the growth rate of the instabilities driven by energetic ions. It was found that the growth rate of the even mode instability exceeds that of the odd mode by a factor of 10. The enhancement is associated with the finite radial width of the mode, which "switches on" the interaction of the mode and the particles with $\mathcal{E} \lesssim 150\,\mathrm{keV}$.

In addition to the described $n = 1$ mode, an $n = 2$ mode was observed in the same LHD shot. However, we failed to find discrete eigenmodes with $|n| = 2$ in the TAE gap. This may mean that the equilibrium model we used is not sufficiently good at the plasma periphery.

ACKNOWLEDGMENTS

One of the authors (Ya.K.) acknowledges the hospitality of the Institute for Fusion Science, Toki, where he was staying for three months as a visiting professor.

References

[1] K. Toi, M. Takechi, M. Isobe *et al.*, Nucl. Fusion **40**, 1349 (2000).

[2] A. Weller, M. Anton, J. Geiger *et al.*, Phys. Plasmas **8**, 931 (2001).

[3] Ya. I. Kolesnichenko, V. V. Lutsenko, H. Wobig, Yu. V. Yakovenko, O. P. Fesenuyk, Phys. Plasmas **8**, 491 (2001).

[4] Ya. I. Kolesnichenko, V. V. Lutsenko, H. Wobig, Yu. V. Yakovenko, Phys. Plasmas **9**, 517 (2002).

[5] K. Toi, S. Yamamoto, K. Toi, N. Nakajima *et al.*, 19th IAEA Conf. on Fusion Energy, Lyon (2002), Report IAEA-CN-94/EX/S3-2, to be published; Research Report NIFS-758 (2002).

[6] S. Yamamoto, K. Toi, S. Ohdachi *et al.*, "Experimental studies of energetic-ion-driven MHD instabilities and their effects on energetic ion transport in the Large Helical Device plasmas", submitted to Nucl. Fusion.

[7] M. Takechi, K. Toi, S. Takagi et al., Phys. Rev. Lett. **83**, 312 (1999).

[8] K. Yamazaki and T. Amano, Nucl. Fusion **32**, 633 (1992).

[9] K. Yamazaki, N. Nakajima, S. Murakami, M. Yokoyama, and the LHD Group, J. Plasma Fusion Res. SERIES **2**, 125 (1999).

Structures on Electron Temperature Profiles of the Plasmas Confined in the Large Helical Device

K. Narihara, I. Yamada , H.Hayashi, H. Funaba, K. Ida, S. Inagaki, S. Morita, Y. Nagayama, S. Ohdachi, B.J. Peterson, K. Tanaka, K. Toi, J. Miyazawa, T.Morisaki, Y. Narushima, S. Sakakibara, R. Sakamoto, S. Sakakibara, K.Y. Watanabe, K. Yamazaki, H. Idei, K. Kaneko, S. Kubo, Y. Oka, M. Osakabe, T. Shimozuma, Y. Takeiri, K. Tumori, K. Matsuoka, A. Komori and the LHD GROUP

National Institute for Fusion Science, Toki, 509-5292, Japan

We present the structures on the electron temperature profiles of the LHD plasma measured with a 200 channel Thomson scattering system.

1. INTRODUCTION

An electron temperature (T_e) profile of plasma confined in a set of nested magnetic surfaces of a sterallator or a tokamak is an outcome of complex processes such as heat deposition, energy transfer to/from ions and the particle-energy transport etc, however we may draw important information about local defects on the magnetic surfaces and/or change of transport properties. Thus considering, we installed a highly space resolved Thomson scattering system (TS) composed of 200 spatial channels [1] on the large helical device (LHD) [2]. Of 200 channels, ~120 channels cover the whole plasma region along a major radius (R) passing the magnetic axis. Although the finite diameter of the laser beam introduces a small cross talk between the neighboring channels, its level is small enough not to degrade its spatial resolution. Representative structures that we often observe with the TS are flat regions, knees and local sharp bumps. In this paper, we give phenomenological descriptions on these structures and their interpretations if possible.

2. SMOOTH TE PROFILES

The LHD plasma has different T_e profiles depending on the heating method, the intensity of the magnetic field at the axis B_0, the position of the magnetic axis R_{ax}, and electron density n_e. Figs 1 show two examples for ECH and NBI plasmas in LHD. When a discharge is initiated and sustained by ECH focused on the magnetic axis, the T_e profile is a broad cusp. NBI sustained plasmas have triangle shaped Te profiles with different

roundness at the top vertex depending on the R_{ax}, B_0 and n_e. Generally, $T_e(R)$ profiles of LHD plasma seem to be peaked and smooth compared with those of the tokamak [3], indicating that the quality of the vacuum magnetic configuration is preserved in the presence of the plasma. This is probably due to the smallness of plasma currents, which would destroy the magnetic configuration and flatten the T_e profile near the rational surfaces via tearing instabilities. Moreover, the mechanism that 'self-heals' the error field generated island [4] seems to make the T_e profile smooth even in the presence of small error magnetic fields. As easily noticed, the T_e profile preserves a sharp vertex, which is particularly the case for the plasma with the magnetic axis at R_{ax}=3.75 m (the R_{ax}=3.75 m configuration) heated by NBI. This is explained, at least qualitatively, by the fact that the center of NBI is tangent to a circle of 3.75 m in radius, giving the most peaky heat deposition profile for the R_{ax}=3.75 m

configuration. As the R_{ax} changes, T_e profile has more rounded top vertex. All these T_e profiles are smooth and symmetric with respect to the magnetic axis. We examine small deviations from these smooth T_e profiles to find a clue to the understanding the mechanisms leading to the confinement degradation/improvement.

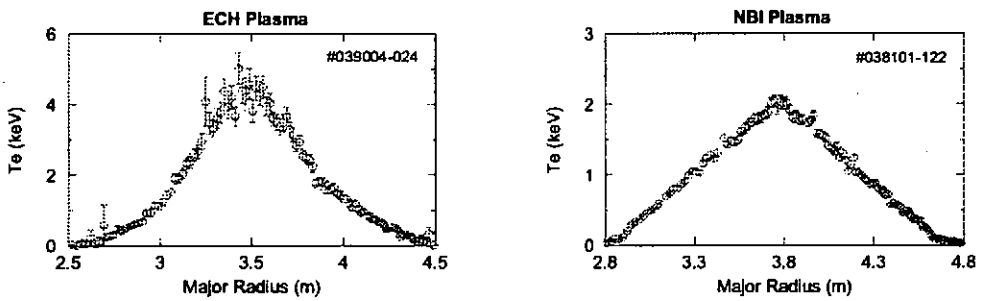

Fig. 1: Typical temperature profiles of ECH and NBI plasmas in LHD.

3. FLAT REGIONS

The most easily notified structures are flat regions at the location where iota~1. We think they are a manifestation of an m/n=1/1 vacuum magnetic island that is observed by applying an electron beam mapping method at the full magnetic field [2]. The cause of the error magnetic field responsible for the island formation is not yet

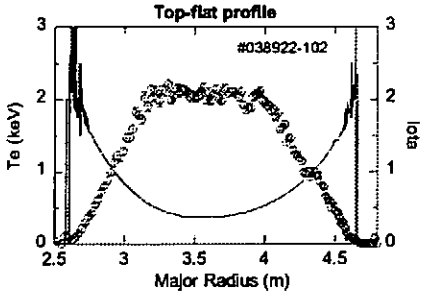

Fig. 2: An example of top-flat T_e profile

clearly identified. In the presence of plasma of high T_e and/or low n_e, the island is often "self-healed" and these flat regions disappear. When the unidentified error field is further increased by the perturbation coils installed on LHD (LID coils), the plasma cannot "self-heal" the island

The central region often becomes flat when NBI is injected in the direction to lower the iota as shown in Fig.2. In this case, the total current exceed 30 kA. Due to this extended iota range, the central magnetic surfaces may become more susceptible to an error magnetic field with many harmonic components that resonate to form magnetic islands, thus leading a flat region.

4. KNEES

A departure from the smooth profiles occurs as knees, an example of which is shown in Fig.3. We may be tempted to consider that the knees are related with a transport barrier [5], because it gives rise to a jump in grad-T_e and therefore in the heat diffusivity χ, provided that the heat deposition is smooth across them. However, this is usually not the case. Examination of many T_e profiles reveals that knees usually appear only on one side of the T_e profile of a triangle shape, indicating that the knee is a deformation of the nested magnetic surfaces, rather than a change of transport properties. We have not yet established a clear correlation with the appearance of knees and the increase or decrease of the diamagnetic energy W_p. Which side a knee appears depends on the magnetic axis position: for the inwards/outwards shifted plasmas, a knee appears on the outer/inner slopes. Very occasionally, we can find T_e profiles with knees with a clear correlation with an increase in W_p.

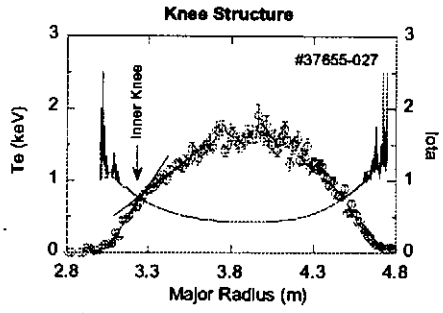

Fig. 3: An example of inner knee structure on a T_e profile.

5. Local Sharp Bumps (ITB)

The central region of T_e profile often shows irregular structures when the U-shaped iota profile is lowered by CCW-NBI or an external error field is added. It seems that, when intense focused ECH is applied at the central region, these structures are highly amplified as sharp bump (ITB) and modified. The appearance of the structure is fairly well

reproducible, though its shape is not. Some of them have been studied as a manifestation of an internal transport barrier (ITB) in the LHD group [6]. Interesting features are: (1) the structures are often asymmetry with respect to the magnetic axis; and (2) they have very large spatial gradients. These structures appear in two different situations. First is the start up phase initiated by ECH. If there is no error field added, T_e profile has a broad cusp shape, while on the other hand if an error field added a narrow bump often appears. Another situation occurs when ECRH is applied to a grown-up plasma sustained by NBI. The necessary conditions for the asymmetric structure to occur are: (1) the focal point of ECRH is close to the magnetic axis; (2) roughly, the ratio between the ECRH power to n_e, P_{ECRH}/ne, is greater than a threshold. (3) NBI is directed so that its driven current lowers the central iota (cnt-NBI). If the condition (3) is otherwise, that is, in co-NBI or balanced-NBI, the T_e profile becomes broad cusp with symmetry with respect to the magnetic axis. The above observations strongly suggest that an "ITB" is highly correlated with the island.

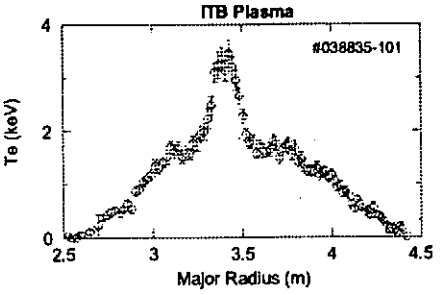

Fig. 4: An example of T_e profile in ITB plasma.

5. SUMMARY

We described three types of structures on T_e profiles of the LHD plasma: flat region, knee and local sharp bump. All of them seem to be related with the iota profile and externally applied error magnetic fields, implying that these structures are related to MHD activities. Although, these structures are limited in space and therefore have only small influence on the global confinement properties, the deep insight of the structures may be an important key for further improvement of plasma performance.

References:

[1] K. Narihara, I.Yamada, K.Yamauchi and H.Hayashi, Rev. Sci. Instrum. **72** ,1122 (2001).

[2] O. Motojima, *et al.*, Phys. Plasmas **6**, 1843 (1999).

[3] M.F.F. Nave *et al.*, Nucl. Fusion **32**, 825 (1992).

[4] K. Narihara, *et al.*, Phys. Rev. Lett. **87**, 135002 (2002).

[5] N. Oyabu, *et al.*, Phys. Plasmas **7**, 1802 (2000).

[6] Y.Takeiri, *et al.*, Physics of Plasma, **10**, 1788 (2003).

Influence of Beam Flow on the Electron Transport in Low Density LHD Discharges

N. Ohyabu, H. Funaba, K. Narihara, I. Yamada, Y. Takeiri, J. Miyazawa, R.Sakamoto, K. Nagaoka, K. Ida, T. Shimozuma, Y. Nagayama, S. Inagaki, T. Morisaki, M. Yokoyama, K. Watanabe, S. Murakami, S. Kubo, Y. Yoshimura, and LHD Experimental Group

National Institute for Fusion Science, Toki, Gifu, 509-5292, Japan

Influence of the beam flow on the electron transport is found to be fairly strong for the low density LHD discharges. In the outer region ($0.4 < \rho < 1$), the shape of the electron temperature profile is independent of the flow direction, but the absolute value is a factor of 1.5-2 higher for co-beam heated discharges. In the core region counter-directed beam flow appears to generates a structure, which enhances the core heat loss (core flattening), but an ITB forms when centrally deposited ECH power exceeds a threshold value.

The Large Helical Device (LHD) is a large heliotron type device with an open helical divertor [1,2]. The focus of the present study is influence of the beam flow on the electron heat transport in the low density ($n < 1.5\times10^{19}m^{-3}$) discharges heated by combination of ECH (electron cyclotron resonance) and NBI (neutral beam injection). Inward shifted configuration is used (R_{ax} = 3.5-3.53m, B (magnetic field) = 2.85 T). The maximum ECH power used in this experiment is 1.5 MW and its power deposition is localized near the center (ρ (normalized radius) < 0.15). In such a low density operation, a significant fraction of the NBI injected beams (150 keV) pass through plasma and are lost and thus the power deposition profile to the bulk plasma is fairly broad. Beam flows drives Ohkawa current which modifies the rotational transport ($\iota/2\pi$) profile particularly in the core. (Sign convention of the current is that positive (negative) current increases (decreases) the rotational transform). This additional rotational transform depends on the current profile. Here we assume parabolic current profile to calculate the $\iota/2\pi$ profile. For positive current of ~25 kA, the $\iota/2\pi$ =1/2 surface disappears from the plasma region. In the gas fuelled, NBI heated LHD discharges (R_{ax} = 3.5-3.6m), the shape of the electron temperature profile is fairly insensitive to variation in density and power. It is close to parabolic profile if plotted in terms of ρ (normalized radius), i.e., $T_e(r) = T_e(0)[1-(\rho/1.05)^2]$.

In the low density ($n < 1.5\times10^{19}m^{-3}$) ctr-beam heated discharges, however, core flattening of the profile occurs, deviating significantly from the parabolic profile as shown in Fig.1(a). Flattening is localized in the core region within the $\iota/2\pi$=1/2 surface.

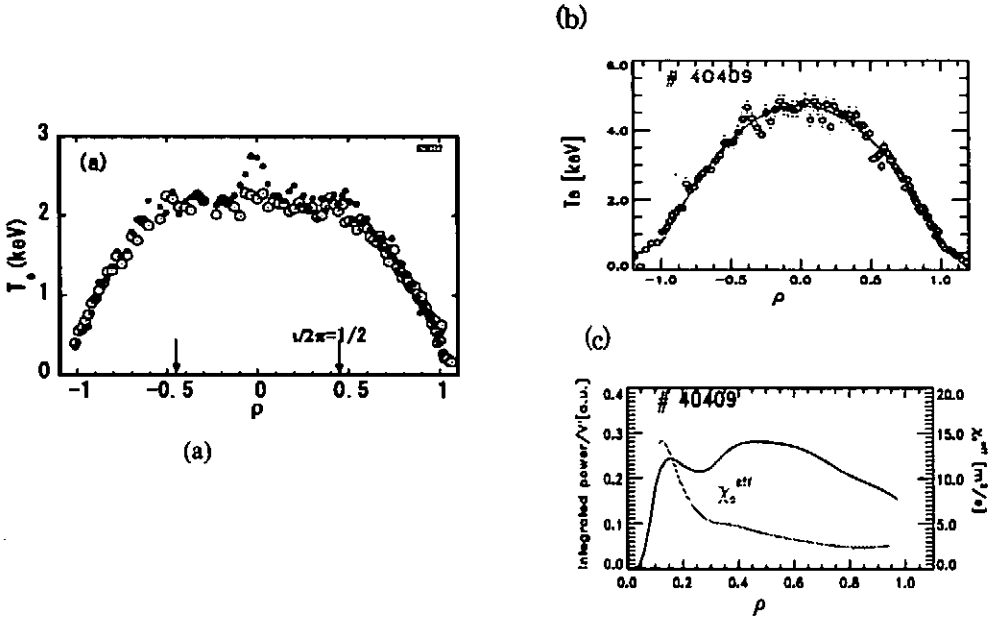

Fig. 1 (a) Electron temperature profiles ($n = 1.35 \times 10^{19} m^{-3}$) (o) with core flattening (P_{ECH}=0.0MW, $P_{NBI(ctr)}$ = 3.6MW),(•)with bump(P_{ECH}=0.3MW, $P_{NBI(ctr)}$=3.6MW), (b) Temperature profile in the co-beam heating dominated discharge. (6MW) (c) transport analysis of the above discharge

A part of reason for the flattening is that a smaller fraction of power is deposited in the core region compared with the co-beam heated discharges. When ECH power of 200 KW with power deposition localized in the core is added, the core temperature increases slightly, but the core flattening still persists. This means that flattening can not be explained simply by difference in the power deposition profile alone since ECH contribution to the power flux dominates over that of the beam in the core region. Thus it is difficult to explain the observed flattening (high thermal diffusivity > $50 m^2 s^{-1}$) without invoking some structural cause. With higher ECH power, a small bump starts to appear in the center as shown in Fig.1 (a). With further higher ECH power, ITB (core region with high ∇T) [3-6] grows rapidly. The power threshold for ITB formation increases with n. The radial location of the ITB foot defined as the location of the discontinuity of ∇T (typically around $\rho = 0.2$) increases slightly with P/n, but it is well within the $\iota/2\pi = 1/2$ surface.

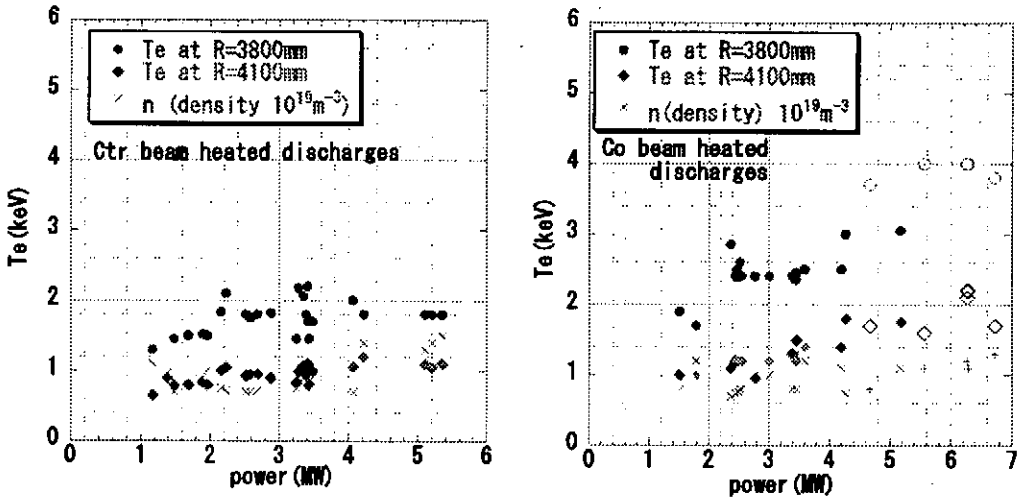

Fig.2 Electron temperatures at R=3800mm (ρ=0.5) and at R=4100mm (ρ=0.8) are plotted as a function of input power for Ctr beam heated and Co beam heated discharges (Rax=3.5m configuration). Neon doped discharges are indicated by (o ◊).

Core heat transport in the low density co-beam heated discharges is quite different from that of ctr-beam case. Core flattening does not occur. With added ECH power, the central temperature increases continuously and a much wider ITB forms with foot location at $\rho = 0.5$. The discontinuity in ∇T at the foot point is much smaller compared with the ctr-beam case, but the central temperature is comparable. In the outer region beyond the foot point, the profile remains unchanged. With higher co beam power, core profile flattening occurs ($0 < \rho < 0.3$). But temperature in the whole region increases and the mild jump in ∇T at $\rho \sim 0.5$ disappear, as seen in Fig. 1(b).

The present LHD data show that the profile shape ($\nabla T/T$) in the core region ($0 < \rho < 0.4$) varies, exhibiting core flattening and ITB. However, we have not observed any significant change in the profile shape in the outer region ($0.5 < \rho < 1$), an important region in determining the global energy confinement. In Fig. 2, Te ($\rho = 0.5$) and Te ($\rho = 0.8$) are plotted as a function of input power for co and ctr beam heating dominated discharges. In these scans, the line average densities are not fixed well, but around ($n \sim 1.0 \times 10^{19} m^{-3}$). The ratios of these temperatures are nearly constant (~2), independent of the power and beam direction. In the ctr-beam heated discharges, temperatures saturates with power fairly severely. In the co-beam heated discharges, temperature increases reasonably well with input power and its profile is a factor of 1.5-2 times

higher than that in the ctr case. This distinct difference is not due to iota change, caused by the beam driven plasma current. We found that the electron temperature profile is nearly independent of the plasma current. The observed burst of magnetic fluctuations shown in Fig. 3 may be responsible for it. With increasing ctr beam power, amplitude of magnetic fluctuations and frequency of the burst increase, accompanying a small drop of the temperature during the burst. ITB formation also becomes more difficult. The frequency of the modes is around 50 kHz and the mode numbers are m=1, 2 and n=1. They are also substantially lower for co-beam heating case.

The electron transport analysis is shown in Fig. 1(c). In this discharge, the density is low enough to separate the electron and ion heat transports because the electron–ion thermalization power is negligible compared with input powers transferred to electrons or ions. In our high energy negative ion NBI system, a half of the power is lost by shinethrough at $n=1.0\times10^{19}m^{-3}$ and Neon gas is added into the plasma to reduce shinethrough loss and hence increase the input power to electrons. The electron thermal diffusivity decreases monotonously with increasing ρ, quite different profile compared with tokamak case. It is a factor of 2 lower than that of the ctr-beam discharges. We, however, can not exclude a possibility that a direct effect of Neon impurity on the electron transport may cause the enhancement of the electron transport.

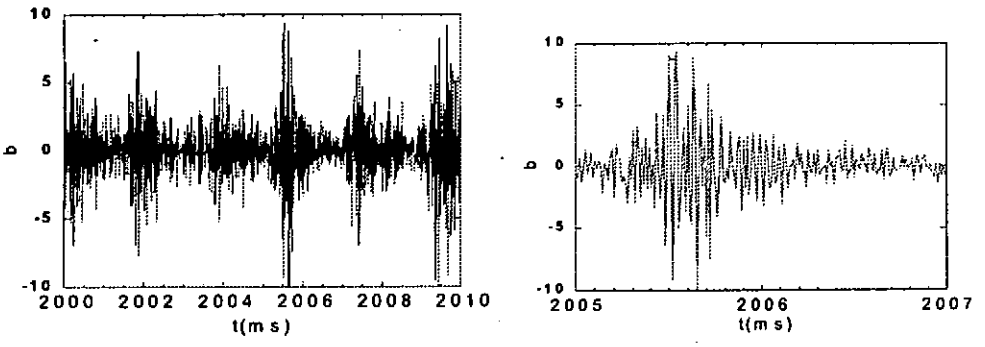

Fig. 3 Burst of the magnetic fluctuations, which appear during the ctr beam heated discharges. The amplitude and frequency of the burst increases with injected ctr beam power.

References

[1] A. Iiyoshi *et al., Nucl. Fusion* 39, 1245 (1999).
[2] O. Motojima et al., to be published in Nucl. Fusion (2003).
[3] T.Fujita et al., Phys. Rev. Lett. 78, 2377 (1997).
[4] A. Fujisawa et al., Phys. Rev. Lett. 82, 2669 (1999).
[5] Shimozuma et al. 12th Joint Workshop on ECE and ECRH, paper No.056 (2002).
[6] Takeiri et al., Physics of Plasma, 10, 1788 (2003).

Edge Density Profile Measurements on LHD with a Lithium Beam Probe

T.Morisaki, K.Tanaka, K.Narihara, S.Masuzaki, S.Morita, N.Ohyabu, A.Komori, O.Motojima and LHD Experimental Group

National Institute for Fusion Science, Toki 509-5292 JAPAN

1. Introduction

In the edge region of the Large Helical Device (LHD), the magnetic field shows the complicated ergodic structure, which is quite different from that in tokamaks [1]. Such a thick ergodic layer is surrounding the last closed flux surface (LCFS), therefore the position of which is quite unclear. Actually the electron temperature and density profiles just outside the LCFS are high and no clear change of its gradient is seen, which suggests the ergodic layer to have enough capability for confinement properties. By measuring the electron density and temperature profiles in detail, effect of the magnetic field ergodicity on the edge transport can be investigated. In the previous study the effective electron heat conductivity χ_e was extracted and its behavior was compared quantitatively with the magnetic field ergodicity [2].

In this paper electron density profiles measured with a 20keV lithium beam probe (LiBP) are presented and the relationship between the edge particle transport and the magnetic structure is discussed. Utilizing the LiBP the electron density can be measured precisely as far as the inside of the LCFS with a good spatial resolution.

2. Experimental apparatus and conditions

The LHD is the largest super conducting heliotron device of which poloidal/toroidal period numbers are 2/10, major radius and averaged minor radius are 3.9 and 0.6m, respectively [3]. Experiments were carried out mainly with electron cyclotron heating (ECH) plasmas with a toroidal magnetic field B_t of ~1.5T. The magnetic axis position R_{ax} was set from 3.45-3.90m. The averaged electron density and the central temperature were 0.2-2x$10^{19}$$m^{-3}$ and 1-3keV, respectively.

Edge density profiles were measured with a lithium beam probe (LiBP) [4]. The LiBP consists of a beam injector and an optical detector. The lithium ions are extracted from a thermionic emitter of aluminosilicate called β-eucryptite with the energy of 20keV, then neutralized in the lithium vapor. The neutral beam is injected to the LHD plasma

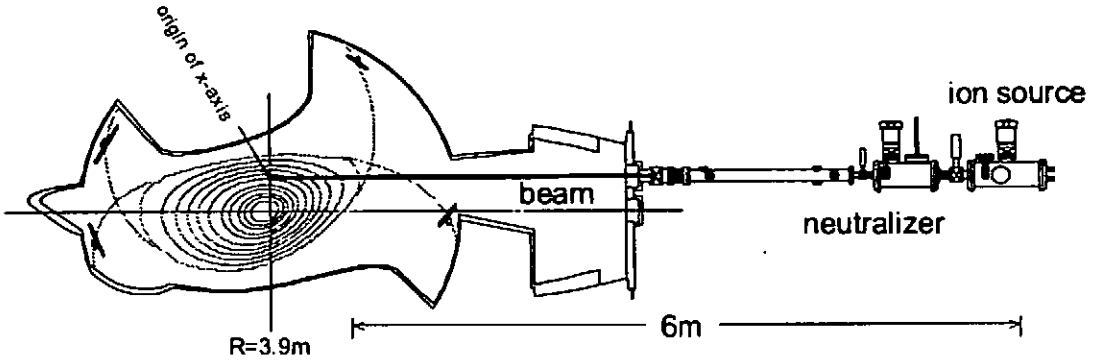

Fig.1. Vertical cross section of the experimental setup. The beam is injected to the plasma 0.3m above the equatorial plane and at an angle of 4 degree to the radial direction.

horizontally from the outboard side of the torus, as shown in Fig.1. Emissions from the beam are detected with a CCD camera. Electron density profiles are reconstructed along the beam as $n_e(x)$. The origin of the x-axis is defined to be the point where the beam (x-axis) encounters the R=3.90m plane. The time and spatial resolutions of the system are 17ms and 2cm, respectively.

The line averaged electron density at the plasma center was measured with an interferometer. The Thomson scattering system was utilized for edge electron temperature measurements.

3. Experimental results and discussion

Controlling the vertical field strength, the plasma column, i.e., the magnetic axis position R_{ax} can be shifted in LHD. This modification to the magnetic surfaces affects not only the particle orbit or the MHD properties but also the ergodic layer in the edge region. In the outward or inward shifted configuration from the standard one (R_{ax}=3.60m), the thickness and the ergodicity of the ergodic layer become large.

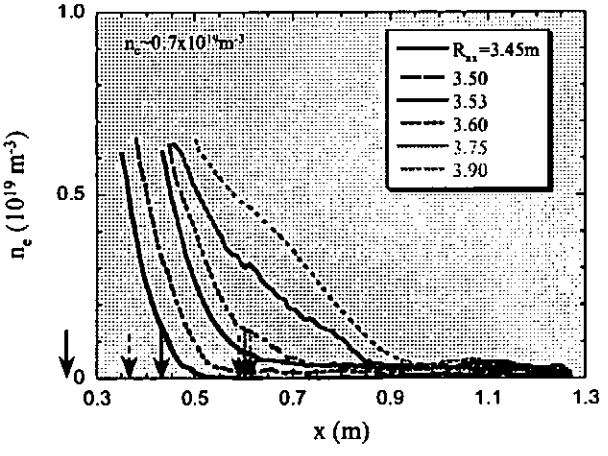

Fig.2. Density profiles measured with LiBP in various R_{ax} configurations. Arrows correspond to each LCFS position.

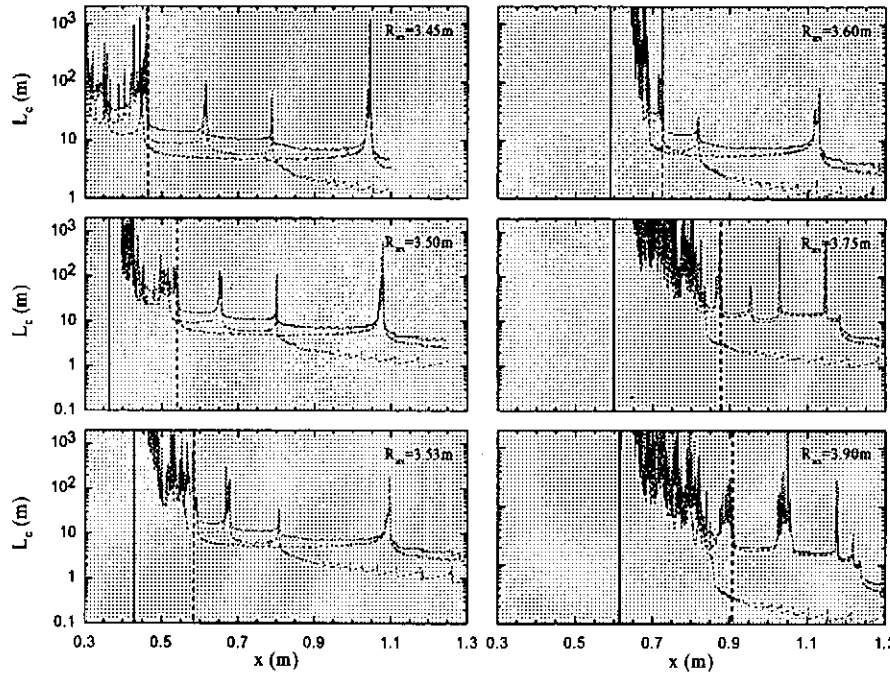

Fig.3. Connection length L_c profiles for various R_{ax} configurations, which are the field line lengths from the starting points on the x-axis to the wall. Black and blue lines represent the direction of the field line tracing, i.e., clockwise and counterclockwise, respectively. The red line is the sum of both directions, i.e., effective L_c from the wall to wall through the starting point on the x-axis.

Figure 2 shows the electron density profiles $n_e(x)$ measured with the LiBP with the same line averaged density of ~$0.7\times10^{19}m^{-3}$. Clear shift of $n_e(x)$ is seen. Although we can see a foot point in $n_e(x)$ where n_e begins to rise and its gradient becomes steep, no change in profiles is seen at the LCFS. The similar characteristic has been observed in T_e profiles [2]. In order to find the information about the foot point, the edge magnetic structures were analyzed precisely. Figure 3 shows the connection length L_c profiles for various R_{ax} configurations. It can be seen that there are many 'whisker' structures outsides the closed region. Although the region between the whiskers has short L_c, relatively high density can be sustained there if the radial diffusion is large enough. In other words, if the distance between adjacent whiskers $\Delta_{whisker}$ is shorter than the SOL width Δ_{SOL}, $n_e(x)$ between them is embedded. Using the simple SOL model, Δ_{SOL} was calculated to be about 4-5cm under the assumptions of the edge temperature T_e ~ 50eV and diffusion coefficient D~1. Measuring $\Delta_{whisker}$ from the outboard side in the L_c profile, the 'innermost whisker' which satisfies $\Delta_{whisker} < \Delta_{SOL}$ can be determined, which should be at the boundary of the continuous $n_e(x)$,

i.e., at the foot point. In Fig.3, the dashed line represents the position of the innermost whisker. Referring Figs.2 and 3, it is found that $n_e(x)$ foot points correspond to the innermost whisker positions in various R_{ax} configurations. It has also been confirmed that the foot point does not change its position during the density scan.

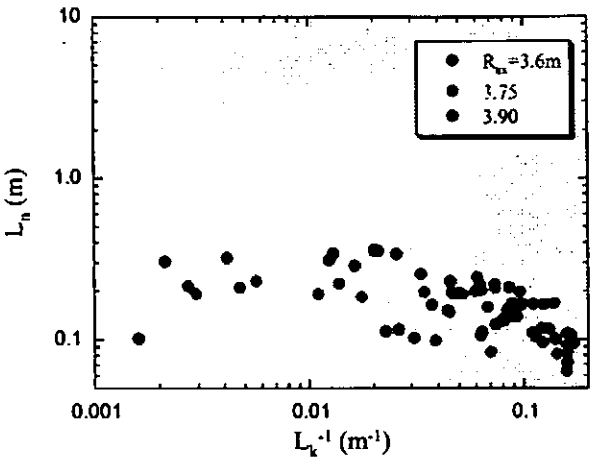

Fig.4. Dependence of density scale length L_n on inverse Kolmogorov length L_K^{-1}.

To clarify the effect of the magnetic structure on edge transport, the relationship between the magnetic ergodicity L_K^{-1} and the density scale length L_n, was investigated, where L_K^{-1} is the inverse Kolmogorov length. The L_n is known to reflect the diffusion coefficient D. The L_K^{-1} was calculated in the vacuum configuration. In Fig.4, little dependence of L_n on L_K^{-1} is seen, although the effective electron heat conductivity χ_e shows the threshold property, i.e., it increases rapidly in the region where L_K^{-1} ~0.2-0.4m^{-1} [2]. It seems that the magnetic ergodicity does not affect the edge particle transport so much. However, in the very low density discharges, flattening in the $n_e(x)$ at the ergodic region is often observed.

Further experiments and calculations are required to get the comprehensive understanding about edge transport.

4. Summary

The magnetic ergodicity does not affect the edge particle transport so much, except for the low density discharges. The $n_e(x)$ foot positions are determined by the innermost whisker position.

References

[1] N. Ohyabu et al., Nucl. Fusion **34** (1994) 387.

[2] T. Morisaki et al., J. Nucl. Mater.**313-316** (2003) 548.

[3] O. Motojima et al., Phys. Plasmas **6** (1999) 1843.

[4] T. Morisaki et al., Rev. Sci. Instrum. **74** (2003) 1865.

Sawtooth Oscillation in Current Carrying Helical Plasma in LHD

Y. Nagayama, K. Kawahata, S. Inagaki, S. Sakakibara, K. Tanaka,

T. Tokuzawa, K. Y. Watanabe, and LHD experimental group

National Institute for Fusion Science, 322-6 Oroshi, Toki 509-5292, Japan

1. INTRODUCTION

Sawtooth oscillation is a series of periodic crashes, which is commonly observed magneto-hydro-dynamic (MHD) activity in tokamak plasmas. The mechanism of sawtooth oscillation has been discussed for a long time. Traditionally, a full reconnection process causes the fast parallel transport phenomena along the field line. However, experimental data are not consistent with the full reconnection model, but support the idea that the reconnection occurs at a localized place causes the sawtooth crash in tokamaks [1-3]. The driving instability and the reconnection are key physics to understand the sawtooth oscillation. In helical systems, the kink, the tearing and the ballooning modes should be stable, since the plasma current is very low and the shear is high. Nevertheless, sawtooth oscillation has been observed in helical plasmas [4]. So sawtooth oscillations in a helical

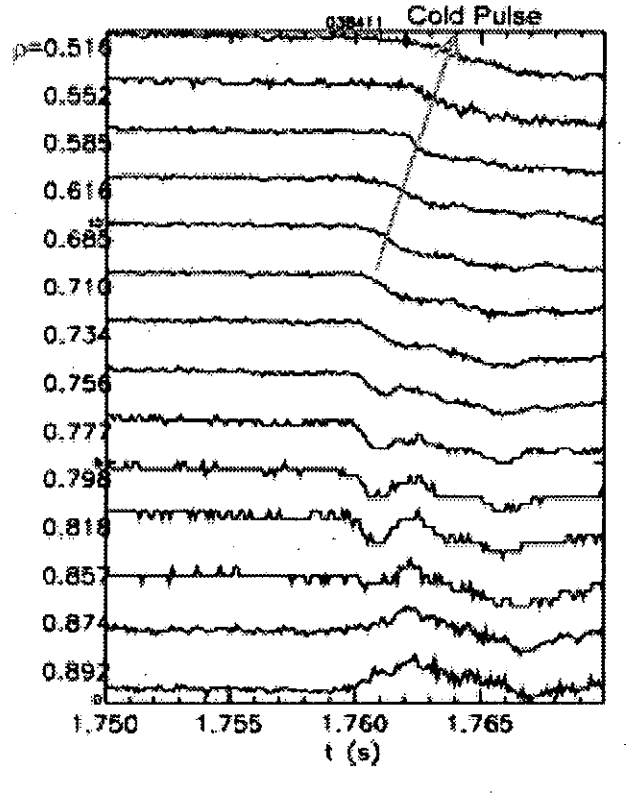

Fig.1 ECE signals during the sawtooth crash.

system should provide new information to MHD physics.

This paper will present the research of the sawtooth oscillation in the current carrying helical plasma using the electron cyclotron emission (ECE) diagnostics [5,6] in the Large Helical Device (LHD): the world largest superconducting heliotron-type fusion device with the averaged minor radius: a=0.65 m, the major radius of the plasma axis R_{ax}=3.6 m. The plasma current is driven by the neutral beam injection (NBI), and the direction (co- or counter-) of the toroidal current can be controlled. Here, the co-current is defined as the current that increases the central iota.

2. SAWTOOTH OSCILATION IN LHD

Figure 1 shows time evolution of the electron temperature (T_e) in the plasma with the sawtooth oscillation and with the co-current. The T_e profile is measured with the 32 channel radiometer [6], and the radiometer data is cross-calibrated to the Michelson interferometer [5]. The plasma has B_{ax}=2.8 T and R_{ax}=3.6 m, and it is heated by the co-beam with the deposited power of 6.2 MW.

Interestingly, no precursor oscillation has been observed in the ECE signals or in the Mirnov signals in the case of annular sawtooth crash. In the Mirnov signal, a steady mode with the frequency of ~7 KHz

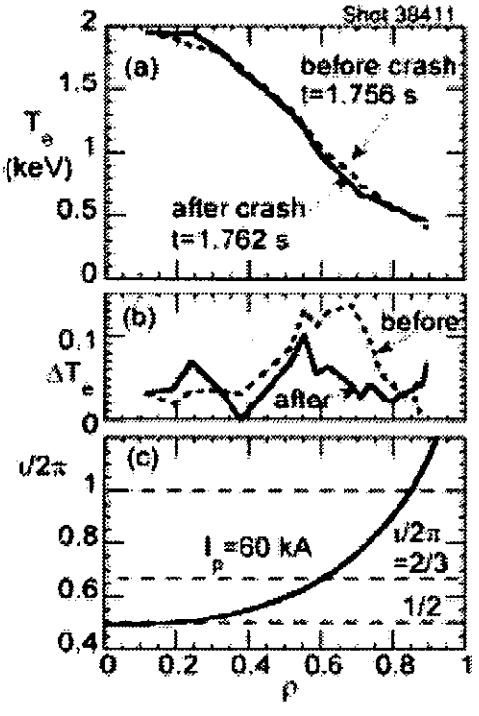

Fig. 2 (a) T_e profile and (b) ΔT_e profile before (solid line) and after (dotted line) the sawtooth crash. (c) Calculated iota profile in the case of I_p=60 kA using VMEC code.

is observed before the crash. Although Mirnov signal is enhanced during the crash, the frequency and the mode number do not change. The mode numbers are (m, n)~(4, 5). Here, m and n are the poloidal and the toroidal mode numbers, respectively. So, the plasma rotates steadily with the frequency of ~1.4 kHz. This is high enough to observe a low n mode during the crash, which takes 2 msec. So, a localized mode, which is hardly observed, may cause the crash.

The ECE at ρ=0.73 drops and the ECE at ρ=0.89 increases at t=1.76 sec. As shown in Fig. 2, the normalized inversion radius is about ρ=0.85, where the $\iota/2\pi$ is nearly 1. The ECE in the region between ρ=0.7 and ρ=0.85 drops, and the ECE in the region of $\rho > 0.85$ increases at t=1.76 sec. This is an annular crash. The decrease of the ECE in the region of $\rho < 0.7$ delays as the ECE position departs from the inversion radius. So the cold pulse propagates in the inward direction.

The iota profiles considering the plasma current are shown in Fig. 2(c). This is calculated using the 3-D equilibrium code VMEC [7] under the assumption of a parabolic current profile. A speculation on the role of co-current is as follows: The co-current reduces the radius of the $\iota/2\pi$=1 surface so that the pressure gradient at the rational surface

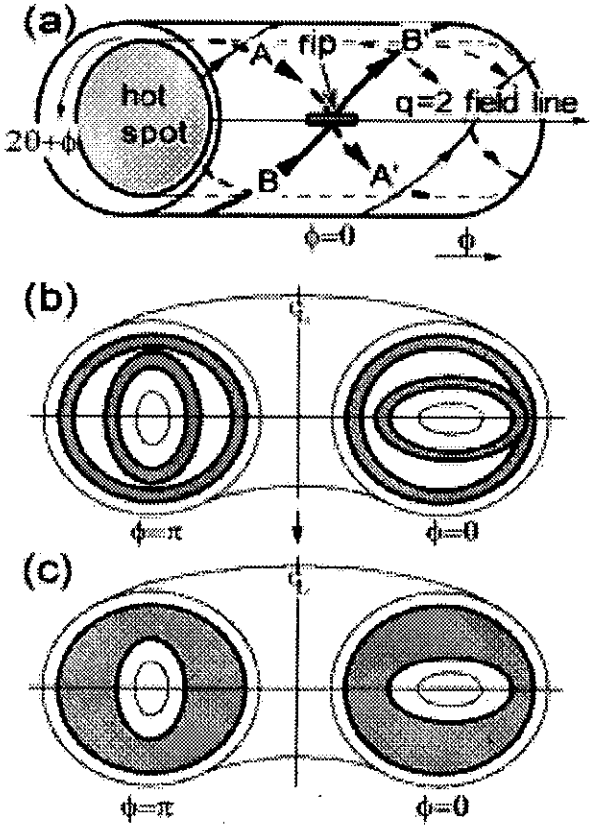

Fig. 3 Localized reconnection model for m=2 mode. (a) The reconnection of field lines (A-A') and (B-B') at the 'rip'. (b) Flux surfaces before the crash. (c) Flux surfaces after the crash.

increases. Finally a pressure driven mode becomes unstable and it drives a reconnection due to some resistivity.

3. LOCALIZED RECONNECTION MODEL

Observations of the inward cold pulse propagation in the case of annular crash indicates that rapid mixture of the plasma in the limited region, in another word the reconnection, is caused in LHD. Figure 3 shows a schematic picture how an annular crash takes place due to the localized reconnection [2]. Suppose that the hot spot that is made of the inner flux surfaces, is slightly apart from the outer surface, and is touched only one localized position named 'rip', and that a field line A-A' belongs to the hot spot and a field line B-B' to outer surface. When they merge at the rip, new field lines A-B' and B-B' are produced due to the reconnection. Since one field line nests one flux surface if not rational, parallel heat flow along the reconnected field lines mixes the inner and outer flux surfaces. The rip can be made by a localized mode, such as the ballooning mode [3]. This process continues until the localized mode terminates, and it makes a ring shaped iso-thermal area. So, the localized reconnection process could cause the annular crash.

References

[1] Y. Nagayama, et al., Phys. Plasmas **3**, 1647 (1996).

[2] Y. Nagayama, et al., J. Plasma Fusion Res. **73**, 712 (1997).

[3] Y. Nishimura, J. D. Callen, and C. C. Hegna, Phys. Plasmas **6**, 4685 (1999).

[4] Y. Nagayama, et al., Phys. Rev. Letters **90**, 205001 (2003).

[5] Y. Nagayama, et al., J. Plasma Fusion Res. **79**, 601 (2003).

[6] K. Kawahata, et al., Rev. Sci. Instrum. . **74**, 1449 (2003).

[7] S.P. Hirshman, D.K. Lee, Comput. Phys. Comm. **39**, 143 (1986).

30th EPS Conference on Contr. Fusion and Plasma Phys., St. Petersburg, 7-11 July 2003 ECA Vol. 27A, P-3.22

Spatial Resolved High-Energy Particle Diagnostic System using Time-of-Flight Neutral Particle Analyzer in Large Helical Device

T.Ozaki, P.Goncharov, S.Murakami[1], T.Amano, T.Saida[2], S.Sudo, I.Yamada and LHD Experimental Group

National Institute for Fusion Science, Toki, Gifu 509-5292, Japan
[1] Department of Nuclear Engineering, Kyoto University, Kyoto, Japan
[2] Tohoku Universities, Sendai, Japan

I. Introduction

High-energy particle measurement is important for an ion temperature monitor, the study of the high-energy particle confinement, the clarification of the electric field formation mechanism and particle transport research. Especially, in the helical system like Large Helical Device (LHD), there are various particle orbits, not only transit particle orbit but also the trapped particle orbit due to the complicated magnetic configuration. These orbits create new electric field and the electric field produces new particle orbits. In addition, there are three different heating systems in LHD, neutral particle injection heating (NBI), ion cyclotron resonance frequency heating (ICH) and electron cyclotron resonance frequency heating (ECH). They produce high-energy particles with different energy ranges and pitch angles. The neutral particle measurement system with the spatial scannable mechanism is indispensable to study the high-energy particle confinement. Therefore 2-dimensional scanning system using the time-of-flight neutral particle analyzer (NPA) has been prepared on the horizontal port in LHD.

The vertical scan system has been available from the middle of the 6th cycle in addition to horizontal scanning system. The detail explanation of the vertical scan will be described in section III. Various experiments, for example, the ion temperature profile at the single shot, the neutral particle flux distribution on the poloidal direction, the optimization of the ion temperature measurement by combination with the horizontal scan and the different pitch angle measurement at the same average radius, can be expected by the vertical scanning.

Here we will summarize the typical results obtained by the horizontal scanning of the NPA, and describe the preliminary results obtained from the newly installed vertical scannable NPA system, especially the ion temperature profile.

II. The Results from Horizontal Scan

The horizontal scan of NPA has been performed by carrying out the remotely motor drive of the NPA stage. A scanning speed is 0.17 degree per second. A scanning center pitch angle, which is defined as the angle between the magnetic axis and the sight line, is from 40 degrees to 100 degrees. [1]

The high-energy neutral particle spectrum during NBI discharge has been measured by scanning of the NPA shot by shot. The transit particle can be mainly observed at the tangential position of NPA, although the trapped particle can be observed at the vertical position. The high-energy particle was confined in LHD plasma without large loss mechanism because the experimental result has been agreed with the simulation result. [2] Comparison between the co- and the counter injection of NBI has been studied. The experiments have been performed on two different long discharges with the normal and reverse magnetic fields. The NPA scan has been continuously proceeded during the long discharge to obtain the accurate dependence on the pitch angle. The higher energy particle can be confined in co-injection case than the counter-injection case. [3]

The horizontal scan experiment has been performed in ICH plasma too. The result is that the spatial distribution of the neutral particle flux had the butterfly shape predicted theoretically. [3,4] The ripple loss can be observed about at 5 keV, especially in low magnetic field and the outer magnetic axis configuration. The pitch angle dependence of the ripple loss was not clear. In the ECH experiments, the disappearance of the ripple loss can be observed by the radial electric field produced by the strong ECH. [5]

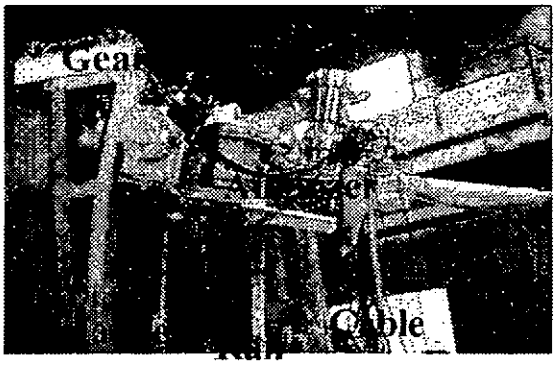

Fig.1. The phtograph of NPA system. The stainless balancer compensates the weight of the analyzer. High speed scan of 1 degree per second can be achieved.

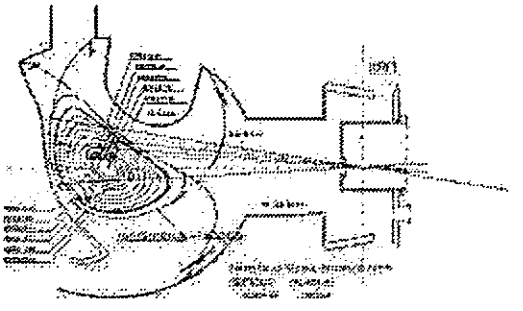

Fig. 2. Plasma section at the vertical scan. To avoid the observation at the diverter region, the horizontal position with the center pitch angle of 60 degrees is chosen.

III. Vertical scanning system

The vertical scanning system is realized by adding a movable mechanism to a current horizontal scanning system (Fig. 1). The analyzer slides along three stainless steel rails, which are arcs of the radii of 4 m. One of rails defines the accurate position of the analyzer. Another rail, which is settled at the front of the rail, fixes the vertical position and the other rail, which is settled at the side, fixes the side position. Therefore, the smooth and non-vibrated vertical driving can be obtained. The two chains and the gears, which are connected with the motor, hang up the analyzer. Two stainless blocks are set on the opposite side of the chain in order to balance the weight (700kg) of the analyzer and reduce the load for the motor. Therefore very high speed of one degree per second can be obtained. To avoid the tilting of the bellow at the pivot point, there are two different bellows for the horizontal and for the vertical scans. Both scannings are performed by the remote control with a personal computer. While acting as the monitor of the position with a CCD camera, the time history of an exact position is read using the position detector, and stored in the personal computer.

VI. Ion temperature profile

The time history of an ion temperature profile can be obtained by changing the vertical position shot by shot. The plasma poloidal section is varied by changing the toroidal position. We choose the horizontal position of the center pitch angle of 60 degrees to avoid the observation at the diverter region where there is much background neutral. (Fig.

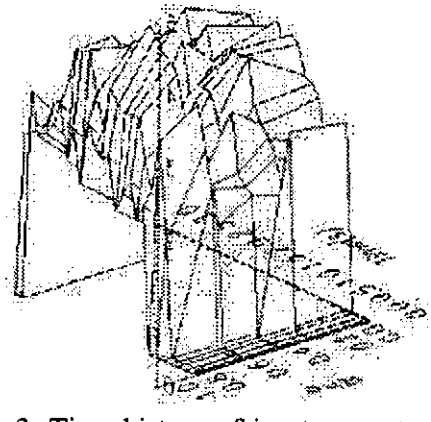

Fig. 3. Time history of ion temperature profile.
The ion temperature profile can be obtained by changing the vertical position shot by shot.

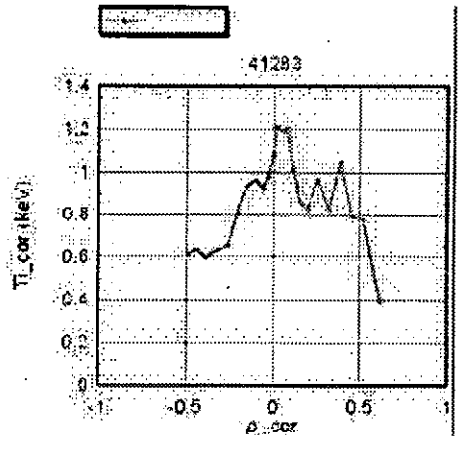

Fig.4 Ion temperature profile.
The ion temperature profile can be obtained by vertical scaning the analyzer during a single long discharge.

2) The time history of the ion temperature profile is shown in Fig. 3. The ion temperature profile is comparatively flat and a central temperature is low observed as compared with other measurement. Since the main component of this plasma is the argon, the contribution of the charge exchange between lower ionized argon and proton should be considered. The lower ionized argon exists near the plasma outer region. Therefore the observed ion temperature may be affected by the contribution of the neutral flux contribution at the outer region rather than at the portion of the smallest plasma radius of the sight. In calculation, these cross sections are too small, the contribution for the neutral flux. Neutral particle scattering with high-Z plasma may be one reason of the profile flattening.

It is possible to obtain the poloidal profile of the neutral particle flux or the ion temperature profile by vertical scanning the analyzer during the single long discharge. Fig. 4 shows the typical ion temperature profile by vertical scanning the analyzer from +9 to -9 degrees with the scanning speed of 1 degree per second during 40-second discharge. Time change corresponds to an observation position. Horizontal measurement positions are at the central pitch angles of 60 degrees. The fluctuation of the ion temperature at $\rho=0-0.5$ may reflect the charge exchange neutral from the dense background neutral at the diverter region.

V. Summary

The 2-dimentional scanning neutral particle measurement system has been completed in order to investigate the high-energy particle confinement. In the horizontal scan, the difference between co- and counter injection of NBI, the heating mechanism of ICH and the ripple loss can be observed. By adding the vertical scan, the ion temperature profile can be obtained as the preliminary experimental result.

References

[1] T.Ozaki, V.Zanza, *et al.*, Rev.of Sci. Instrum., 71 (7), (2000) 2698-2703.

[2] T.Ozaki, S.Sudo, *et al.*, Plasma Phys.and Fus. Res. SERIES, 3, (2000) 444-448.

[3] K.Saito, *et al.*, Plasma Physics and Controlled Fusion, 44 (2002) 103-119.

[4] T.Ozaki, P.Goncharov, *et al.*, Proc.of 29th EPS, P-4.065. (2002)

[5] T.Ozaki, S.Murakami, *et al.*, Rev. of Sci. Instrum., 74 (3), (2000) 1878-1882.

[6] T.Notake, *et al.*, IAEA-TM (2003) (to be submitted)

Suprathermal Proton Distribution Function Measurements with a Multidirectional Charge Exchange Diagnostic on LHD

P.R.Goncharov[1], T.Ozaki[1], J.F.Lyon[2], S.Sudo[1], S.Murakami[3] and LHD Experimental Group[1]

1) National Institute for Fusion Science, Toki, Gifu 509-5292, Japan
2) Oak Ridge National Laboratory, Oak Ridge, TN 37831-8072, USA
3) Kyoto University, Kyoto, 606-8501, Japan

The multidirectional passive neutral particle analyzer described in [1, 2] has been applied to investigate the behaviour of anisotropic distributions of suprathermal particles in LHD plasma. Temporally and angularly resolved measurements of $f(v, \theta, t)$ have been made in experiments with tangential hydrogen neutral beam injection into hydrogen and noble gas target plasmas on LHD. A simplified kinetic model employed for the data interpretation is based on the Fokker-Planck equation with Landau-Trubnikov collision operator. It assumes a Maxwellian background plasma in a uniform magnetic field and does not take into account either radial electric field effects or the spatial inhomogeneity. Two groups of experimental observations are discussed: those that can be interpreted in terms of this Coulomb collisional model as the effects of the frictional drag force and the diffusion tensor and the influence of the magnetic configuration on the fast ion distribution.

The time development of the energetic distribution tails in NBI-heated plasma has been measured. Fig. 1 shows the experimentally observed time evolution of the energetic particle distribution from tangential 150 keV H NBI in He target plasma $n_e = 0.5\times10^{13}$ cm^{-3} measured along a nearly tangential sight line directed towards NBI, i.e. at smaller θ.

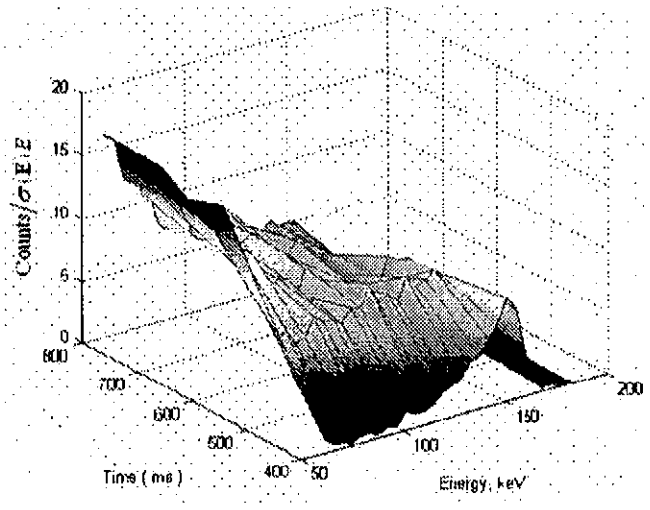

Fig. 1. Experimental tangential NBI - produced proton distribution time development.

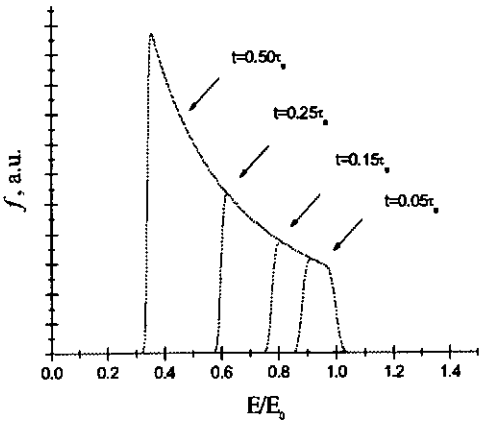

Fig. 2. Analytic calculation of the fast ion distribution function time evolution.

Experimental H^+/He^+ charge exchange cross-section data [3] was used for σE-correction of neutral particle spectra. The slowing down time scale is consistent with the Coulomb collisional slowing down time τ_s and the evolution of the spectrum can be seen from a peaked one to an equilibrium slowing down distribution. The value 400 ms on the time axis corresponds to 100 ms after the commencement of the NBI pulse. Such a time evolution governed by the slowing down term, i.e. the frictional drag in the Fokker-Planck equation, is illustrated in Fig. 2. A delta-like NBI source function $S(v-v_0)=\frac{S_0}{4\pi v^2}\frac{1}{\epsilon\sqrt{\pi}}e^{\frac{(v-v_0)^2}{\epsilon^2}}$ was assumed in calculations, where S_0 is the source rate and the value ϵ determines the source function width; it is assumed that $\epsilon \ll v_0$.

The influence of the target plasma Z_{eff} on the intensity of the pitch angle scattering of NBI-produced fast ions has been studied. A substantial enhancement of the pitch angle scattering of fast ions from tangential NBI has been observed for plasmas with higher Z ion species in comparison with hydrogen plasma. The asymptotic behaviour of H^+/Ne^{k+} and H^+/Ar^{l+} charge exchange cross-sections at high energies discussed e.g. in the monograph [4] was used for σE-correction of measured neutral particle spectra.

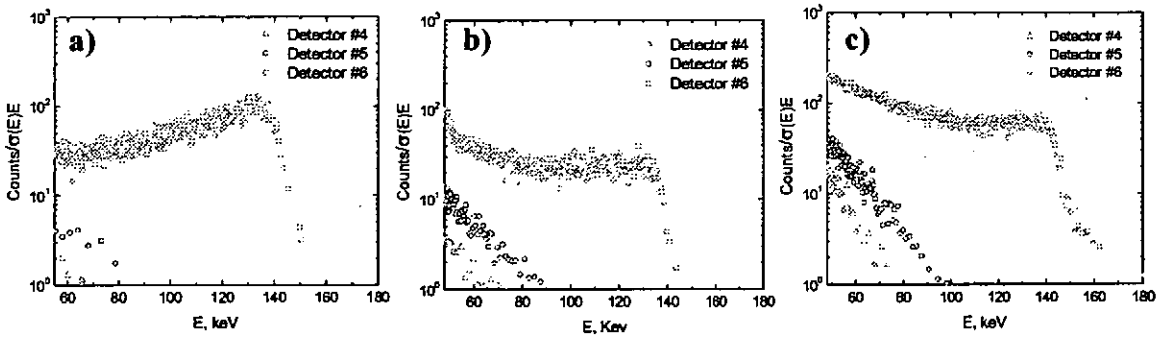

Fig. 2. Proton energy distributions f(E, θ) along three directions from H, Ne and Ar/He target plasmas.

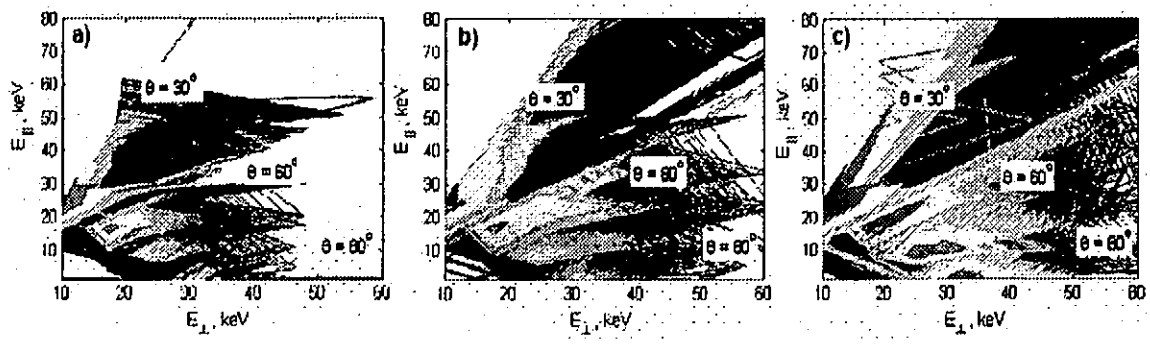

Fig. 3. Contour plots of the proton energy distributions $f(E_\perp, E_\parallel)$ from H, Ne and Ar/He target plasmas.

The energetic proton distributions from $n_e = 0.4\times10^{13}$ cm^{-3} target plasmas for three viewing directions shown in Fig. 2 a) are from 131 keV H NBI into H (Z = 1); in Fig. 2 b) – from 132 keV H NBI into Ne (Z = 10) and in Fig. 2 c) – from 135 keV H NBI into Ar (Z = 18) / He (Z = 2). Fig. 3 shows the contour plots of H^+ energy and pitch angle distributions in the axes $E_\perp, E_\parallel$ for these three target plasma ion compositions correspondingly. The sectorial gaps are due to the fact that the measurements are made along several discrete directions. A detailed description of the diagnostic viewing geometry is given in [1].

It can be seen that the angular diffusion of energetic protons is very sensitive to the background plasma ion composition in similar discharges. The interpretation is that the Legendre operator describing the angular spread on the right hand side of the Fokker-Planck equation contains the ion contribution proportional to Z_{eff}. The value of the effective charge $Z_{eff} = \frac{1}{n_e}\sum_i Z_i^2 n_i$ strongly depends on the ion species.

On the spectra of NBI - produced energetic particles measured tangentially noticeable tails above the injection energy E_0 have been observed. This effect is attributed to the velocity diffusion described by another term originating from the diffusion tensor. It should be noted that the finite width ϵ of the NBI source function leads to a certain tail above E_0 even if the diffusion tensor effects are neglected. However, NBI is assumed to be highly monoenergetic and the observed tails definitely cannot be attributed solely to ϵ. Fig. 4 shows the experimental distributions of energetic particles from tangential 145 keV H NBI in He target plasma $n_e = 0.5\times10^{13}$ cm^{-3} and also from the same NBI combined with ICH. It has been observed that the application of additional ICH leads to a certain expansion of the distribution tail above E_0.

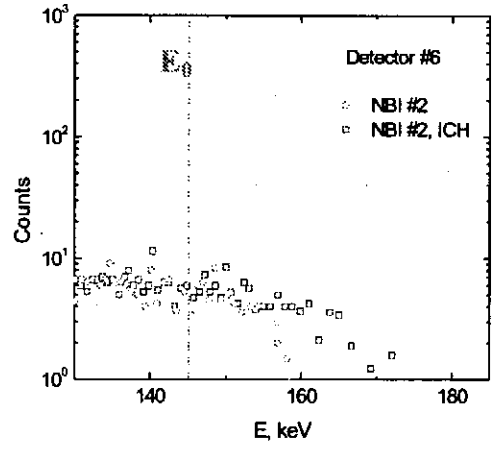

Fig. 4. Energetic tails expanding above the beam injection energy.

The dependence of the energetic particle distributions on LHD magnetic configuration has been investigated in experiments with combined H NBI and H minority ICRF heatings of low density He target plasmas with the magnetic axis shifted inwards and outwards in major radius. Measurements have been made along six viewing directions. The three different colors correspond to different magnetic axis positions. The measurements were made at similar

values of the H minority density (estimated H/(H+He) density ratio about 0.3). The magnetic field B_t was adjusted in order to preserve the ICR layer position. A clear difference can be seen between the three configurations. The relative values of the distribution increase and the spectra extend further for inward shifted plasmas. This is interpreted as a reduction of fast particle losses in comparison with the outward shifted case. The effect is more pronounced when the magnetic axis position changes from 3.75 m to 3.60 m than it is when R_{ax} changes from 3.60 m to a closer value 3.53 m.

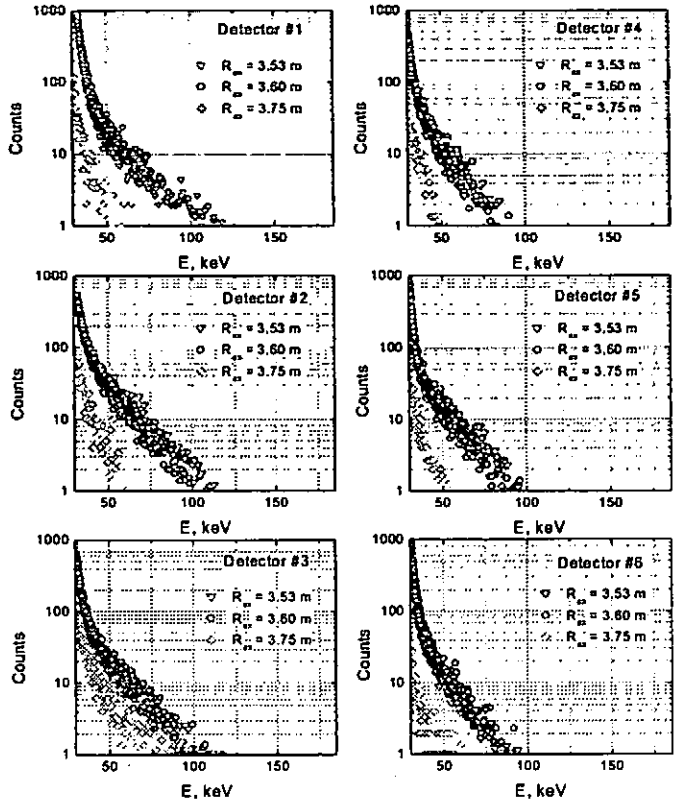

Fig. 5. Energetic particle distributions measured at three magnetic axis positions.

As it can be seen from Fig. 5, the effect is stronger for the detectors that observe nearer to the perpendicular direction in comparison with the more tangentially looking detectors. This indicates an improvement of trapped energetic particle confinement in inward shifted configurations.

The summary is as follows. The enhancement of the pitch angle scattering of beam ions in plasmas with higher effective charge has been observed. The velocity diffusion effect on energetic ion distributions has been interpreted in terms of the kinetic model. The time behaviour of tangential spectra is shown to be consistent with the classical slowing down. The above measurement results agree with the analytic model based on Fokker-Planck equation for energetic ions. The effect of increased fast ion population in inward shifted magnetic axis configuration has been verified experimentally on LHD.

[1] J.F. Lyon, P.R. Goncharov et al., Rev. Sci. Instrum., **74**, 1873 (2003)

[2] P.R. Goncharov, J.F. Lyon et al., J. Plasma Fusion Res. Series, **5**, 159 (2001)

[3] C.F. Barnett, ed., *Atomic Data for Fusion*, ORNL-6086 (ORNL, USA, 1990)

[4] R.A. Mapleton, *Theory of Charge Exchange* (John Wiley & Sons, New York, 1972)

Energetic Ion Confinement Analysis for the CHS-qa Quasi-Axisymmetric Stellarator

M.Isobe, D.A.Spong[1], A.Shimizu, T.Akiyama, C.Suzuki,
S.Nishimura, S.Okamura and K.Matsuoka

National Institute for Fusion Science
322-6 Oroshi-cho Toki-shi 509-5292 Japan
[1]Oak Ridge National Laboratory
P.O.Box 2009, Oak Ridge, TN 37831-8072, U.S.A.

1. Introduction

The quasi-axisymmetric stellarator CHS-qa, which is one of the so-called advanced stellarators, has been designed to provide good neoclassical confinement as well as magneto-hydrodynamic stability while realizing a tokamak-like, toroidally-symmetric magnetic structure in Boozer coordinates [1,2]. In CHS-qa, the neoclassical transport is significantly improved compared with that in the existing CHS [3]. However, we must verify the confinement of energetic ions, especially toroidally trapped ions since residual non-axisymmetric magnetic field components exist in the edge region and this residual ripple can enhance the radial diffusion of toroidally trapped ions. Effect of residual ripples on barely transit energetic ion orbits is also of interest because their orbits may become stochastic over many toroidal circulations and escape from the system after a while. In this work, the orbit topology of collisionless transit beam ions is numerically studied for CHS-qa configuration in Cartesian coordinates. Next, the confinement property of neutral beam (NB)-injected energetic ions (38keV/H^+) is investigated by use of particle simulation code DELTA5D following orbits in presence of slowing-down and pitch angle scattering processes on Boozer coordinates that has been developed at ORNL.

2. Collisionless orbits of parallel and anti-parallel beam ions in CHS-qa

Basic features of CHS-qa are briefly described. Figure 1 shows poloidal cross sections with different toroidal angles ϕ and magnetic field spectrum of CHS-qa. CHS-qa has a toroidal periods of 2, fairly low aspect ratio of 3.2 and is characterized by B_{10}(toroidicity)-dominated magnetic field structure in the whole region of the system although residual helical magnetic field ripples still exist in the peripheral region. The major radius R and the magnetic field strength B_t of CHS-qa are 1.5m and 1.5T, respectively at present design [1,2].

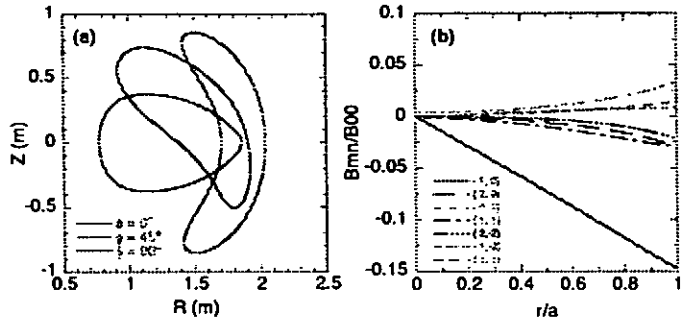

Figure 1 (a) Poloidal cross sections of CHS-qa in different toroidal angles ϕ. (b) Profile of magnetic field spectrum.

Assuming NB injection, which will be one of the primary heating methods for real experiments, collisionless orbits of parallel and anti-parallel NB ions are studied numerically in real coordinates. Fig. 2 shows their Poincare plots with energy of 38keV, which is an injection energy E_b of existing NB injector of CHS, at ϕ=0° (bean-shaped cross section) and ϕ=90° (horizontally elongated cross section) in the vacuum magnetic field produced by 20 modular coils for B_t of 0.5T and 1.5T [4]. The calculation in B_t of 0.5T is intended for high beta experiments. Beam ions are launched with $v_{//}/v \sim \pm 1$ corresponding to parallel and anti-parallel injection at r/a=+0.53 on the equatorial plane of ϕ=0° cross section and full gyro motions are followed by solving m•dv/dt=q•(vx**B**). Here, "+" in r/a stands for large R side from the magnetic axis. The red and blue lines represent orbits at B_t of 1.5T and 0.5T in the absence of collisions, respectively. The orbit analysis shows that the co-going beam ions whose birthplaces are in large R side are well confined as expected. Although beam ion orbits deviate substantially from magnetic flux surfaces at B_t of 0.5T as seen in Fig. 2(a) and 2(b), beam ions keep staying inside the system even if they are born in the peripheral region. On the other hand, counter-injected beam ions ionized at the edge region will be promptly lost even without collisions because their orbits largely deviate from flux surfaces toward inboard side and then cross the last closed magnetic flux surface (see Fig. 2(c) and 2(d)). The orbit analysis indicates that NB ions ionized at r/a > +0.43 can escape promptly at B_t of 0.5T, suggesting counter-injected NB heating will not be as efficient. By increasing B_t, prompt loss domain of

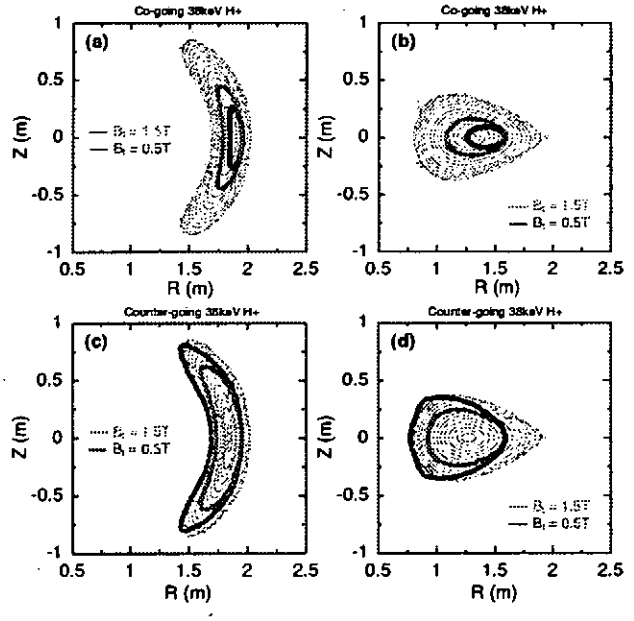

Figure 2 Poincare plots of co-going and counter-going transit neutral beam ions in Cartesian coordinates at ϕ=0° and 90° cross sections. The red and blue lines stand for orbits in B_t of 1.5T and 0.5T, respectively.

counter-injected beam ions becomes narrower as expected and confinement/prompt loss boundary is now located at r/a = +0.74 in B_t of 1.5T. An issue for prompt loss of counter-going beam ions will not be serious in B_t of 1.5T because a fraction of NB ions ionized in the region of r/a > +0.74 will be small.

3. Simulation of beam ion confinement in the presence of collisions by DELTA5D

As to evaluation of NB ion confinement, it is actually important to consider slowing-down and pitch angle scattering processes of beam ions because in typical experimental conditions, E_b of NB based on a positive ion source is not much higher than critical energy and in such a case, beam ions may be scattered into unconfined orbits through collisions with bulk ions. In order to evaluate global beam ion confinement in the presence of collisions, the particle simulation code DELTA5D [5] is employed. The guiding center beam ion orbits are followed in the equilibrium magnetic field obtained from the VMEC code which are then transformed to Boozer coordinates. The beam ions slowed down to $3/2 \cdot T_i$ are counted as part of thermal ions. The plasma parameters used here are ; $n_e(0)$=6.0x10^{19} m^{-3} with profile of $n=n(0) \cdot (1-(r/a)^2)$, $T_e(0)=T_i(0)$=1.5keV with profile of $T = T(0) \cdot (1-(r/a)^2)^2$. n_i (hydrogen) is given as $0.91 \cdot n_e$ and one impurity component is considered. The potential is set to be 0. NB of 38keV is injected into the plasma on the equatorial plane of ϕ=0° cross section and the initial pitch angle is given by taking the ratio of tangency radius R_{tan} of NB to the local value of R where the particles are ionized. The profile of NB ion density n_b is assumed to be as $n_b=n_b(0) \cdot (1-(r/a)^2)$ and only magnetic flux surfaces having $R > R_{ax}$ are populated with beam ions. Currently, charge exchange loss of beam ions is not consider in this analyis.

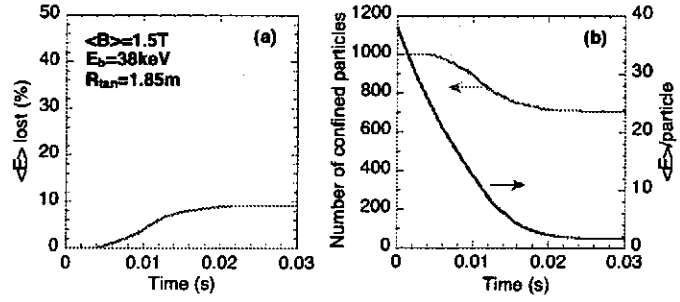

Figure 3 (a) Time evolution of <*E*> lost (%), (b) Number of confined ions and <*E*>/ions in the vacuum equilibrium.

Figure 3 shows time evolution of the percentage of energy lost (<*E*> lost) from the beam averaged over the ensemble of 1,000 ions, number of confined ions and averaged energy of ions in volume averaged magnetic field strength <*B*> of 1.5T with R_{tan} = 1.85m, corresponding to the parallel injection. The percentage of <*E*> lost is determined when it reaches a saturated plateau in its time evolution ; this plateau is associated with the average beam ion decelerating to the energy level of $3/2 \cdot T_i$.

We have studied dependence of <*E*> lost on R_{tan} and *B*. The energy loss rate increases as R_{tan} becomes small (see Figure 4(a)). Concerning co-injection, <*E*> lost is about 9.5% at R_{tan} of 1.85m and goes up to 25% at R_{tan} of 1.25m. The primary reason for this tendency is a radial diffusion of fast ions through ripple trapping due to pitch angle scattering. Because initial beam ion orbits are closer to passing-trapped boundary in velocity space as R_{tan} is decreased, they can be trapped more easily. It looks that residual ripples play an important role in confinement of toroidally trapped ions. Loss rate of counter-injected beam ions is higher than that in co-injected ions as expected and this is mainly due to prompt, first orbit loss. Next, by keeping R_{tan}, variation of <*E*> lost with <*B*> is investigated. <*E*> lost of counter-injected beam ions strongly depends on the magnitude of <*B*> and goes up to 40% even in tangential injection because of significant prompt loss fraction, whereas <*E*> lost of co-injected NB ions is not very sensitive to the magnitude of <*B*>.

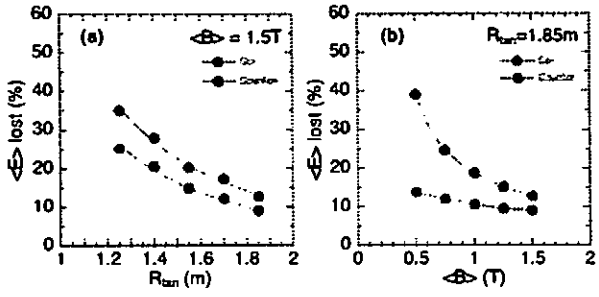

Figure 4(a) Dependence of beam losses on tangency radius in <*B*> of 1.5T. (b) Dependence of beam losses on field strength in R_{tan} of 1.85m in the vacuum equilibrium.

4. Summary

We have studied orbits and confinement property of NB-injected energetic ions in quasi-axisymmetric stellarator CHS-qa. It appears that tangentially co-injected beam ions are well confined even in the presence of collisions and <*E*> lost is evaluated to be about 9.5% at B_t of 1.5T. However, the beam ion confinement is deteriorated as R_{tan} is decreased because of existence of residual helical ripples. The confinement of counter-injected NB ions tends to be worse than that of co-injected ions as <*B*> is decreased due to some fraction of prompt loss and <*E*> lost is evaluated to be about 40% at <*B*> of 0.5T.

References

[1] S. Okamura *et al.*, Nuclear Fusion **41**(2001)1865.

[2] K. Matsuoka *et al.*, J. Plasma Fusion Res. SERIES **4**(2001)111.

[3] M.F. Heyn *et al.*, Plasma Phys. Control. Fusion **43**(2001)1311.

[4] A. Shimizu *et al.*, Fusion Engineering and Design **65**(2003)109.

[5] H. Kugel *et al.*, to be published in Fusion Science and Technology.

HEAT PULSE PROPAGATION STUDIES OF ANNULAR SAWTOOTH CRASH IN COMPACT HELICAL SYSTEM

S. Takagi[a)], K. Toi[a)], G. Matsunaga[b)], S. Nishimura[a)], K. Tanaka[a)], M. Takechi[c)], M. Isobe[a)], K. Matsuoka[a)], T. Minami[a)], S. Okamura[a)], M. Osakabe[a)], C. Takahashi[a)], Y. Yoshimura[a)] and CHS Group[a)]

[a)] *National Institute for Fusion Science, Toki 509-5292, Japan*
[b)] *Institut für Plasmaphysik Forschungszentrum, Jülich 52425, Germany*
[c)] *Japan Atomic Energy Research Institute, Naka 311-0193, Japan*

Introduction

In Compact Helical System (CHS), sawtooth oscillations are often observed in the neutral-beam-injection (NBI) heated plasmas [1]. In most of cases, both high frequency ($10 - 100\,\mathrm{kHz}$) and low frequency ($2 - 8\,\mathrm{kHz}$) magnetohydrodynamic (MHD) modes appear just before the crash and low frequency mode persists after the crash. These modes have the $m/n = 2/1$ (m and n: poloidal and toroidal mode number) mode structure. The former mode is energetic ion driven MHD mode, that is energetic particle mode (EPM) and the latter one is low-n interchange mode. Recent detailed analysis reveals that low frequency interchange mode is the main trigger of the crash observed in CHS [2]. The sawtooth crash takes place first near the $q = 2$ (q is the safety factor) rational surface located on the normalized minor radius $\rho \simeq 0.5$. The change in the soft X-ray (SX) signals around the plasma center is appreciably smaller than the change just inside the inversion radius. These behaviors of the sawtooth crash in CHS are phenomenologically consistent with that of the ideal/resistive interchange mode, because the radial mode structure of these instabilities are localized around the resonant surface in the low-beta plasmas [3].

Perturbative transport experiments have been carried out in many tokamak plasmas using the temperature or density perturbation induced by the $q = 1$ sawtooth crash [4–5]. In those experiments, the incremental electron heat diffusivity which is the diagonal element of the transport matrix was determined. However, the analysis is limited to a region outside the $q = 1$ radius. On the other hand, the heat and density pulses propagate both inside and outside the $q = 2$ radius due to the $q = 2$ annular crash. It is interesting from the viewpoint of the transport studies. We have investigated transport processes of $q = 2$ annular crash using a equation of electron temperature perturbation on an appropriate initial condition.

Experimental Results

Figure 1(a) shows time traces of SX signals for one period of the sawtooth oscillations, where the solid curves correspond to the SX signals eliminating $m/n = 2/1$ coherent components using FFT technique. ρ_{tan} denotes a normalized tangent minor radius of SX lines of sight. The sawtooth crash occurs at $t \simeq 134.2\,\mathrm{ms}$ (vertical line in the figure). Experimental crash time is about $0.5 - 1.0\,\mathrm{ms}$ and is fairly slow compared with that in tokamaks ($10 - 100\,\mu\mathrm{s}$). Temporal evolutions of the change in SX profile $\tilde{I}_{\mathrm{SX}}$ and the change in local SX emissivity profile $\tilde{E}_{\mathrm{SX}}$ due to the crash are shown in Fig. 1(b) and (c). Here, $\tilde{E}_{\mathrm{SX}}$ are obtained from chord-integrated data using the method discussed in Ref. [6]. The SX emissivity around $\rho \simeq 0.4$ drop sharply due to the crash, while the

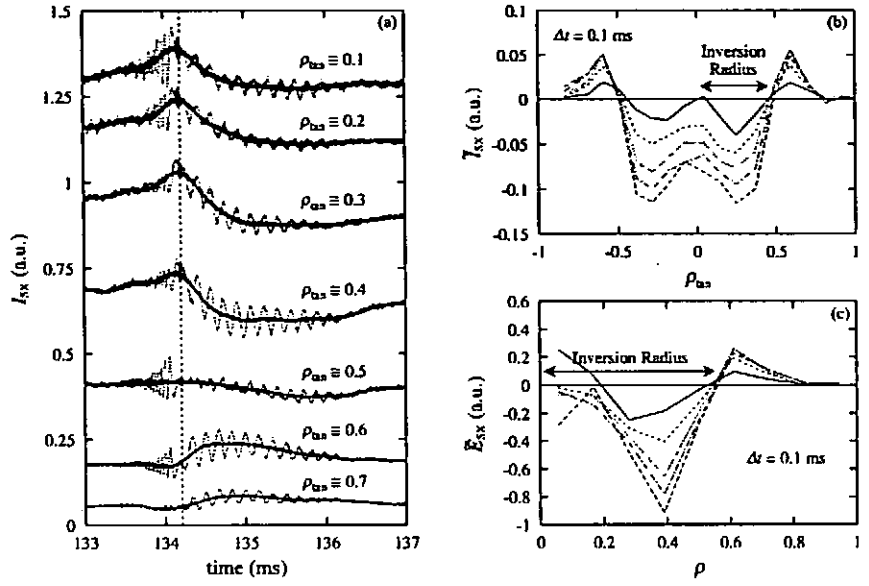

Figure 1: (a) Time traces of SX signals for one period of the sawtooth oscillations, where solid curves correspond to the filtered SX signals. (b) Temporal evolutions of the change in SX profile $\tilde{I}_{SX}$ for the case of the crash at $t \simeq 134.2$ ms in Fig. 1(a). (c) Temporal evolutions of the change in local SX emissivity profile $\tilde{E}_{SX}$.

crash does not affect the central region. These behaviors clearly indicates the character of the annular crash. The inversion radius in the SX emissivity profile is about $\rho \simeq 0.55$ and agrees well with the $q = 2$ rational surface in the rotational transform profile.

Heat Pulse Propagation Analysis

The basic equations for the heat pulse propagation analysis are the perturbed equations for the energy and particle balances expressed as follows [7]:

$$\frac{\partial \tilde{n}_e}{\partial t} = -\nabla \cdot \tilde{\Gamma}_e \tag{1}$$

$$\frac{3}{2} n_{e0} \frac{\partial \tilde{T}_e}{\partial t} = -\nabla \cdot \tilde{q}_e - T_{e0} \nabla \cdot \tilde{\Gamma}_e, \tag{2}$$

where Γ_e and q_e denote particle and heat fluxes, respectively. The equilibrium value of parameters are denoted by the subscript "0", while the perturbed quantities are expressed with a tilde. We assume $\tilde{q}_e = -n_e \chi_e \nabla \tilde{T}_e$ with unperturbed electron density $\tilde{n}_e \simeq 0$, which is supported by FIR interferometer measurement (typically $\tilde{n}_e \sim 1\,\%$). Then the simple diffusion equation regarding electron temperature perturbation is obtained as follows:

$$\frac{3}{2} a^2 n_{e0} \frac{\partial \tilde{T}_e}{\partial t} = \frac{1}{\rho} \frac{\partial}{\partial \rho} \left(\rho n_{e0} \chi_e \frac{\partial \tilde{T}_e}{\partial \rho} \right), \tag{3}$$

where a is the averaged minor radius of the plasma and χ_e is the electron heat diffusivity.

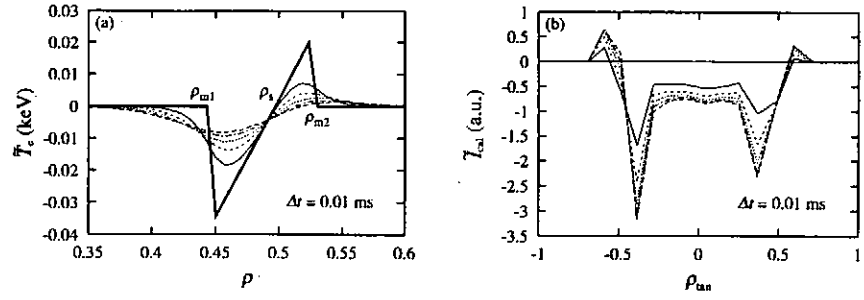

Figure 2: An example of the simulation result: (a) Temporal evolutions of the change in electron temperature $\tilde{T}_e(\rho, t)$ due to the annular crash. (b) Temporal evolutions of the change in SX signals $\tilde{I}_{cal}(\rho_{tan}, t)$. For these calculations, $\rho_{m1} = 0.45$, $\rho_s = 0.5$, $\rho_{m2} \simeq 0.53$ and $\chi_e = 1.0\,m^2/s$, respectively.

The initial condition of $\tilde{T}_e(\rho, t)$ expected to describe the annular crash is illustrated by the thick solid curve in Fig. 2(a). ρ_s is the $q = 2$ inversion radius. ρ_{m1} and ρ_{m2} are the "inner" and "outer" mixing radii. For the conservation of total heat content, we must satisfy $\int_0^1 \tilde{T}_e(\rho, 0)\,\rho d\rho = 0$. A simulation results for the annular crash are shown in Fig. 2. As can be seen from Fig. 2(a), the heat pulse propagates both inward and outward from the crash layer at $\rho \simeq 0.45 - 0.55$. The change in SX profile $\tilde{I}_{cal}(\rho_{tan}, t)$ obtained by the line-integration of local SX emissivity reconstructs the nature of the annular crash in the experimental results (Fig. 2(b)). Therefore, this analysis is useful for investigation of the heat pulse propagation of the annular crash.

For rough estimation of χ_e, we compare the arrival time of SX pulse peak t_p between experimental data and numerical one for various χ_e in Fig. 3(a). Here, χ_e is assumed to be uniform in space. It should be noted that t_p in the experimental data around the $q = 2$ rational surface located on $\rho_{tan} \simeq 0.5$ is fairly long. This indicates the possibility for the reduction of χ_e around the $q = 2$ rational surface. On the other hand, χ_e is thought to be $1.0 - 2.0\,m^2/s$ in the central region of $\rho_{tan} \leq 0.3$. Figure 3(c) shows the comparison of measured SX pulses with the best numerical fits, where χ_e profile shown in Fig. 3(b) is used in calculation. The fitted data except neighborhood of the rational surface agree well with the experimental data. On the other hand, the discrepancy between measured data and numerical one is large around the rational surface. The numerical data near the rational surface is sensitive for the location and width of the initial $\tilde{T}_e$ profile. It is difficult to estimate initial $\tilde{T}_e$ profile due to the limitation of the spatial resolution of the SX signals ($\delta\rho \simeq 0.1$). The electron diffusivity profile which gives the best numerical fits in Fig. 3(b) suggests the formation of the internal transport barrier (ITB) around the $q = 2$ rational surface. However, the electron temperature profile does not support the possibility of the formation of the ITB. Moreover, the obtained χ_e from the heat pulse propagation analysis is almost $\chi_e \simeq 1.0\,m^2/s$ except $q = 2$ layer and is smaller than that expected from the equilibrium transport analysis χ_{pb} ($2.0 - 5.0\,m^2/s$). The SX signal depends on the electron density, impurity levels and electron temperature. These contribution may slow down the radial propagation of the SX pulses.

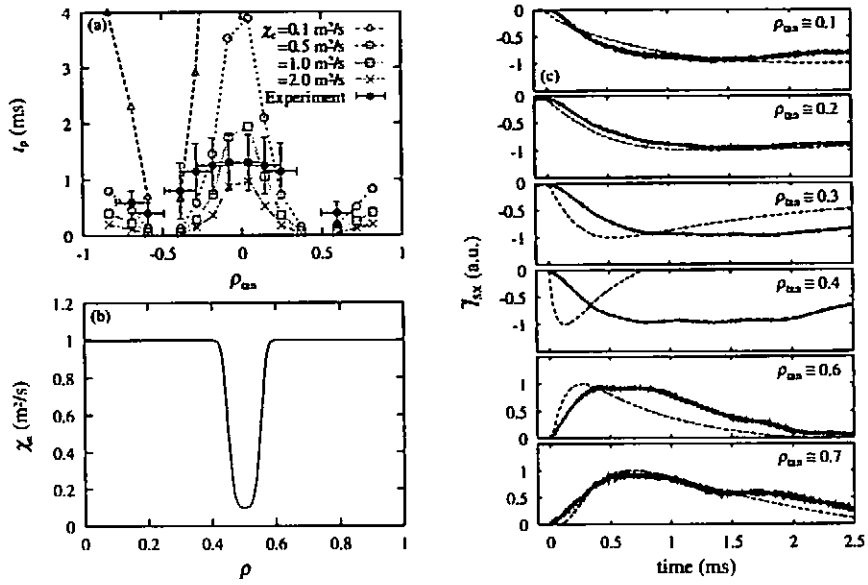

Figure 3: (a) Comparison of the arrival time of SX pulse between experimental data and numerical data (χ_e = 0.1, 0.5, 1.0 and 2.0 m^2/s). (b) The electron diffusivity χ_e which gives the best numerical fits. (c) SX signals at various radial positions (solid curve), compared with the best numerical fits (broken curve).

Summary

In CHS, $q = 2$ sawtooth oscillations are observed in NBI heated plasmas. The sawtooth crash indicates a character of an annular crash. The numerical analysis based on the simple diffusive model reconstructs the space and time evolutions of SX perturbation induced by the annular sawtooth crash. The obtained electron heat diffusivity χ_e from the heat pulse propagation analysis is smaller than that expected from the equilibrium transport analysis χ_{pb}. The resulting χ_e profile implies the formation of the internal transport barrier (ITB) around the $q = 2$ rational surface. However, the electron temperature profile does not support the possibility of the formation of the ITB.

References

[1] S. Takagi et al., Rev. Sci. Instrum. **72**, 721 (2001).
[2] S. Takagi et al., J. Plasma Fusion Res. Vol. 78, No. 12, 1275 (2002).
[3] H. Sugama and M. Wakatani, J. Phy. Soc. Jpn. **58**, 1128 (1989).
[4] J. D. Callen and G. L. Jahns, Phys. Rev. Lett. **38**, 491 (1977).
[5] M. Soler and J. D. Callen, Nucl. Fusion **19**, 703 (1979).
[6] S. Takagi et al., Jpn. J. Appl. Phys. Vol. 42, No. 1, p291 (2003).
[7] N. J. Lopes Cardozo, Plasma Phys. Control. Fusion **37**, 799 (1995).

Edge Plasma Turbulence in Fusion Devices:

Bursty Behavior and Fractal Properties

V.P. Budaev[1], S.Takamura[2], N. Ohno[2],
A. Komori[3], S. Masuzaki[3], G.S. Kirnev[1], S.A. Grashin[1]
[1]*Nuclear Fusion Institute, RRC Kurchatov Institute, 123182, Kurchatov Sq.1,Moscow,Russia* [2]*Department of Energy Engineering and Science, Graduate School of Engineering, Nagoya University, Nagoya 464-8603, Japan*
[3]*National Institute for Fusion Science, Oroshi 322-6, Toki, Gifu 509-5292, Japan*

Experimental measurements in the edge plasmas of fusion devices [1-5] have shown a bursty rather than random behavior of plasma fluctuations with non-Gaussian statistics and fractal properties suggesting the universality of self-similarity properties in edge of magnetically confined plasmas. Traditional methods like spectral ones have shown deviation from simple self-similarity (monofractality). Specific structure of plasma near the edge in fusion device with presence of magnetic structure hierarchy, can be involved in a stochastic process known as Levy-type process. It generates large-scale dynamics such as "flights" and ballistic transport with non-Gaussian statistics. Levy-type stochastic process may be a dynamic cause of the anomalous transport together with small-scale diffusion. Hence, the turbulence in fusion device should be considered as a multi-scale phenomenon. All these phenomena are beyond the Kolmogorov's refined self-similarity (monofractal) hypothesis [6]. Kolmogorov (1962) [7] formulated hypothesis invoking some statistical independence in the cascading process, which led to the log-normal model for the rate of dissipation of turbulent kinetic energy. To describe distinguish between absolute and weighted curdling of stochastic physical system the statistical description by multifractal formalism was proposed by Mandelbrot [8]. The multifractal formalism is based on the fact that the highly nonuniform probability distribution arises from the nonuniformity of the system possessing rich scaling properties and self-similarity. In the present work, experimental probe signals from the edge of tokamaks T-10 [9] and HYBTOK-II [10], the divertor plate probe of stellarator LHD [11] and the linear machine NAGDIS-II [12] have been analyzed in terms of the multifractal formalism revisited with wavelets. The multifractal formalism based on wavelet calculations allows one to study the scaling properties of turbulent fluctuations. The signals of density possess a high frequency part and a number of peaks caused by the intermittent structures that are called as intermittent bursts. The structures in the signal are studied by comparing the probability density function (pdf) with a Gaussian to measure how random the signal. The deviation from a Gaussian distribution could be due to a reduction of the number of degrees of freedom. In fully developed turbulence this is called intermittency where inhomogeneous distribution of the fluctuations leads to a coherent structure formation. The pdf's of density fluctuations are plotted in fig. 1. They are positively skewed, reflecting that positive fluctuations much greater than expected from a pure random distribution and associated with the large-scale bursts. As was observed in T-10 edge plasma, non-Gaussian statistics of density fluctuations transfers in the radial particle transport statistics (fig. 1).

Fluctuations in density and particle cross-field flux are investigated by wavelet technique (based on Morlet mother wavelet) to analyze radial moving of the turbulent structures in T-10 Scrape-off Layer(SOL) and NAGDIS-II. The technique makes use the fluctuating signals of two probes separated radially by 8 mm (for T-10) and 3 mm (for NAGDIS-II). Wavelet analysis suited for the description of the signals which display invariance, not under translation, but under scale change. Due to the time-scale nature the wavelet transform can be used to study a multi-scale phenomena such as plasma turbulence

with intermittency. Using the wavelet decomposition and reconstruction signal components within scale band of a, we compute a cross-correlation function (non-scaled) between the corresponding components of two probe signals. The maximum amplitude of this cross-correlation function, is referred as energy concentrated feature. In fig. 2(a), typical dependence of wavelet correlation maxima on a wavelet scale a is shown. For the reference, normalized linear cross-correlation function for the same two density series is shown in fig. 2(b). It demonstrates exponential decay with time lag, the value of a maximum is rather low (~0.25) no indication of the bursts radial moving on this plot. Contrary to this, wavelet correlation in fig. 2(a) shows the strong correlation at several scales illustrating bursty behavior of the process. Phase delay time (shift from zero) of the wavelet cross-correlation function maximum is used to compute the burst velocity defined as probe separation divided by the phase delay time.

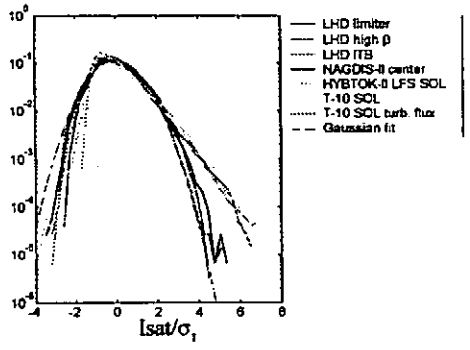

Figure 1. The pdf of the normalized density fluctuations in edge plasmas of fusion devices. The best fit by a Gaussian is plotted in a dash line.

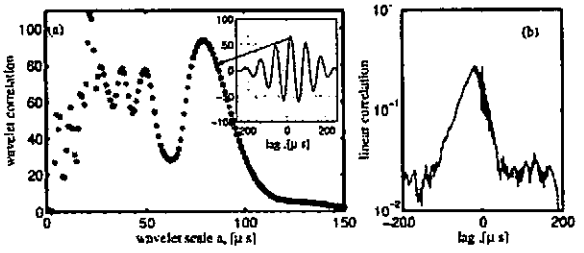

Figure 2. (a) Wavelet correlation between components of two probe signals vs. wavelet scale a. Local maxima of the dependence refer to the coherent events. In the inset a typical wavelet correlation function between corresponding components of two signals. (b) Linear cross-correlation function for the signals from probes separated radially by 8 mm

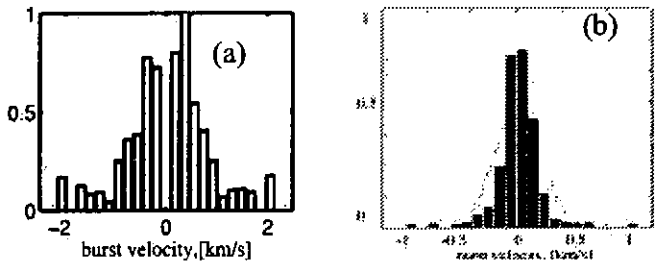

Figure 3.The pdf for the fluctuation in velocity of coherent events propagated radially across the magnetic field (a) T-10 SOL plasma (b) NAGDIS-II edge plasma.

The analysis shows numerous coherent events propagate with velocity of 150-2000 m/sec directed as outward as inward from plasma volume. This velocity is of 1-2 orders of magnitude below the sound speed. The pdf for this radial velocity, in fig. 3(a), is positively skewed indicating outward averaged flux, and the pdf is deviated from a Gaussian shape suggesting that process of burst radial propagation is not like a classical diffusion. Wavelet decomposition of turbulent radial flux demonstrates a fractal structure of transport process, large-scale fluctuations in radial transport are accompanied by high level of radial correlation in density fluctuations. The poloidal and toroidal structure of these structures is unknown. Similar result is obtained for NAGDIS-II probe experiment. Wavelet analysis shows that coherent events propagate across magnetic field with velocity of 100-1500 m/sec, fig 3b. Velocity of these events is distributed with positively skewed non-Gaussian pdf.

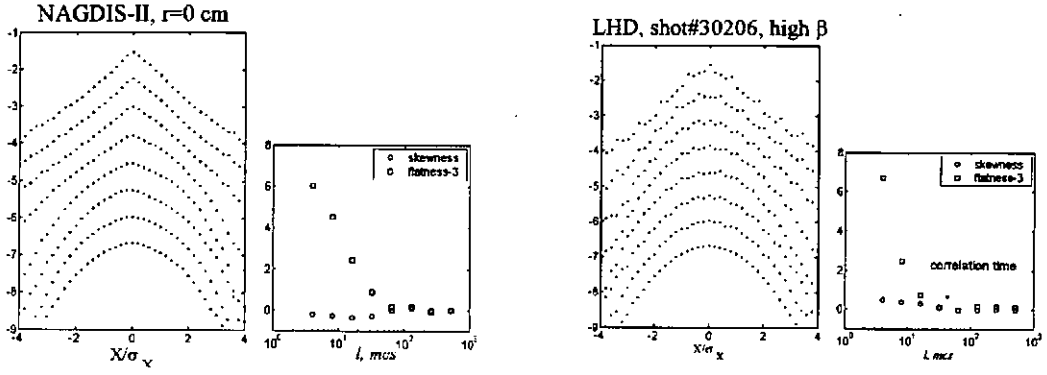

(a) (b)

Figure 4. Scaling properties of magnetized plasma fluctuations as an evidence of multifractality. Probability density functions of plasma density increments $\delta_l X(t)$ (normalized to its standard deviation) for different time scales (from top to bottom) l=2,4,8,16,32,64,128, 256 microseconds, in NAGDIS-II (a) and LHD divertor(b). One can see continuous deformation and the appearance of fat tails for fine scales at the scale related the correlation time.

It is observed that plasma edge turbulence in fusion devices demonstrates multifractal statistics, i.e. the scaling behaviour of absolute moments ($M(q,l)= M(q,L)\ (l/L)^{\zeta(q)}$, $M(q,l)=E(|\delta_l X(t)|^q)$, $\delta_l X(t)=X(t+l)-X(t)$) is described by a convex function $\zeta(q)=qH-\lambda^2 q^2$. Multifractality is a notion that is often related to an underlying multiplicative cascading process. The analyticity of the $\zeta(q)$ spectrum is deeply connected to the self-similarity properties of the function [13,14]: a function is self-similar if it can be written as a multiplicative (b) e in an appropriate space-scale (or time scale) representation [13-15]. In that context, the so-called multifractal formalism is valid, i.e., one can relate the $\zeta(q)$ spectrum to the singularity spectrum that provides information about the statistical distribution of singularity (Hölder) exponents h. Multifractality suggests that the probability distribution functions satisfy cascade equation with a Gaussian cernel when going from large to small time scales [15]. Thus, as far as the pdf of increments at different time scales are concerned, they will satisfy an evolution equation from "quasi-Gaussian" at very large scale L to fat tailed pdf's at small scales. This transformation of the pdf's for plasma turbulence in LHD divertor volume and NAGDIS-II is illustrated in fig. 4 where are plotted, in logarithmic scale, the standardized pdf's for different time scales in the range 1-250 microseconds. Multiplicative cascading process has «coarse» scale L from that iterating towards finer scales. This scale L is refered as correlation scale [15] (shown in fig. 4b of ~50 microseconds for LHD divertor) that characterizes coherent event scale in the turbulent plasma.

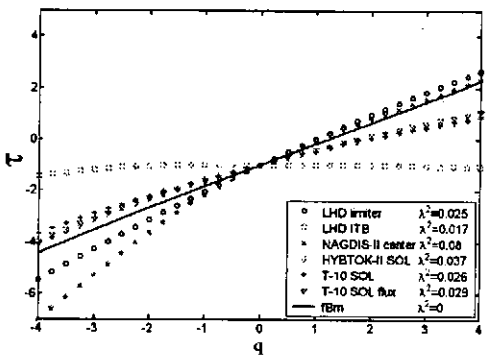

Figure 5.Scaling of moments $\tau(q)=\xi(q)-1=qH-\lambda^2 q^2 -1$ corresponding to the singularity spectrums for edge plasma turbulence. Parabolic behaviour is observed as evidence of multifractality. For monofractal $\tau(q)$ would be a linear function of q like fractional Brownian motion (fBm)

Using wavelet based technique[16], we have computed the scaling exponent $\zeta(q)$ for q-th order moments that include as positive as negative values of q. The dependence of the exponent $\zeta(q)=qH-\lambda^2 q^2$ reported in fig. 5, is well fitted by the parabolic shape that is predicted

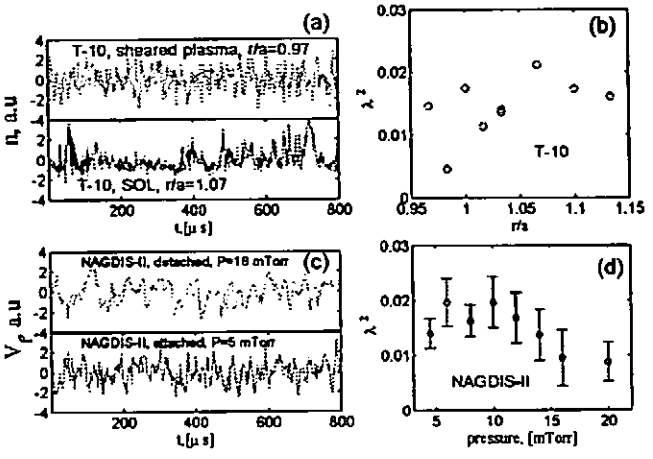

Figure 6. Degree of multifractality for edge plasma turbulence. (a) Density fluctuations in edge plasma of tokamak T-10 and in the shear edge region . (b) Radial dependence of multifractality factor λ^2 in T-10, in the shear region it is decreased. (c) Potential fluctuation in plasma of NAGDIS-II , detached (bottom) and attached (upper) mode. (c) Dependence of λ^2 with puffing pressure in NAGDIS-II, in detached plasma is decreased.

by log-normal model [15]. Parabolic behaviour is observed as evidence of multifractality for these time-series. For monofractal ones like fractional Brownian motion (fBm), the dependence would be a linear function of q. Estimated parameters of multifractality λ^2 are considered to be relevant value to characterize a phase transition in a plasma state. The degree of multifractality λ^2 changes with the edge plasma condition (fig. 6): the λ^2 is close to 0 for detached plasma in NAGDIS-II and sheared plasma (r/a=1.07) in T-10 that are close to Brownian (monofractal) motion. It reflects the fact of no self-organizing in these plasmas and no coherent structures responcible for the transport. It is observed mainly two levels of multifractality parameter: (1) for plasma with no self-organizing the value of λ^2 is close to 0; (2) for edge plasmas with clear bursty behaviour the parameter λ^2 is close to ~0.02-0.03 (as predicted by some stochastic models [15]). It suggests some universality of multifractal statistics and related transport properties in magnetized plasmas.

In summary, we have presented multifractal analysis of Langmuir probe signals from edge plasma of different fusion devices. It is observed that plasma edge turbulence in fusion devices demonstrates multifractal statistics, i.e. the scaling behaviour of absolute moments is described by a convex function suggesting the universality of self-similarity properties. Parameter of multifractality λ^2 is considered to be relevant value to characterize edge plasma state and related transport. Universality of multifractal properties observed in edge fusion plasmas is one of the key moment for the prediction of transport losses in large-scale fusion devices. To find whether the parameters of multifractality observed in this analysis, have a more universal validity, it would be interesting to extend multifractal analysis to a broader set of edge plasma data.

1.LaBombard et al. Nucl. Fusion, 40, 2041 (2000).
2.R.A.Moyer et al. Plasma Phys. Controlled Fusion 38, 1273 (1996).
3.G.Y.Antar et al. Phys. Rev. Lett. 87, 065001 (2001).
4.V.Budaev, G.Fuchs, R.Ivanov, and U.Samm, Plasma Physics and Controlled Fusion .3, 429 (1993).
5.G.M.Zaslavsky, et al.Phys. Plasmas.7, 3691 (2000).
6.Kolmogorov, Doklady Akad. Nauk SSSR(reprinted in Proc.R.Soc.London, Ser.A
7. A.N. Kolmogorov. J. Fluid Mech. 13, 82, (1962).
8.B.B. Mandelbrot, J. Fluid Mech. 62,331 (1974).
9.V.A.Vershkov et al., Proc. 28th EPS Conf. Contr. Fus. Plasma Phys. (Madeira, Portugal)1,3.098 (2001).
10. Y.Kikuchi e.a.Proc. 28th EPS Conf. Madeira, Portugal, 2001, p.277
11.N. Ohno, D. Nishijima, S. Takamura et al. Nuclear Fusion, 41, 1055 (2001)
12.S.Masuzaki et al. Nuclear Fusio n, 42,(2002) 750
13.J-F Muzy, D. Sornette, J. Delour and A. Arneodo. Quantitave Finance, 1,131 (2001).
14 J.F.Muzy, E.Bacry, and A. Arneodo, Int. J. Bifurcation Chaos Appl. Sci. Eng. 4,245 (1994).
15 E.Bacry, J.Delour, J.F. Muzy Phys.Rev. E, 64 , 026103-1 (2001)
16 S. Mallat and W. L. Hwang, IEEE Trans. Inf. Theory ,38, 617 (1992).

Imaging Bolometer for a Burning Plasma Experiment

B.J. Peterson[1], N. Ashikawa[1], S. Konoshima[2], L.C. Ingesson[3] and C. I. Walker[4]

[1]*National Institute for Fusion Science, Toki-shi, Gifu-ken 509-5292, Japan*
[2]*Japan Atomic Energy Research Institute, Naka-machi, Ibaraki-ken 311-0193, Japan*
[3]*EFDA Close Support Unit - Garching, Boltzmannstr. 2, D-85748 Garching, Germany*
[4]*ITER International Team - Garching, Boltzmannstr. 2, D-85748 Garching, Germany*

I. Introduction

Infrared Imaging Video Bolometers (IRVB) have recently been developed which can provide hundreds of channels of data in a two dimensional image of the plasma radiation and which can approach the sensitivity of resistive bolometers as IR cameras continue to improve [1]. Meanwhile, neutron irradiation tests of conventional resistive bolometers have shown a propensity of the resistive grids to break during the reactor shut down period, possibly due to a weakening of the gold grids due to partial transmutation to mercury [2], leading to some concern regarding their applicability to ITER. While imaging bolometers would not be prone to open circuits, they may have other problems resulting from the weakening of the gold foil due to transmutation to mercury, therefore other foil materials should be considered. In this paper imaging bolometers are considered as a replacement or supplement to resistive bolometers in diagnosing the radiated power loss from a fusion reactor. Numerous prospective foil materials are surveyed. A comparison is made of the IRVBs currently installed in the Large Helical Device (LHD), with a design for the JT-60U tokamak, a feasibility study for the International Thermonuclear Experimental Reactor (ITER) and conventional resistive bolometers in terms of sensitivity, spatial and time resolution, port access requirements, steady-state operation and long term durability.

II. Foil materials

The noise equivalent power for the IRVB [3] is given in terms of the foil thermal conductivity, k, thermal diffusivity, κ and thickness, t_f, the sensitivity of IR camera, σ, number of IR camera pixels per bolometer pixel, N, time resolution Δt and the area of the bolometer pixel, A, as

$$\eta_{IRVB} = \frac{\sqrt{10} k t_f \sigma}{\sqrt{N}} \sqrt{1 + \frac{A^2}{5\kappa^2 \Delta t^2}} \quad (1)$$

In terms of the foil material parameters this can be reduced to $\eta_{IRVB} \propto kt_f / \kappa$, which is inversely proportional to the IRVB sensitivity. In Table 1 (a) various metals are listed in order of (b) the IRVB sensitivity ($\propto \kappa/k$), also showing (c) the upper captured photon energy limit, (d) the melting point and (e) the minimum available thickness. Metals shown in red are best suited for energetic plasmas, with the ability to stop x-rays above 17 keV. Among those we have chosen gold for LHD (1 μm) and JT-60U (2.5 μm) due to inexpensive, readily available thin foils in large sizes. However in a high neutron flux environment such as ITER, gold may be inappropriate due to the reasons mentioned above. Therefore we have chosen Hf (10μm) for ITER for its high sensitivity and high melting point. Other factors should be considered such as outgassing, etc.

(a) metal	(b) κ/k (cm3C/J)	(c)Eph (keV)	(d)Tm (C)	(e)tmin (μm)
Sb	0.55	10.0	287	6
Mg	0.56	12	649	10
Zr	0.55	7.6	1852	3
Cd	0.50	10.2	321	5
Mo	0.45	9.4	2617	4
Nb	0.43	8.6	2468	2.5
Al	0.41	3.9	660	0.8
As	0.40	10.7	962	2
Ti	0.36	7.8	1660	4
Zn	0.36	12.3	419	2.5
Fe	0.34	11.0	1554	4
V	0.34	9.1	1690	3
Cu	0.29	8.0	1083	2
SS304	0.27	4.4	1400	8
Ni	0.25	12.5	1453	2
Co	0.25	12.0	1495	3

Table 1 IRVB foil material properties (a) element, (b) sensitivity, (c) maximum energy photon stopped by a 10 μm foil (< 8 keV, 8-13 keV, > 17 keV), (d) melting point and (e) minimum thickness available in a 10 cm x 10 cm foil [].

III. IRVBs in LHD

Currently 3 IRVBS are installed and operating in LHD, one with a tangential view in Port 6-T, one with a top view in Port 6.5-U and one with a semi-tangential view in Port 5-O, as shown in Fig. 1 and detailed in Table 2.

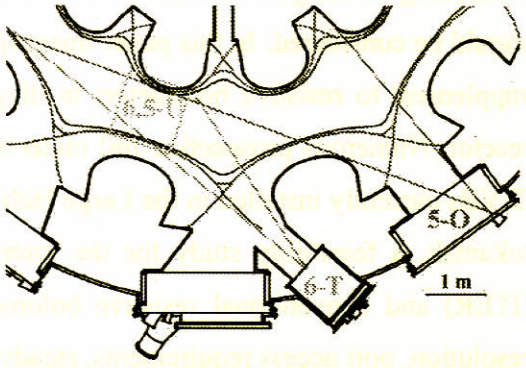

Fig. 1 Top view of LHD with LCFS, ergodic edge and divertor legs with sightlines of IRVBs from ports 6-T, 6.5-U and 5-O.

IV. IRVB design for test on JT-60U

An IRVB for JT-60U has been designed and constructed with plans to install in August of 2003. The field of view of the central column of bolomter pixels in the poloidal cross-section is shown in Fig. 1 with the design specifications shown in Table 2. The main objectives of this project are (1) to test the operation of the IRVB in a tokamak, as there is some concern over the durability of a large thin foil in the presence of disruptions, and (2) to compare it with the existing resistive bolometers on JT-60U.

V. Imaging Bolometers for ITER

In Fig. 3 the (a) spatial and (b) angular coverage of four IRVB arrays designed for ITER are shown. The design parameters of the yellow array are shown in Table 2 as an example. The installation would be similar to the existing plans for IR thermography diagnostics with an IR endoscope/ labyrinth to view the foil mounted in a pinhole camera directly behind the blanket service module, while shielding the IR camera mounted outside the port plug from neutrons.

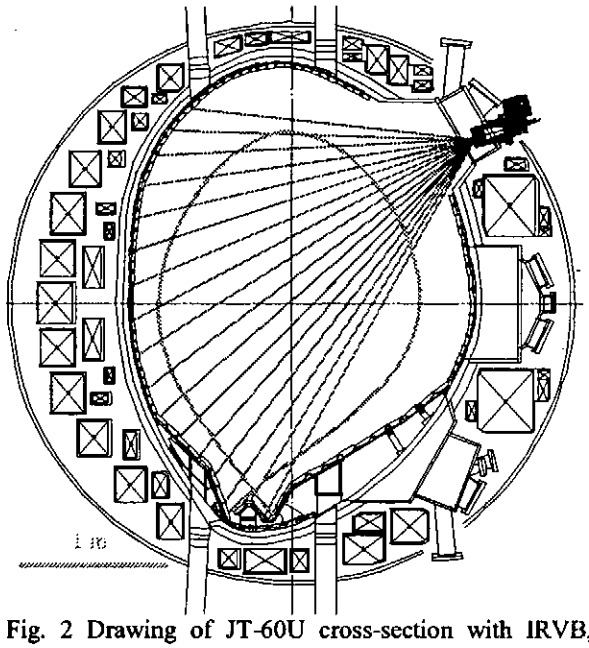

Fig. 2 Drawing of JT-60U cross-section with IRVB, IRVB central sight lines and approximate separatrix.

VI. Discussion

Comparison of the IRVBs in Table 2 shows the improvement that can be made with a state-of-the-art IR camera in the case of the ITER design compared to the other IRVBs in terms of the number of channels (x4-8), time resolution (x2-6) and photon energy range (x2-3) while having the same or somewhat worse sensitivity (x0.2-1). Fig. 3 shows that with one tangential IRVB (yellow) complete spatial coverage of the entire cross-section can be achieved, as well as reasonable angular coverage. This array even has better angular coverage of the divertor than the tangential array viewing the divertor (green) although the density of sightlines would be less than half.

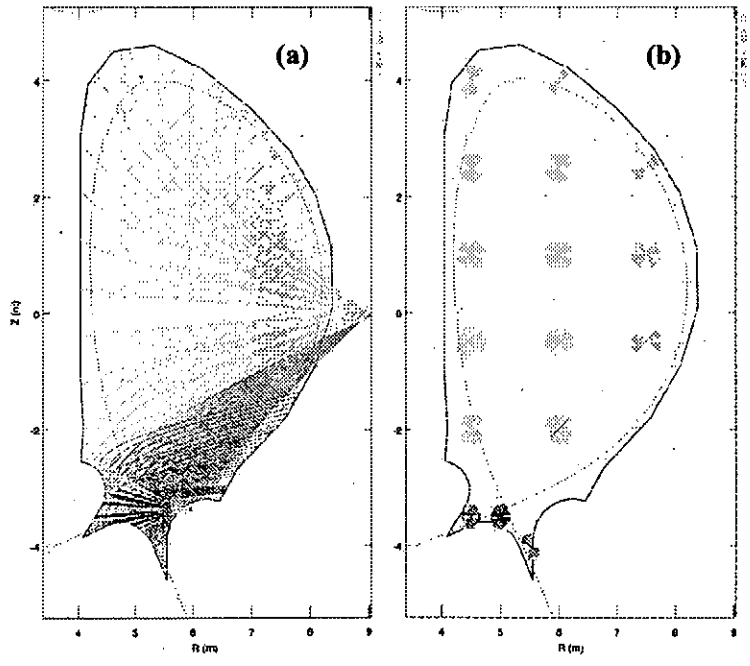

Fig. 3 (a)Projection into poloidal plane of sight lines of IRVB arrays on ITER: [illegible], tangential view from equatorial port of divertor plasma, semi-tangential view from divertor of divertor, tangential view from divertor of divertor (b) plots of angular coverage by each of the arrays in Fig 3 (a) at 16 points in the poloidal cross-section. Dashed line shows separatrix. (zoom for details)

Comparison of the blue and red arrays shows the superiority of the tangential array (red) in angular coverage which was seen in other cases in our study. Angular coverage by the yellow array is strongest near the equatrotial plane and could be augmented in the divertor by the red array and in the upper portion of the cross-section by a tangential array form the upper port. The area with the weakest angular coverage would be the out board edge, which could not be remedied by IRVBs alone. In order to determine the sufficiency of these arrays a tomographic modeling study should be carried out.

[1] B.J. Peterson *et al.*, *Plasma Physics and Cont. Fusion* **45**, 1167 (2003).

[2] T. Nishitani, T. Shikama, R. Reichle *et al.*, *Fusion Engin. Design* **63-64**, 437 (2002).

[3] B.J. Peterson *et al.*, *Rev. Sci. Instrum.* **74**, 2040 (2003).

Device /Port	IR Camera		IRVB						Signal level, S (W/ cm^2)	SA/ η
	Make/ Model	σ (mK)	Slit/ pixel size A (mm^2)	Foil Metal/ t_f (μm)	E_{ph} (keV)	Δt (ms)	Ch # (N)	η/A (μW/ cm^2)		
LHD/ 6T	AGEMA THV900	120	8 x 8/ 7 x 7	Au/ 1	5.6	67	11x7 (100)	70		
LHD/ 6.5U	FLIR/ SC500	150	20x24 /8 x 8	Au/ 1	5.6	17	9 x 9 (64)	400		
LHD/ 5O	FLIR/ SC500	120	8 x 8/ 7 x 7	Au/ 1	5.6	17	11x11 (196)	180		
JT-60U P-9	Indigo/ Omega	85	5 x 5/ 5 x 5	Au/ 2.5	8	33	12x16 (64)	300		
ITER	Indigo/ Phoenix	25	2.5x2.5/ 2.5x2.5	Hf/ 10	18	10	25x34 (289)	400		

Table 2. Parameters for existing and planned imaging bolometers and exisiting and planned resistive bolometer arrays.

Recent Issues of NIFS Series

NIFS-759 S. Kubo, T. Shimozuma, H. Idei, Y. Yoshimura, T. Notake, M. Sato, K. Ohkubo, T. Watari,K. Narihara, I. Yamada, S. Inagaki, Y. Nagayama, S. Murakami, S. Muto,Y. Takeiri, M. Yokoyama, N. Ohyabu, K. Ida, K. Kawahata, O. Kaneko, A. Komori, T. Mutoh, Y. Nakamura, H. Yamada, T. Akiyama, N. Ashikawa, M. Emoto, H. Funaba, P. Goncharov M. Goto, K. Ikeda, M. Isobe, H. Kawazome, K. Khlopenkov, T. Kobuchi, A. Kostrioukov, R. Kumazawa, Y. Liang, S. Masuzaki, T. Minami, J. Miyazawa, T. Morisaki, S. Morita, H. Nakanishi, Y. Narushima, K. Nishimura, N. Noda, H. Nozato, S. Ohdachi, Y. Oka, M. Osakabe, T. Ozaki, B. J. Peterson, A. Sagara, T. Saida, K. Saito, S. Sakakibara, R. Sakamoto, M. Sasao, K. Sato, T. Seki, M. Shoji, H. Suzuki, N. Takeuchi, N. Tamura, K. Tanaka, K. Toi, T. Tokuzawa, Y. Torii, K. Tsumori, K. Y. Watanabe, Y. Xu, S. Yamamoto, T. Yamamoto, M. Yoshinuma, K. Itoh, T. Satow, S. Sudo, T. Uda, K. Yamazaki, K. Matsuoka, O. Motojima, Y. Hamada and M. Fujiwara
Transport Barrier Formation by Application of Localized ECH in the LHD
Oct. 2002 (EX/C4-5Rb)

NIFS-760 T. Hayashi, N. Mizuguchi, H. Miura, R. Kanno, N. Nakajima and M. Okamoto
Nonlinear MHD Simulations of Spherical Tokamak and Helical Plasmas
Oct. 2002 (TH/6-3)

NIFS-761 K. Yamazaki, S. Imagawa, T. Muroga, A. Sagara, S. Okamura
System Assessment of Helical Reactors in Comparison with Tokamaks
Oct. 2002 (FT/P1-20)

NIFS-762 S. Okamura, K. Matsuoka, S. Nishimura, M. Isobe, C. Suzuki, A. Shimizu, K. Ida, A. Fujisawa, S. Murakami, M. Yokoyama, K. Itoh, T. Hayashi, N. Nakajima, H. Sugama, M. Wakatani, Y. Nakamura, W. Anthony Cooper
Physics Design of Quasi-Axisymmetric Stellarator CHS-qa
Oct. 2002 (IC/P-07)

NIFS-763 Lj. Nikolic, M.M. Skoric, S. Ishiguro and T. Sato
On Stimulated Scattering of Laser Light in Inertial Fusion Energy Targets
Nov. 2002

NIFS-764
NIFS Contributions to 19th IAEA Fusion Energy Conference (Lyon, France, 14-19 October 2002)
Nov. 2002

NIFS-765 S. Goto and S. Kida
Enhanced Stretching of Material Lines by Antiparallel Vortex Pairs in Turbulence
Dec. 2002

NIFS-766 M. Okamoto, A.A. Maluckov, S. Satake, N. Nakajima and H. Sugama
Transport and Radial Electric Field in Torus Plasmas
Dec. 2002

NIFS-767 R. Kanno, N. Nakajima, M. Okamoto and T. Hayashi
Computational Study of Three Dimensional MHD Equilibrium with m/n=1/1 Island
Dec. 2002

NIFS-768 M. Yagi, S.-I. Itoh, M. Kawasaki, K. Itoh and A. Fukuyama
Multiple-Scale Turbulence and Bifurcaion
Jan. 2003

NIFS-769 S.-I. Itoh, K. Itoh and S. Toda
Statistical Theory of L-H Transition and its Implication to Threshold Database
Jan. 2003

NIFS-770 K. Itoh
Summary: Theory of Magnetic Confinement
Jan. 2003

NIFS-771 S.-I. Itoh, K. Itoh and S. Toda
Statistical Theory of L-H Transition in Tokamaks
Jan. 2003

NIFS-772 M. Stepic, L. Hadzievski and M.M. Skoric
Modulation Instability in Two-dimensional Nonlinear Schrodinger Lattice Models with Dispersion and Long-range Interactions
Jan. 2003

NIFS-773 M.Yu. Isaev, K.Y. Watanabe, M. Yokoyama and K. Yamazaki
The Effect of Hexapole and Vertical Fields on α-particle Confinement in Heliotron Configurations
Mar. 2003

NIFS-774 K. Itoh, S.-I. Itoh, F. Spineanu, M.O. Vlad and M. Kawasaki
On Transition in Plasma Turbulence with Multiple Scale Lengths
May 2003

NIFS-775 M. Vlad, F. Spineanu, K. Itoh, S.-I. Itoh
Intermittent and Global Transitions in Plasma Turbulence
July 2003

NIFS-776 Y. Kondoh, M. Kondo, K. Shimoda, T. Takahashi and K. Osuga
Innovative Direct Energy Conversion Systems from Fusion Output Thermal Power to the Electrical One with the Use of Electronic Adiabatic Processes of Electron Fluid in Solid Conductors.
July 2003

NIFS-777 S.-I. Itoh, K. Itoh and M. Yagi
A Novel Turbulence Trigger for Neoclassical Tearing Modes in Tokamaks
July 2003

NIFS-778 T. Utsumi, J. Koga, T. Yabe, Y. Ogata, E. Matsunaga, T. Aoki and M. Sekine
Basis Set Approach in the Constrained Interpolation Profile Method
July 2003

NIFS-779 Oleg I. Tolstikhin and C. Namba
CTBC A Program to Solve the Collinear Three-Body Coulomb Problem: Bound States and Scattering Below the Three-Body Disintegration Threshold
Aug. 2003

NIFS-780 NIFS
Contributions to 30th European Physical Society Conference on Controlled Fusion and Plasma Physics (St.Petersburg, Russia, 7-11 July 2003) from NIFS
Aug. 2003